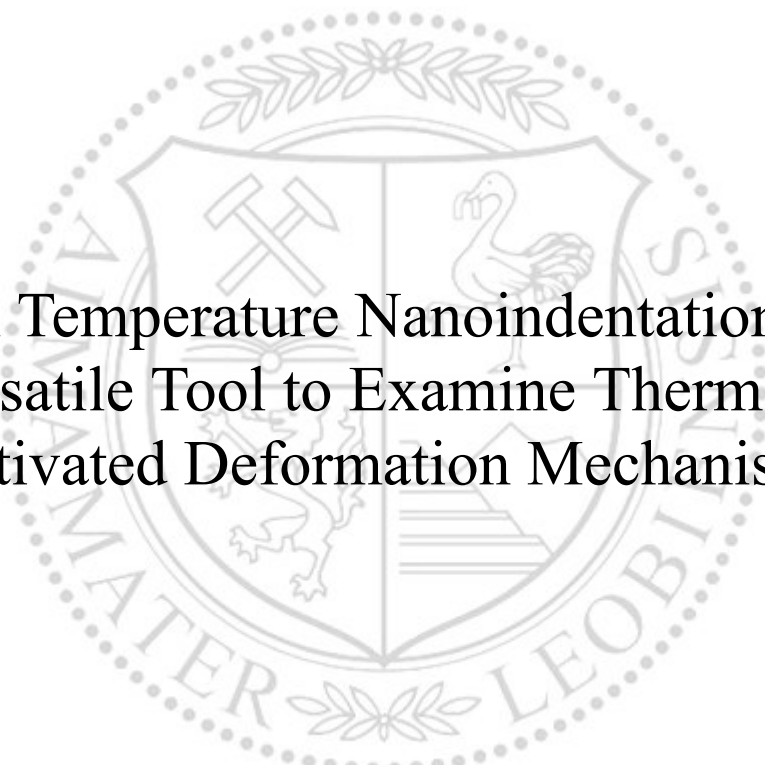




Chair of Physical Metallurgy and Metallic Materials

Doctoral Thesis



High Temperature Nanoindentation as a
Versatile Tool to Examine Thermally
Activated Deformation Mechanisms

Dipl.-Ing. Johann Kappacher, BSc

March 2021



AFFIDAVIT

I declare on oath that I wrote this thesis independently, did not use other than the specified sources and aids, and did not otherwise use any unauthorized aids.

I declare that I have read, understood, and complied with the guidelines of the senate of the Montanuniversität Leoben for "Good Scientific Practice".

Furthermore, I declare that the electronic and printed version of the submitted thesis are identical, both, formally and with regard to content.

Date 01.03.2021

A handwritten signature in blue ink, appearing to read 'Johann Kappacher', written over a horizontal line.

Signature Author
Johann Kappacher

Danksagung

An erster Stelle möchte ich mich bei meiner Betreuerin Frau Verena Maier-Kiener für ihre Unterstützung in den vergangenen vier Jahren und die Möglichkeit ein so interessantes Thema bearbeiten zu können bedanken. Durch zahlreiche hochkarätigen wissenschaftlichen Diskussionen und Anregungen konnte so manches werkstofftechnische oder experimentelle Problem gelöst werden. Die vielen Konferenzen im In- und Ausland die sie mir während meiner Zeit als Dissertant ermöglichte, waren eine wahre Bereicherung durch die ich viele neue Kontakte und Freundschaften knüpfen konnte. Auch habe ich von ihr so manches über das Leben abseits des wissenschaftlichen Arbeitens gelernt, wofür ich sehr dankbar bin.

Auch meinem Mentor, Herrn Daniel Kiener sei an dieser Stelle mein Dank ausgesprochen. Seine Anregung zu meinen wissenschaftlichen Ergüssen waren stets sehr hilfreich und haben maßgeblich zum Gelingen dieser Arbeit beigetragen. Die Diskussions-, Grill- und Weinabende bei euch beiden werde ich mit Freuden in guter Erinnerung behalten.

Vielen Dank auch an Herrn Helmut Clemens für die Möglichkeit an seinem Lehrstuhl mein Dissertationsvorhaben in die Tat umzusetzen. Die vielen gemeinsamen fachlichen Besprechungen mit ihm waren stets auch mit einer Prise Humor gewürzt und haben uns allen den Alltag am Institut versüßt. Sein unermüdlicher Einsatz, auch noch über Nacht ein Manuskript zu korrigieren, um eine knappe Deadline einhalten zu können, machte es möglich diese wissenschaftliche Arbeit zu erstellen.

Ein besonderer Dank gilt meinen Kollegen und Freunden in der MEH-Gruppe, Maximilian Siller, Anna-Sophie Ebner und Severin Jakob. Die Erlebnisse auf unseren gemeinsam besuchten Konferenzen, wie die Shooting-Range oder das Rodeo in Texas werden uns wohl noch lange in lebhafter Erinnerung bleiben. Über die Jahre haben wir uns zu einem eingeschweißten Team entwickelt und ich hoffe, dass das auch in Zukunft so bleiben wird.

Meinen Bürokollegen, den Mitgliedern des Herrensalons: Phillip Haslberger, Michael Burtscher, Manfred Stadler, Jan Ingo Platl und Michael Göbl sei gedankt für die immerzu aufmunternde und lustige Zeit, auch wenn es einmal nicht so gelaufen ist. Unvergessen bleiben werden diverse Auftritte der "Stahlbannenboys" oder von "Hanna und die harten Kerle" auf Weihnachtsfeiern und Institutsgillereien.

Auch Freunde, die ich schon während meines Studiums kennengelernt habe und die gemeinsam mit mir eine Dissertation begonnen haben, Sandra Ebner und Matthias Hofinger, möchte ich meinen Dank aussprechen. Die zahlreichen gemeinsam verbrachten Spieleabende ermöglichten es auch nach langen Arbeitstagen den Kopf wieder freizubekommen.

Den Institutsmitarbeitern Reinhilde Stopar, Angelika Tremmel, Regina Kranz und Susanne Strasak (Sekretariat), Gerhard Hawranek (REM und ein Meister der Akustikgitarre), Silvia Pölzl (Metallographie) und Alfons Lontschar (EDV), ohne deren tatkräftige Unterstützung diese Arbeit nicht so reibungslos abgelaufen wäre. Ihnen allen sei an dieser Stelle herzlich gedankt.

Für die Unterstützung über Institutsgrenzen hinweg möchte ich mich bei Markus Alfreider, Oliver Renk, Michael Wurmshuber, Christian Saringer, Michael Tkadletz, Christina Hofer und Andreas Landefeld bedanken, die immer ein offenes Ohr für Anliegen aller Art hatten.

Abschließend möchte ich mich bei meiner Familie für den Rückhalt und die tatkräftige Unterstützung während der vergangenen Jahre bedanken. Ein besonderer Dank gilt meiner Freundin Katharina, die es immer wieder versteht mich mental aufzubauen, auch wenn es mal nicht so läuft wie geplant.

Vielen Dank!

Abstract

Modern technical devices in microelectronics, energy harvesting or display technology become ever smaller. Therefore, small-scale mechanical testing techniques are a rising field of research in order to satisfy the demand to investigate and understand the possibly changing underlying deformation mechanisms of materials used in these applications and thereby secure reliability of such devices. Depth sensing hardness testing, commonly designated as nanoindentation, can be such a method of choice and with advancing refinement of methodology a variety of materials properties can be extracted.

In this PhD-thesis high temperature nanoindentation with a focus on development of high temperature methodology and thermal management was systematically accomplished. Thermal activation analyses were carried out to investigate the dominating deformation mechanisms on a variety of materials with a special focus on body-centered cubic metals, and therefore the influence of alloying elements and refinement of microstructure into the ultra-fine grained regime.

It was found that in coarse grained W-Re alloys the alloying element Re mainly influence the low temperature plasticity by a reduction of the Peierls barrier, while at high temperatures dislocation-dislocation interaction was evident. Contrarily, in case of a reduced grain size to some hundreds of nanometers, the effect of Re on the mechanical properties primarily originates at high temperatures through grain boundary diffusion processes. By designing samples with custom grain boundary types on Ta_{2.5}W, the role of misorientation of adjacent grains and the consequently changed interface diffusivity on the high-temperature plastic deformation behavior was highlighted. It was found that the temperature- and rate-dependence of the flow stress is strongly reduced for samples consisting mainly of low-angle grain boundaries, in contrast to a random high-angle character.

Further the mechanical properties and deformation mechanisms occurring upon a phase transformation were examined in a previously non-existing way with micromechanical methods on pure metallic cobalt. It was found that a transformed crystal structure sharply leads to a change in plasticity. Cobalt specifically undergoes a development in the rate controlling deformation mechanism from friction stress controlled basal dislocation glide to dislocation cross slip as temperature increases. Upon phase transformation the process that controls plasticity was found to change again to obstacle-controlled dislocation glide.

The present work clearly highlights the versatility of advanced high temperature nanoindentation methods as a tool for thermal activation analysis and determination of the dominating deformation mechanisms in a variety of materials. This will help in the development of future high performance materials with complex microstructures to tailor alloy design and meet their high requirements for specific materials properties.

Kurzfassung

Moderne technische Geräte der Mikroelektronik, Energiegewinnung oder Displaytechnologie werden immer kleiner. Daher sind Prüfmethode in kleinen Dimensionen ein wachsendes Forschungsfeld, um die mechanischen Eigenschaften von Materialien in solchen Anwendungsfeldern zu untersuchen. Durch die Miniaturisierung können sich die zugrundeliegenden Verformungsmechanismen grundlegend ändern, welche untersucht und verstanden werden müssen um die Zuverlässigkeit solcher Geräte zu sichern. Die tiefenregistrierende Härteprüfung, allgemein als Nanoindentation bekannt, kann eine solche Prüftechnik sein, und mit fortschreitender Verbesserung der Methodik können eine Vielzahl von Materialeigenschaften ermittelt werden.

In der vorliegenden Dissertation wird die Hochtemperatur Nanoindentation mit einem Schwerpunkt auf Methodik und thermisches Management systematisch untersucht. Verschiedene Techniken der thermischen Aktivierungsanalyse wurden durchgeführt um den dominierenden Verformungsmechanismus einer Reihe von Werkstoffen mit einem Fokus auf kubisch raumzentrierten Metallen zu untersuchen. Besonderes Augenmerk wurde auf den Einfluss von Legierungselementen und Korngrößenvariationen bis in den ultrafeinkörnigen Bereich gelegt.

Die Ergebnisse zeigten, dass in grobkörnigen W-Re Legierungen das Legierungselement Re vorwiegend die Tieftemperaturplastizität durch ein Verringern des Peierls Potentials beeinflusst, während bei hohen Testtemperaturen die Wechselwirkung zwischen Versetzungen dominiert. Im Gegensatz dazu wirkt sich in denselben Materialien, wenn die Korngröße auf wenige hundert Nanometer verringert wird, der Effekt von Re hauptsächlich auf die Hochtemperatureigenschaften durch Korngrenzdifusion aus. In Untersuchungen an Ta_{2.5}W mit maßgeschneiderten Korngrenzen konnte die Rolle der Missorientierung zwischen den Körnern und der daraus geänderten Korngrenzdifusion auf das Hochtemperaturverhalten in kubisch raumzentrierten Metallen untersucht werden. Es wurde gezeigt, dass die Temperatur- und Dehnratenabhängigkeit der Fließspannung für Proben mit überwiegendem Kleinwinkelkorngrenzcharakter deutlich reduzierter ausfällt im Vergleich zu solchen mit Großwinkelkorngrenzen.

Außerdem wurden die mechanischen Eigenschaften und der Verformungsmechanismus, welche während einer Phasenumwandlung auftreten untersucht. Dies erfolgte in einer bisher nicht beschriebene Art mittels mikromechanischer Methoden an reinem metallischen Cobalt. Dadurch konnte gezeigt werden, wie sich eine Änderung der Kristallstruktur auf die Plastizität auswirkt. In Cobalt ändert sich mit steigender Temperatur der Verformungsmechanismus von reibspannungskontrolliertem Versetzungsgleiten auf der Basalebene zu Versetzungsquergleiten. Oberhalb der Umwandlungstemperatur tritt als ratenbestimmender Schritt das Schneiden von Waldversetzungen auf.

Die vorliegende Arbeit hebt die Vielseitigkeit von weiterentwickelten Hochtemperatur Nanoindentationsmethoden für die thermische Aktivierungsanalyse und die Bestimmung des dominierenden Versetzungsmechanismus in einer Vielzahl unterschiedlicher Werkstoffe hervor. Damit sollen in Zukunft Materialien für Hochleistungsanwendungen mit komplexer Mikrostruktur gezielt entwickelt werden können um den hohen Anforderungen an spezielle Werkstoffeigenschaften gerecht zu werden.

Contents

Part I

1 Motivation and Aim of the Thesis	1
2 Nanoindentation - State of the Art	2
2.1 Conventional Nanoindentation Testing	2
2.2 Dynamic Nanoindentation Analysis	3
2.3 Probing Thermally Activated Processes with Nanoindentation	4
2.3.1 Constant Indentation Strain Rate Experiments	4
2.3.2 Strain Rate Jump Tests	5
2.3.3 Extraction of the Activation Energy for Plastic Deformation	6
3 Implementation of a New High Temperature Nanoindentation System	8
3.1 The InSEM-HT System	8
3.2 Thermal Gradients and Tip Temperature Calibration	9
3.3 Thermal Drift and Temperature Matching	11
3.4 Choice of Indenter Material and Tip Degradation	14
4 Application Examples	18
4.1 Comparison Between Different Nanoindenter Platforms	18
4.2 Identification of the Deformation-Bearing Phase in a Two-Phase Duplex Steel - Room Temperature Property Mapping	21
4.3 High Temperature Performance of Different Cu-Alloys	23
5 Summary of Publications	25
5.1 Publication List	25
5.2 Conference Contributions	27
5.3 Supervised Theses	27
5.4 Fundamentals of Plasticity in bcc Metals with Confined Microstructure	28
5.5 Influence of Bulk Phase Transformation on Thermally Activated Deformation Processes	33
6 Concluding Remarks and Outlook	35
References	37

Part II

Publication A	45
Publication B	53
Publication C	65
Publication D	79

Abbreviations

A_c	projected contact area	HAGB	high-angle grain boundary
a_0	geometry factor	hcp	hexagonal closed packed
β	geometry factor	HPT	high pressure torsion
bcc	body-centered cubic	HT	high temperature
BSE	back-scattered electron	k_B	Boltzmann constant
C^*	constraint factor	LAGB	low-angle grain boundary
cg	coarse grained	LSCM	laser scanning confocale microscope
cLR	constant load rate	m	strain rate sensitivity
CSM	continuous stiffness measurement	ν	Poisson's ratio
cSR	constant strain rate	n	stress exponent
DSC	differential scanning calorimetry	P_{max}	maximum load
ϵ	geometry constant	Q	activation energy
E	Young's modulus	R	universal gas constant
E_r	reduced modulus	rex	recrystallized
EBSD	electron back-scatter diffraction	RT	room temperature
EDS	energy dispersive X-ray spectroscopy	S	contact stiffness
fcc	face-centered cubic	SEM	scanning electron microscope
G'	pre-exponential factor	T	temperature
H	hardness	T_m	melting temperature
h_c	contact depth	ufg	ultra-fine grained
h_f	remaining indentation depth	V^*	apparent activation volume
h_{max}	maximum indentation depth	XRD	X-ray diffraction

1 Motivation and Aim of the Thesis

Since the ground breaking work of Oliver and Pharr in 1992 [1] nanoindentation has been established as a versatile tool to probe mechanical properties on a local scale. Nowadays, techniques have been developed to investigate not only hardness and elastic modulus, but also strain rate sensitivity and activation volume, creep properties, fracture toughness and even stress-strain response of a material of interest can be extracted with an adequate experimental setup. Further expansions combined nanoindentation setups with micron-sized sample geometries *e.g.* shaped through focused-ion beam milling, enabling micro-mechanical experiments that include pillar compression, cantilever bending, tensile tests or fatigue experiments.

The above described analysis methods were originally designed for testing at room temperatures (RT). However, with emergence of in-house developments or commercially available heating systems, high temperature (HT) micromechanical experiments became accessible to the community. While the maximum testing temperature was limited to roughly 500 °C until the middle of the past decade for various reasons, experimental improvements led to a shift of this restraints to a temperate range, where modern high temperature materials are applied. For the development of new high performance components it is essential to assess and understand the origin of the materials behavior in such harsh environments. Therefore, it is of particular interest for both, academics as well as industrial applicability, to advance the availability of such HT nanoindentation systems in order to investigate reliably the temperature dependent material properties in small dimensions.

In this thesis a systematic introduction of a newly acquired InSEM-HT nanoindentation system from Nanomechanics Inc./KLA was conducted, allowing *in-situ* experiments up to 1000 °C. A special focus is placed on the development of HT methods for a better understanding of the experimental setup and thermal management to ensure reliable data extraction as well as limitations of the system. Further, dominating deformation mechanisms were investigated and possible fields of application were highlighted to lay the cornerstone for future materials development.

As a materials class of interest, body-centered cubic (bcc) metals with a spotlight on technically pure tungsten and its alloys was chosen. The influence of binary alloying elements on the deformation behavior of both, the coarse grained (cg) and ultra-fine grained (ufg) microstructural condition, is rarely discussed in literature, especially for operational temperatures exceeding 500 °C. Furthermore, a proof of concept for investigating a bulk phase transformation and its respective influence on the dominating plastic deformation behavior applied on cobalt as a model material was conducted.

The aim of this thesis is thus to get a better understanding of thermally activated deformation processes investigated on a local scale. Reliable data extraction from micromechanical HT investigations should open a pathway into future high performance materials developments.

2 Nanoindentation - State of the Art

Nanoindentation, also known as instrumented indentation testing or ultra-low-load indentation is a technique that was developed in the early 1980s. The aim of these initial research studies was to evolve a tool, which is capable of measuring the influence of ion implantation into materials just a few ten nanometers below the surface [2, 3]. Since then, the capability of this tool has made a remarkable evolution, allowing the determination of all kinds of materials attributes in a variety of environments and can therefore be truly called a mechanical properties microprobe.

2.1 Conventional Nanoindentation Testing

In a nanoindentation experiment an indenter of well-known geometry is pushed into the material of interest and force and displacement are detected. From the corresponding load-displacement curve, hardness, H , and Young's modulus, E , can be derived according to the analysis of Oliver and Pharr [1]. The fundamentals of this technique are briefly described in this section, for further details the readers are referred to [1, 4, 5].

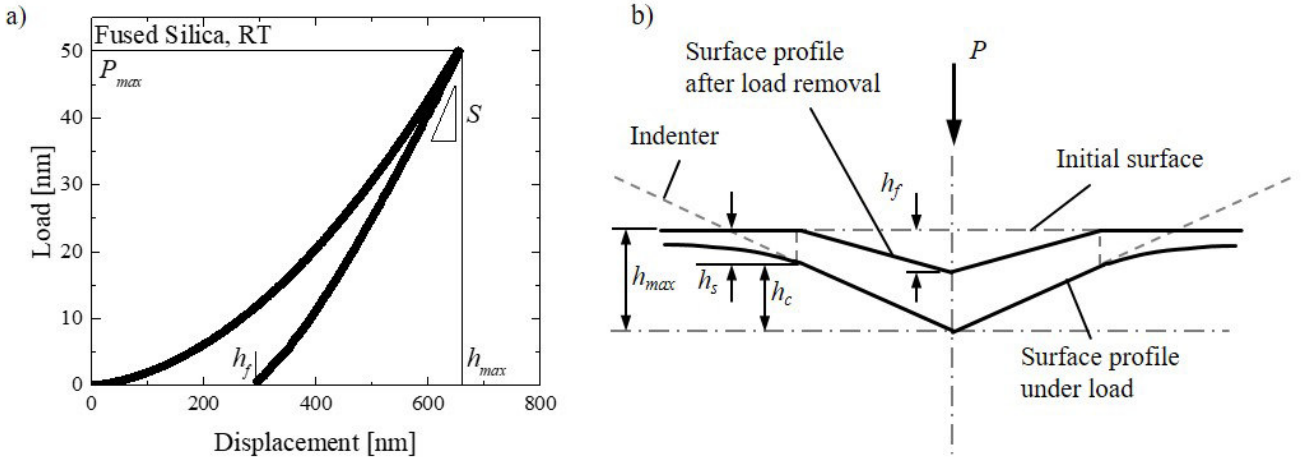


Figure 2.1: Nanoindentation analysis according to Oliver and Pharr [1]: a) Load-displacement response of a RT indentation on the reference material fused silica indicating P_{max} and h_{max} as well as S during unloading. b) Represents a schematic view of the indenter profile.

From a load-displacement curve, shown in Fig. 2.1a, the maximum load P_{max} and the corresponding maximum indentation depth h_{max} as well as the contact stiffness S , derived from the slope at the point of unloading (h_{max}) can be obtained. After unloading an indent with the final depth h_f remains in the materials surface. The contact depth h_c that deviates from h_{max} by the displacement of the surface at the perimeter of the contact, h_s , can be calculated from Eq. 2.1 with ϵ being a geometry factor of 0.75 for a standard Berkovich indenter.

$$h_c = h_{max} - h_s = h_{max} - \epsilon \cdot \frac{P_{max}}{S} \quad (2.1)$$

The projected contact area A_c as a function of h_c can be obtained from a calibration procedure on an elastic-plastic isotropic material. Conventionally, fused silica ($E = 72$ GPa) is used for that purpose. The tip geometry can be described by a polynomial function of h_c :

$$A_c(h_c) = a_0 h_c^2 + a_1 h_c + a_2 h_c^{1/2} + a_3 h_c^{1/4} + a_4 h_c^{1/8} + \dots \quad (2.2)$$

a_0 is a geometry factor depending on the opening angle of the indenter (24.5 for a perfect Berkovich tip) and a_i are fitting parameters. From the knowledge of $A_c(h_c)$, H and the reduced modulus, E_r , (Eqs. 2.3 and 2.4) can be calculated at the point of unloading. The depth-independent geometry factor β is 1.034 for a Berkovich tip geometry.

$$H = \frac{P_{max}}{A_c(h_c)} \quad (2.3)$$

$$E_r = \frac{\sqrt{\pi}}{2\beta} \cdot \frac{S}{\sqrt{A_c(h_c)}} \quad (2.4)$$

The reduced modulus can finally be used to assess the Young's modulus of the investigated material:

$$\frac{1}{E_r} = \frac{1 - \nu^2}{E} + \frac{1 - \nu_i^2}{E_i} \quad (2.5)$$

where ν is the Poisson's ratio of the test material, and E_i and ν_i are the elastic modulus and Poisson's ratio, respectively, of the indenter.

2.2 Dynamic Nanoindentation Analysis

Static nanoindentation allows the determination of Young's modulus and hardness at the peak load/displacement, as the contact stiffness is dependent on the displacement and can only be determined from the unloading curve (Fig. 2.1a). An alternative approach to create a deliberately elastic contact is to superimpose an oscillation that is small enough to produce only elastic deformation. This led to the development of the continuous stiffness measurement (CSM) technique [6, 7]. By design, modern nanoindentation systems are manufactured to be harmonic oscillators with a mass represented by the indentation column including the indenter tip, the springs that support the indenter column are well modeled by a single spring and the displacement gauge is the primary source of damping. Applying a sinusoidal force signal on the quasi-statically increasing load on the sample and simultaneously measuring the resulting displacement amplitude as well as the phase angle between the two allows for the determination of the contact stiffness over indentation depth (Fig. 2.2). As a consequence hardness and Young's modulus can also be calculated continuously over displacement.

Apart from the obvious advantages when applying dynamic nanoindentation to materials with a gradient in mechanical properties, the CSM method has also led to advanced testing protocols, allowing the determination of the local strain rate sensitivity [8, 9] or creep stress exponent [10, 11]. The techniques relevant in this thesis will be further outlined in section 2.3.

Despite the improvements made by the CSM method, its accuracy has sometimes been critically questioned. *E.g.* it was suggested that local fatigue damage might be induced by the periodic oscillation, influencing the extracted mechanical properties [12]. This was found partly true, but only for much larger

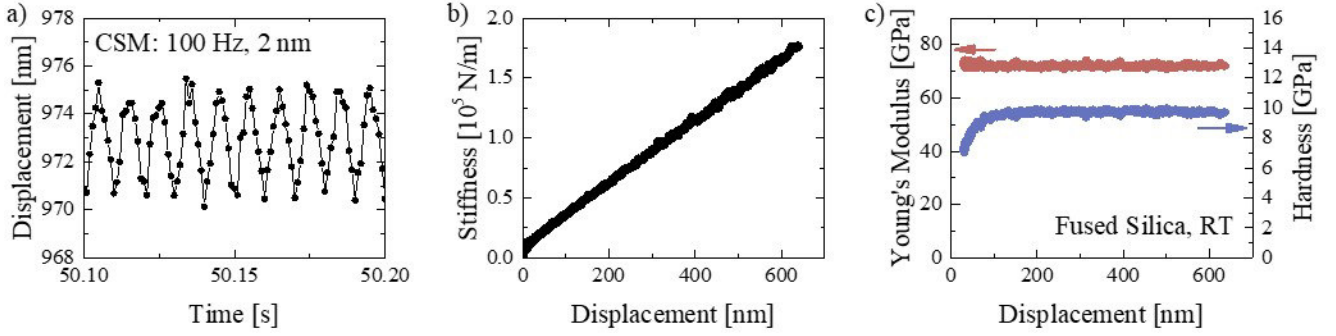


Figure 2.2: Dynamic nanoindentation of fused silica: a) Displays the CSM signal with a frequency of 100 Hz and a displacement amplitude of 2 nm. b) The enabled continuously recorded stiffness over indentation depth. c) The resulting continuously measured Young’s modulus and hardness over displacement.

displacement amplitudes than usually applied during nanoindentation [13]. Pharr *et al.* [14] showed that for materials with a high E/H ratio the CSM signal can lead to a systematic bias in the observed contact stiffness. More recently, Merle *et al.* [15] confirmed these observations for indentations with a Berkovich tip, highlighting the worst-case combination of a slow CSM signal with a high E/H ratio of the sample, resulting in a significant plasticity error. They advised careful observation of the dynamic phase angle, which should be negligible during the whole measurement to confirm validity of the obtained stiffness signal.

2.3 Probing Thermally Activated Processes with Nanoindentation

The fundamentals for thermal activation analysis is to evaluate a time dependent materials response during strain rate changes, creep loading or stress relaxation. In all these experiments the strain rate sensitivity is one key criterion for a successful analysis. The following discussion relates to pyramidal indenter tips that apply a constant indentation strain depending on the opening angle [16, 17]

2.3.1 Constant Indentation Strain Rate Experiments

The simplest way to perform an indentation experiment is to apply a constant load rate (cLR). For such a loading scenario the applied load increases linear with the time of the experiment to a preset maximum load. Lucas and Oliver [10] showed that a constant indentation strain rate (cSR) can successfully be conducted with a proportional loading protocol. According to their findings, the indentation strain rate can be described as follows:

$$\dot{\epsilon} = \frac{\dot{h}}{h} = \frac{1}{2} \left(\frac{\dot{P}}{P} - \frac{\dot{H}}{H} \right) \approx \frac{1}{2} \frac{\dot{P}}{P} \quad (2.6)$$

Applying Eq. 2.6 to cLR experiments outlined, that for conventional methods the indentation strain rate varies for loading times and load levels [18]. Leitner *et al.* [19] further pointed out that when contact stiffness and thus the mechanical properties are evaluated from the unloading curve, the holding segment at constant peak load influences thereby directly the applied strain rate sensitivity. Hence, the cSR

loading profile applied during dynamic nanoindentation testing is the most advantageous and reliable way to investigate a materials deformation behavior at constant indentation strain rate.

2.3.2 Strain Rate Jump Tests

Further improvement in the evaluation of thermally activated processes with nanoindentation techniques were achieved, when Maier *et al.* [9] and Alkorta *et al.* [8] introduced the so-called indentation strain rate jump tests. While for macroscopic tension or compression experiments the examination of flow stress after an abrupt change in the applied strain rate is state-of-the-art, its introduction to micromechanical investigations and the transferability to uniaxial stress state experiments opened a whole new field of research.

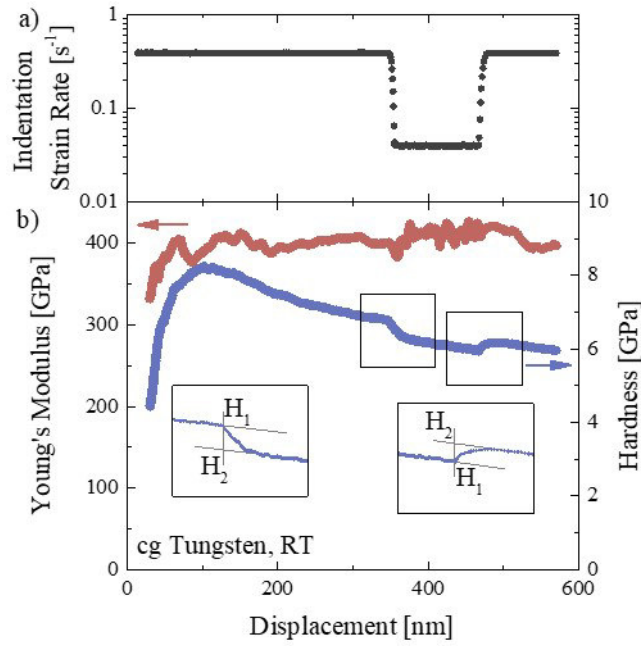


Figure 2.3: Strain rate jump tests applied to cg W at RT: a) Set indentation strain rate over displacement. b) Corresponding Young's modulus and hardness with the highlighted changed hardness response upon the changed strain rate.

Nanoindentation strain rate jump tests allow for adjustment of the applied strain rate/displacement protocol as the indenter is pushed into the material (Fig. 2.3a). Depending on application and material, the required parameters can be chosen independently. While the recorded Young's modulus should be independent of the applied strain rate, in the case of a strain rate sensitive material, the hardness can change remarkable. This is shown for coarse grained tungsten at room temperature in Fig. 2.3b. From the change in hardness, the strain rate sensitivity, m and the apparent activation volume, V^* , can be calculated [9]:

$$m = \frac{\partial(\ln(H))}{\partial(\ln(\dot{\epsilon}))} \quad (2.7)$$

$$V^* = \frac{C^* \cdot \sqrt{3} \cdot k_B \cdot T}{m \cdot H} \quad (2.8)$$

where C^* is a constraint factor of 2.8 [17, 20], k_B is the Boltzmann constant and T the absolute temperature. The knowledge of these materials parameter give a hint on the dominating deformation process as discussed in section 5.4.

To highlight the large variation of materials behavior during nanoindentation strain rate jump tests, in Fig. 2.4 hardness is plotted over displacement for Ta2.5W in varying microstructural condition and a large temperature range: a) represents the single-crystalline behavior of a cg material, while the samples in b) and c) exhibit an ufg structure mainly consisting of high-angle grain boundaries (HAGB) and low-angle grain boundaries (LAGB), respectively. The impact of a changed deformation mechanism, thermally activated dislocation-impurity interaction or thermo-mechanical grain growth can be read off these curves. A detailed analyses is given in **Publication D**.

2.3.3 Extraction of the Activation Energy for Plastic Deformation

While a change in strain rate sensitivity and activation volume do indicate a possible change in the rate-controlling mechanism, they are insufficient to confirm a mechanistic transition. Resolving those parameters over temperature, however, further encourages the extraction of the activation energy Q . Being a thermodynamic parameter for thermally activated plasticity, a change in Q can provide certainty for the underlying deformation mechanism. Several evaluation techniques exist for the extraction of Q , for example those described in Refs. [21–23].

Following the hot-hardness analysis of Sherby and Armstrong [24], the activation energy can be derived from a temperature dependent hardness and Young’s modulus as follows:

$$\frac{H}{E} = G' \cdot \exp\left(\frac{Q}{nRT}\right) = G' \cdot \exp\left(\frac{Qm}{RT}\right) \quad (2.9)$$

G' is a pre-exponential factor, R the universal gas constant ($8.3145 \text{ J mol}^{-1} \text{ K}^{-1}$) and n the stress exponent, which relates to the strain rate sensitivity $m = 1/n$.

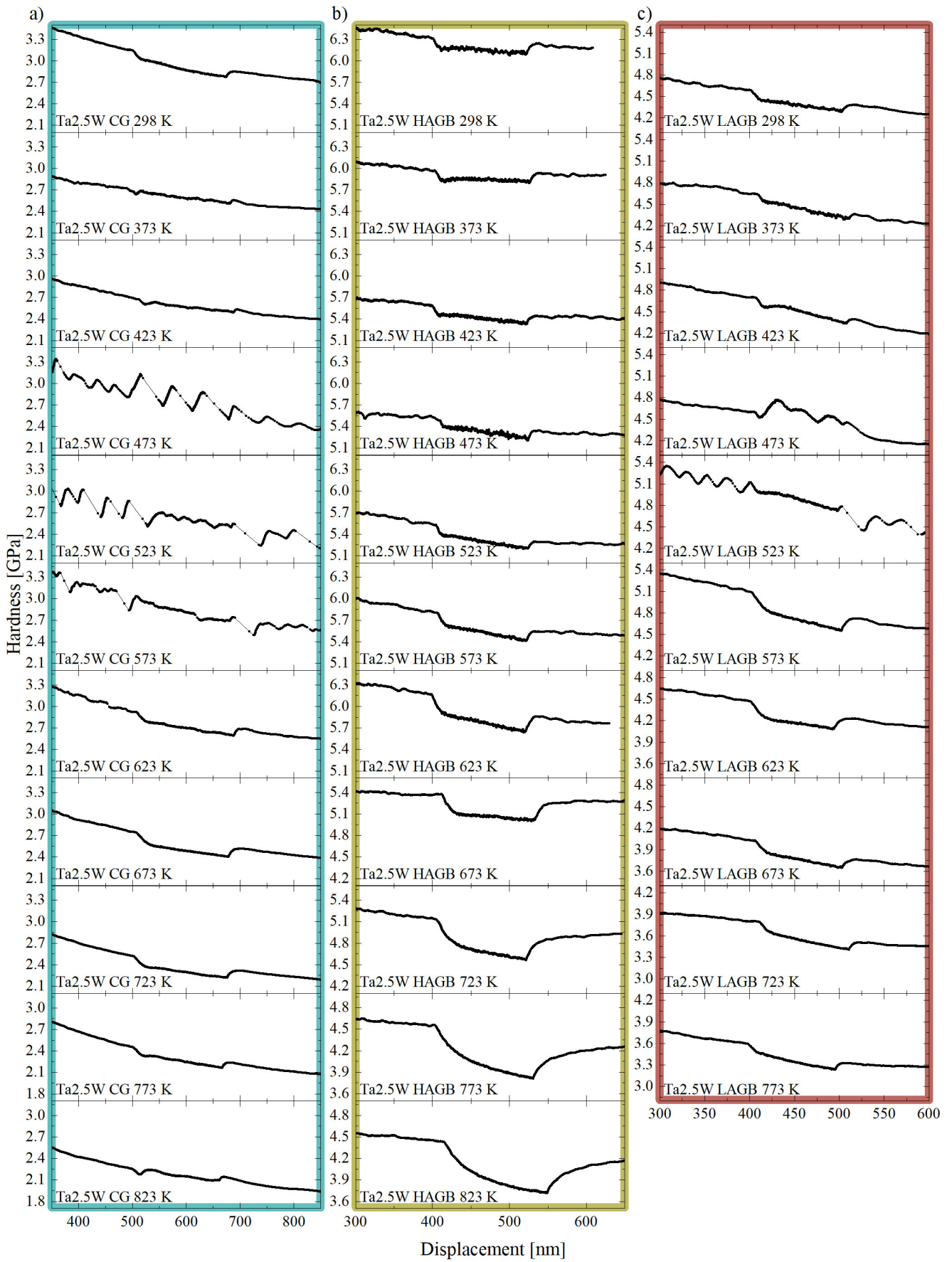


Figure 2.4: Hardness over displacement of Ta_{2.5}W at a wide range of temperatures for varying microstructural condition: a) cg, as well as ufg samples consisting mainly of b) HAGB and c) LAGB.

3 Implementation of a New High Temperature Nanoindentation System

High temperature nanomechanical testing techniques, mostly nanoindentation and micro-pillar compression, became increasingly popular over the last years. This is owed to a decreasing length scale of devices, the lower cost of sample fabrication, and higher speed of indentation testing. While most commercial nanoindentation system manufacturers now offer a high temperature option, the success of these systems is mainly dependent on the thermal controls implemented in the system [25]. A brief review on this topic and how these challenges were faced in this thesis is summarized in sections 3.2 and 3.3.

In the first half of the 2010s, the maximum achieved temperature in nanomechanical systems reached a plateau at around 500 °C [26], mainly due to the lack of appropriate indenter material for high temperature applications. In 2017 Gibson and co-workers [27] finally broke the sonic barrier of nanoindentation up to 1000 °C. Their success was possible, amongst other things, due to the development of new indenter tip materials. This topic will be addressed in section 3.4.

3.1 The InSEM-HT System

The high temperature nanoindentation system mainly used for experiments in this thesis is the InSEM-HT from Nanomechanics Inc./KLA (Oak Ridge, TN) as illustrated in Fig. 3.1. It is based on an InForce 50 nanomechanical actuator with an electromagnetic load application to a maximum force of 50 mN and a capacitive displacement sensor. Typical noise levels are below 0.1 nm in displacement and <50 nN for the force signal. It is equipped with a CSM unit (section 2.2) and mounted in a scanning electron microscope (SEM) Tescan VEGA3 (Tescan, Brno, Czech Republic) to maintain the indentation process and to exclude for oxidation of the sample or indenter at elevated temperatures.

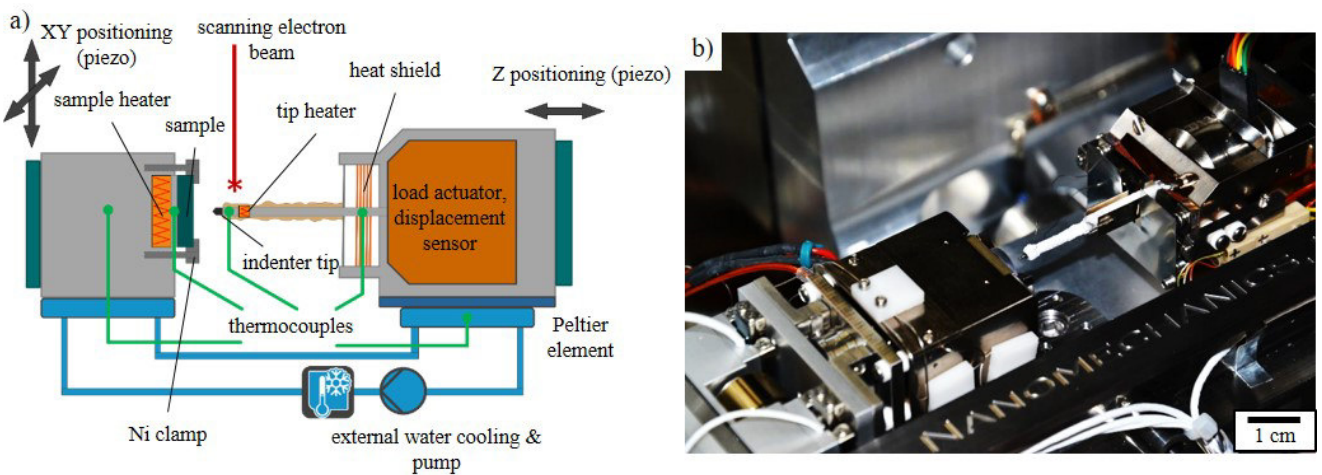


Figure 3.1: The InSEM-HT nanoindenter system, a) schematically illustrated and b) an image of the actual experimental setup.

Precise indent positioning is achieved with linear piezo stages at an accuracy below 1 μm . Tip and

sample can be heated independently up to 1000 °C with a PID-controlled feedback loop, while temperatures can be accurately supervised with a number of thermocouples. Heating is conducted with electric resistance heating elements. To achieve thermal stability even at high temperatures, Peltier elements as well as an external water cooling cycle are implemented. The sample is mechanically clamped to the sample heater, with a small Mo platelet in between, where a small slit for a thermocouple allows for measuring the sample temperature.

3.2 Thermal Gradients and Tip Temperature Calibration

Knowing the temperature distribution and thermal gradients within a HT nanoindentation system is crucial for valid data evaluation. This is achieved by a number of thermocouples, however, temperature measurements directly at the point of contact between indenter and sample surface are impossible for obvious reasons. A thermal gradient exists between the tip thermocouple and the actual indenter tip. Temperature differences of up to 40 % are reported [25] between the measuring point and the point of interest. Therefore, a calibration procedure needs to be performed every time when a new indenter tip is used. This can be either achieved by direct indentation of a thermocouple, Raman spectroscopy or infrared thermometry as summarized in [28]. If the actual contact temperature is known as a function of the measured tip temperature, further experiments exhibit precise awareness of the investigated temperature.

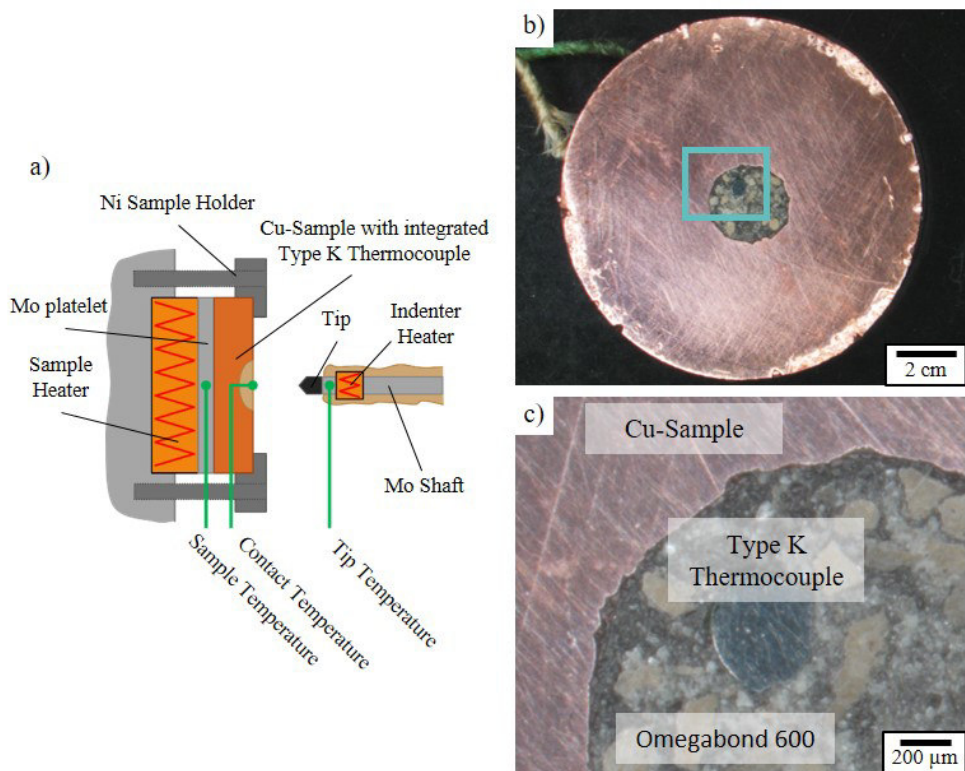


Figure 3.2: Experimental setup for a tip temperature calibration: a) Schematic illustration of the procedure. b) Overview and c) details of the thermocouple mounted in a Cu sample.

On the InSEM-HT system, successful tip temperature calibrations were achieved by direct indentation of a thermocouple, as schematically drawn in Fig. 3.2. While tip degradation at elevated temperatures

needs to be considered with this high temperature contact method (see Sec. 3.4), the simplicity of the experimental setup is advantageous. A 2.5 mm thick disc of Cu was used as a holder for the type K thermocouple, due to its high thermal conductivity. Holes were drilled for the cable feedthrough and the thermocouple was fastened with a ceramic high temperature glue OmegabondTM600 (Omega Engineering Inc., Deckenpfromm, Germany). This high temperature cement has a relatively high thermal conductivity, while at the same time it is electrically insulating. The sample prepared in this way was then carefully ground to a relatively smooth finish with a SiC sandpaper #4000 (Figs. 3.2b and c).

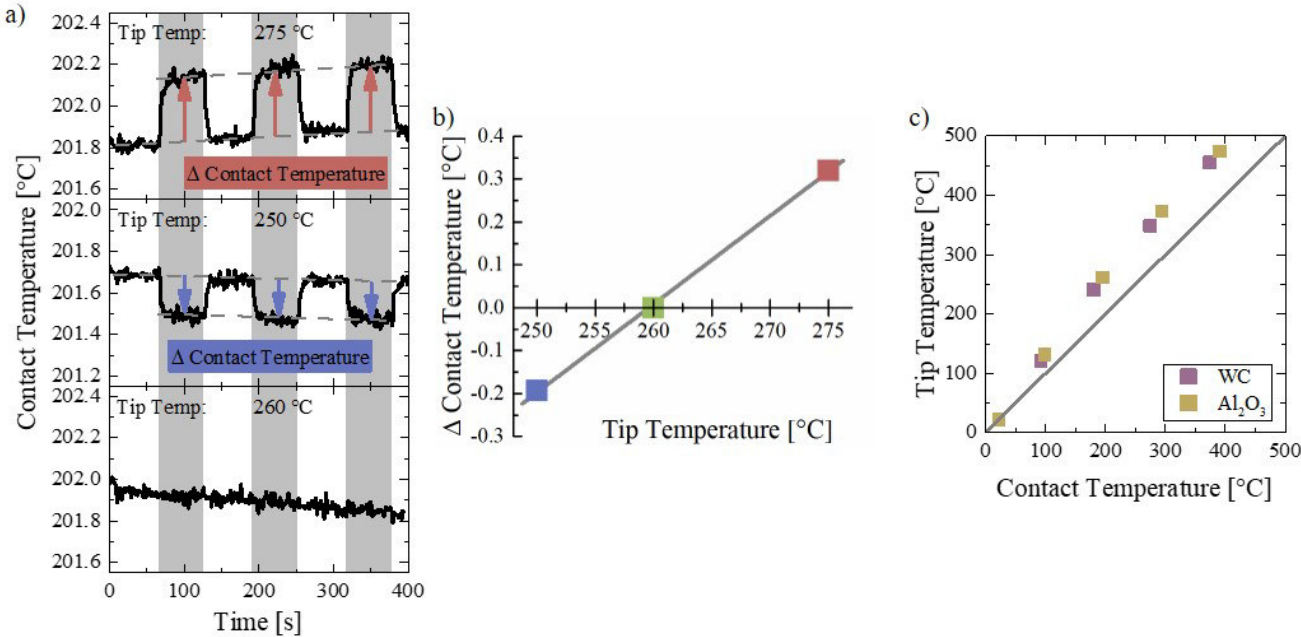


Figure 3.3: Tip temperature calibration: a) Temperature response of the contact temperature thermocouple during multiple loading steps. b) Shows how thermal equilibrium was achieved by variation of the tip temperature. In c) the resultant tip temperature is plotted as a function of contact temperature for two different indenter materials.

Isothermal contact was achieved by examination of the signal of the contact thermocouple, as it was found to be very sensitive to temperature differences between indenter and sample surface. By repeatedly connecting the indenter with the thermocouple (shaded grey in Fig. 3.3a) a shift in contact temperature can be examined and through a linear approach isothermal contact can be achieved [29] (Fig. 3.3b). Reiterating this procedure at different temperatures gives a calibration curve of tip temperature over contact temperature for a certain indenter material. As an example, the result of this procedure is shown in Fig. 3.3c for a WC and a Al₂O₃ indenter. The curves lie on top of each other, indicating an almost identical thermal gradient within the different tips. This is owed to the very similar thermal conductivity of WC and Al₂O₃ [26].

Performing high temperature indentation experiments on sample materials and examining the temperatures at isothermal contact revealed that the thermal gradient between tip and sample measured during an experiment coincide with the those from the tip temperature calibration. In other words, the temperature difference between tip and sample is identical, within measurement inaccuracy, to the one between tip and contact during the above described calibration procedure. It can therefore be concluded,

that the thermal gradient within the measured sample is negligible in the system, as long as the thermal conductivity is sufficiently high. This observation was made for a variety of materials, including body-centered cubic and face-centered cubic metals and alloys as well as thin-film coatings on a silicon substrate.

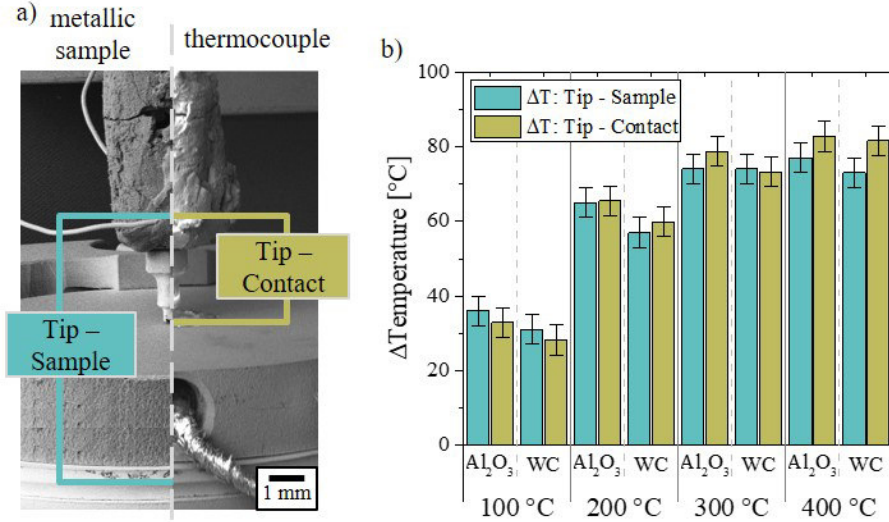


Figure 3.4: a) SEM images of the indenter in contact with a sample material and the prepared contact thermocouple to illustrate the points of temperature measurement. b) Compares the occurring temperature differences during actual measurements on a metallic sample and the tip temperature calibration for two different indenter materials.

3.3 Thermal Drift and Temperature Matching

Thermal drift is a time dependent shift in displacement measurements that occurs due to thermal expansions within the indenter system. The necessity for measuring length scales in the nanometer range causes significant thermal drift for temperature variations as small as one degree Celsius. Thermal drift can be split into two contributions, frame drift and contact drift [28]. Separating between the two and knowing their cause is important to be able to take appropriate actions to counter the specific source of error.

Frame drift is caused by thermal expansion of the frame, caused by temperature variations away from the contact. At ambient temperatures it may occur through variation of atmospheric conditions, and is generally accounted for through a hold segment at lower loads after indentation, assuming a linear behavior with time. Utilizing the experiments in a sealed cabinet or enclosure with a stabilization time can minimize frame drift and the linear approach is accurate for standard test times below 30 min. Longer duration testing requires more complex considerations as described in [11]. For elevated temperature testing the frame drift arises from changing thermal gradients between the heaters and the cooled components and is independent of the contact. This drift component will decrease with time, as thermal gradients are established and thermal expansion desists, which is generally described as the stabilization time [28]. Its duration is in the range of an hour after reaching the desired testing temperature, but

depends on the experimental temperature, the thermal conductivity of the components and the power of the cooling system.

Contact drift occurs due to heat flow between the indenter and sample surface at the contact, caused by a temperature difference between them. For ambient testing conditions this is negligible. At high temperature testing, however, a temperature mismatch between tip and sample becomes increasingly significant for thermal drift. Several factors influence the amount of heat flow [25]: thermal gradient, contact area, materials properties and pressure. As several of these factors vary during indentation, contact drift is non-linear with time [25, 30].

In order to keep thermal drift at a minimum during load-displacement measurements, both types of drift have to be minimized prior to the actual experiment. Frame drift can be minimized by an appropriate waiting time for the thermal gradients within the system to stabilize. The waiting time depends on the components of the indenter system, the previous heating rate and the desired temperature. As thermal radiation appears at higher temperatures, the stabilization usually increases with the target temperature. Contact drift on the other hand can only be avoided, if the surface of the sample exhibits the same temperature as the indenter tip. Therefore, a temperature matching procedure has to be carried out.

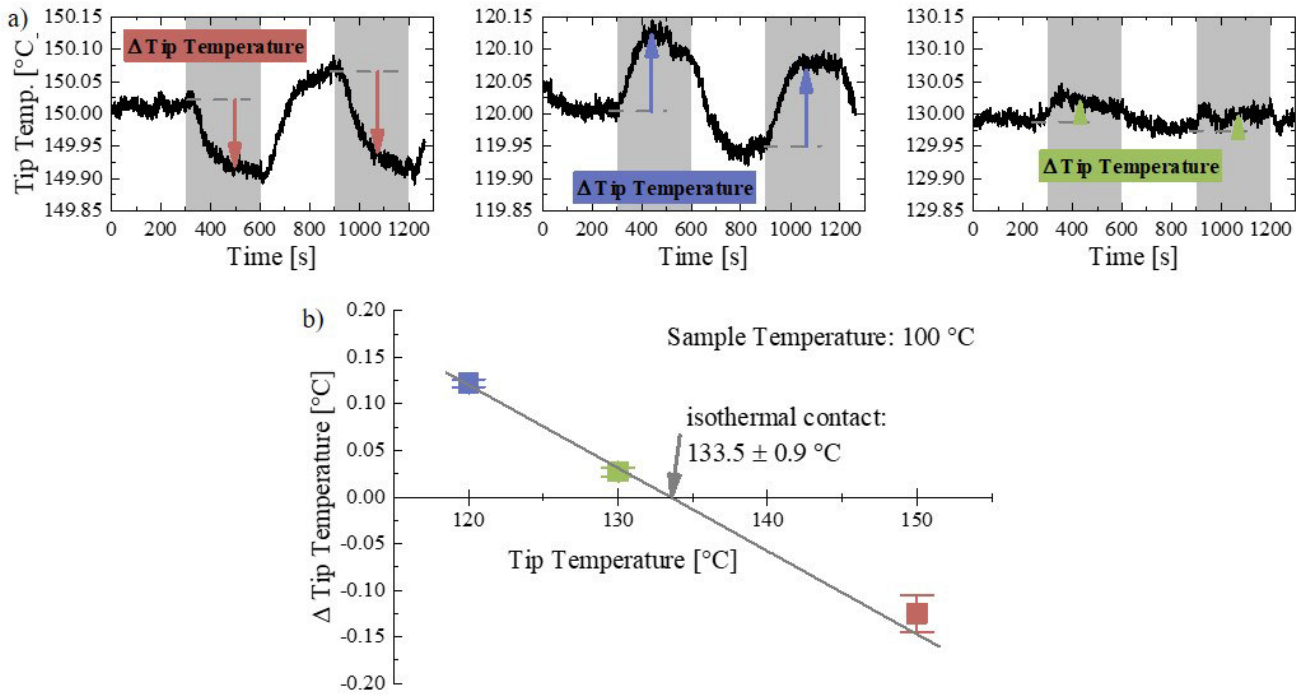


Figure 3.5: Temperature matching based on thermal feedback during contact: a) Temperature response of the tip thermocouple during multiple loading steps. b) Shows how isothermal contact temperatures can be estimated.

To achieve thermal equilibrium between tip and sample, a temperature matching procedure is required. Two methods have been proposed in literature for tuning indenter and sample temperature: using thermal drift [30, 31] or observation of the tip thermocouple signal to evaluate heat loss or gain during contact [25, 29]. Performing the latter on the InSEM-HT system is illustrated in Fig. 3.5. In Figs. 3.5a a shift in

the tip temperature can be observed during contact (shaded grey) due to a thermal mismatch between indenter and sample. In case of a hotter tip than sample surface its temperature decreases due to heat loss, while a cooler tip results in a rising temperature signal. From the observed temperature change (Δ Tip Temperature) the isothermal contact can be estimated through a linear approach (Fig. 3.3b). However, it was found that on the InSEM-HT system this procedure has several drawbacks: The change in temperature signal is rather weak and sluggish. This is related to the position of the thermocouple, around 3 mm (see Fig. 3.4a) away from the actual contact. As a consequence, even a large thermal mismatch of more than 15 °C results in a change in the temperature signal of only around 0.12 °C. To get a change in signal at all, high contact forces (close to 50 mN) as well as long contact times (several minutes) are required. Both these requirements are disadvantageous for diffusion processes between indenter and sample and consequent tip degradation (see section 3.4) at high temperature testing.

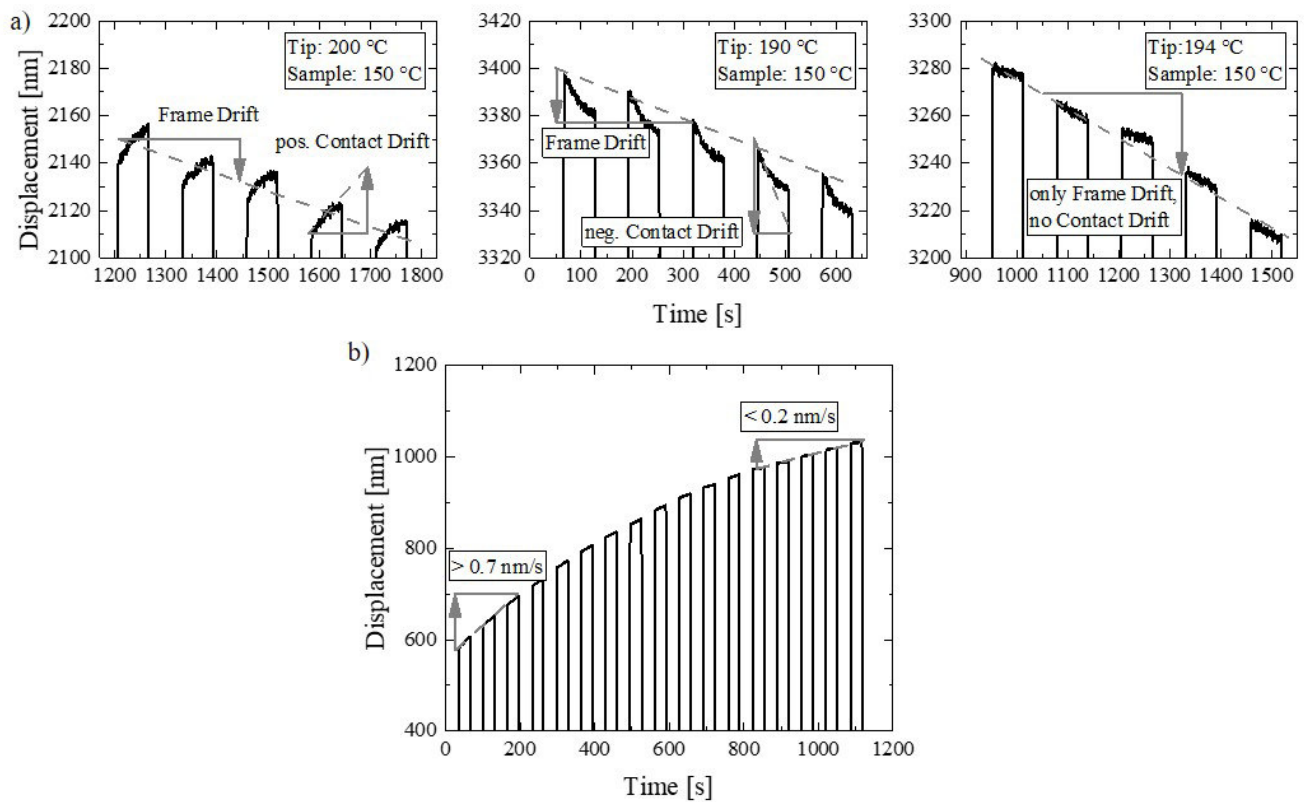


Figure 3.6: Temperature matching based on thermal expansion affecting the displacement signal: a) Displacement response during the temperature matching procedure at different tip temperatures. b) Decreasing frame drift during the stabilization period.

Therefore, a temperature matching procedure was developed in cooperation with Nanomechanics Inc./KLA that takes advantage of the accurate displacement measurement affected by thermal expansion. Thereto, the indenter is repeatedly brought into contact with the sample at a given force (*e.g.* 5 mN) and the resulting displacement is examined (Fig. 3.6a). This allows for distinguishing between the two drift components: Frame drift linearly superimposes the observed displacement signal and does not change significantly within the investigated time interval of 600 s. Contact drift on the other hand causes an immediate, non-linear change in the displacement signal due to thermal expansion/retraction

of the indenter. Due to the larger thermal mass of the sample the tip is thus stronger affected by thermal induced length variation. The observed displacement signal in Fig. 3.6a is interpreted as follows: A hotter indenter initiates heat flow from tip to sample upon contact, causing the tip temperature to decrease and results in thermal retraction of the indenter. Consequently, the displacement increases and thus a positive contact drift is observed. This process is reversed for a cooler indenter. Heat flow from sample to tip causes thermal expansion, leading to a decreasing displacement signal and a negative contact drift.

As this procedure allows to distinguish between frame drift and contact drift, the stabilization time required for thermal gradients within the nanoindenter system to established can be carefully adhered to. This is illustrated in Fig. 3.6b, where a noticeable reduction of the frame drift from 0.7 nm s^{-1} to below 0.2 nm s^{-1} is observed. The drift decreases asymptotically and generally higher testing temperatures require longer stabilization times. While this procedure does not allow for quantitative approaching of the tip temperature towards thermal equilibrium, it is beneficial in terms of high temperature tip degradation due to low contact forces and short contact times.

3.4 Choice of Indenter Material and Tip Degradation

While the introduction of high vacuum techniques enabled the problem of oxidation of diamond indenters to overcome [32], the choice of tip material is still a major concern in the HT nanoindentation community. Diamond was successfully used for investigations of Ni-base alloys up to $800 \text{ }^\circ\text{C}$ [33]. Sapphire was shown to work for a PM2000 ODS steel up to $700 \text{ }^\circ\text{C}$ [34], Ni-base superalloys and thermal barrier coatings [27] up to $1000 \text{ }^\circ\text{C}$, as well as for Ni and Mo up to $1100 \text{ }^\circ\text{C}$ [35]. Cubic boron nitride cBN exhibited promising results for testing Inconel 617 alloy up to $800 \text{ }^\circ\text{C}$ [36] as well as W up to $950 \text{ }^\circ\text{C}$ [37, 38]. However, as no failed attempts are published and no comprehensive data base exists, the choice of the suitable indenter material still depends on trial-and-error and the experience of the user to conduct successful experiments.

The property requirements for indenter materials are extensive due to the combination of high temperatures and contact pressures. Most importantly, it should have a high hardness that does not decrease significantly with increasing temperature. In order to successfully generate plastic deformation in a sample material, the hardness of the indenter must be at least 20 % higher [39, 40]. To prevent rapid blunting of a sharp indenter tip, however, the hardness of the indenter material has to be significantly higher ($>100 \%$). Even if an indenter is sufficiently hard to plastically deform a sample material, chemical reactivity between itself and the investigated material may potentially demolish the original tip geometry. The classical example for this is indentation of steel with a diamond tip at elevated temperatures. Fe, as a strong carbide former dissolves the diamond tip at $500 \text{ }^\circ\text{C}$ and destroys the geometry of the indenter [26]. As for the analysis according to Oliver and Pharr [1] the indenter area function has to be known precisely for valid experimental results, these chemical reactions render the validity of the experimental results impossible.

To date, diamond, Al_2O_3 , WC, cBN, SiC and B_4C indenter tips are commercially available. For the identification of the right indenter material for a certain experiment the work of Wheeler and Michler [26] is a good guideline, although in this publication mainly diffusion processes between tip and investigated material are a criterion for suggested material pairings. However, in this thesis it was found that tip degradation by dissolution of the tip material is a minor issue even when testing in a temperature range

between 400 and 800 °C. A more crucial role comes to wetting and consequently adhesion of parts of the investigated material on the tip. The calibrated tip area function is thereby changed and no valid indents can be performed anymore. In particular, when materials are tested at high homologous temperatures (above 0.6 of their melting temperature, T_m) this problem was observed. This is demonstrated in Fig 3.7, where a WC-tip was used to investigate a precipitation hardened aluminum alloy AA7050 up to 400 °C.

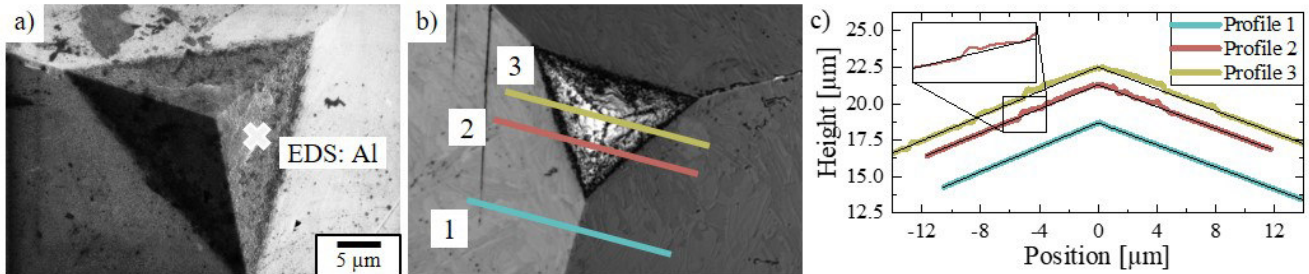


Figure 3.7: Investigations on a WC tip after testing an AA7050 aluminum alloy at 400 °C. a) SEM image taken in BSE mode with EDS detection of Al. b) LSCM intensity image with coloured lines indicating the position of height profiles. c) Profile of the tip at three different positions corresponding to image b).

SEM images taken in back scattered electron (BSE) mode reveal, that the basic geometry of the three-sided Berkovich tip is still extant. Large amounts of Al could be detected via energy dispersive X-ray spectroscopy (EDS) (Fig. 3.7a) along the contact area that appears darker in the BSE image. Profilometric investigations done with a laser scanning confocale microscope (LSCM) outlined, that additional material adhere to the shape of the tip. Thus, not dissolution of the indenter material, but permanent adhesion caused a failure of the experiment.

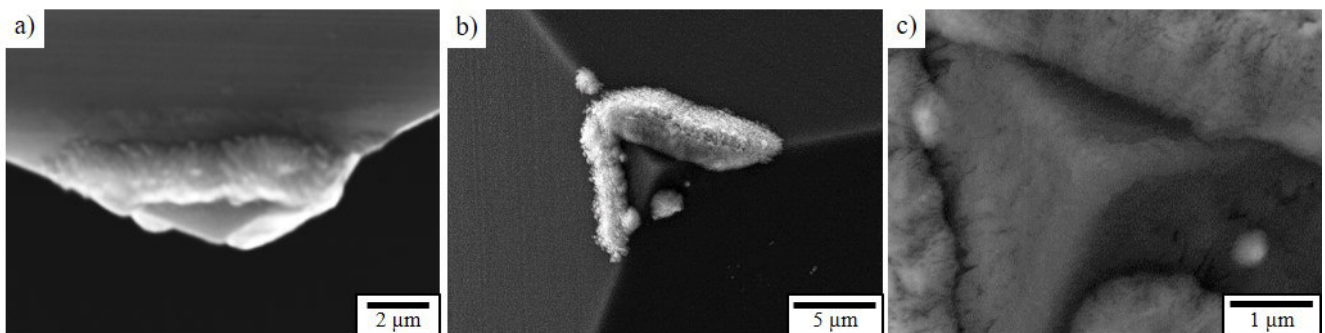


Figure 3.8: Electron microscopic observations on a SiC indenter that was used for cobalt at 700 °C. a) Shows the side view of the tip, indicating adhesion of sample material. b) The top view specifies the adhesion process along the intersection indenter/sample surface/vacuum. c) The geometry of the indenter is largely intact.

A similar problem arose when testing coarse grained metallic cobalt at 700 °C. Fig. 3.8 reveals electron microscopic observations performed on the contaminated SiC indenter. From the side view in Fig. 3.8a it can be deduced that sample material added up on the pyramidal indenter geometry. Interestingly, as can be seen in Fig. 3.8b, these adhesion processes do not happen uniformly throughout the full contact area,

but rather along the triangle of maximum indentation depth. It can be speculated that impurities, either molecules (such as oxygen) that might adhere to the surfaces or residual gas in the vacuum facilitate the adhesion process along the intersection indenter/investigated cobalt sample/vacuum. Notably, the sharp tip of the indenter (Fig. 3.8c) did not cause significant degradation through any kind of diffusion processes.

A simple way to check the validity of a HT nanoindentation experiment is to perform indents on a reference material (*e.g.* fused silica) at RT before and after elevated temperature testing. This was consequently done throughout all the HT experiments that were performed within this thesis. Additionally, this procedure allows for track of slight tip rounding when considering the analysis of hardness over displacement, as shown in Fig. 3.9 for a SiC tip. Before testing (Fig. 3.9a) a rather constant hardness value over indentation depth refers to an almost perfectly shaped Berkovich indenter. After testing one sample of ultra-fine grained (grain size around 300 nm) W up to 800 °C, the hardness evaluation (Fig. 3.9b) indicated slight tip rounding for the first 170 nm of indentation depth. Proceeding with testing of three more ufg W-Re samples suggests progressed tip rounding within the first 230 nm, but also tip imperfections at larger indentation depth of 500 nm. Examining this tip in the SEM revealed again adhesion of sample material to the tip. Interestingly, it seems that in the case of ufg sample material, single grains are lined up along the triangle that borders the contact area at maximum indentation depth.

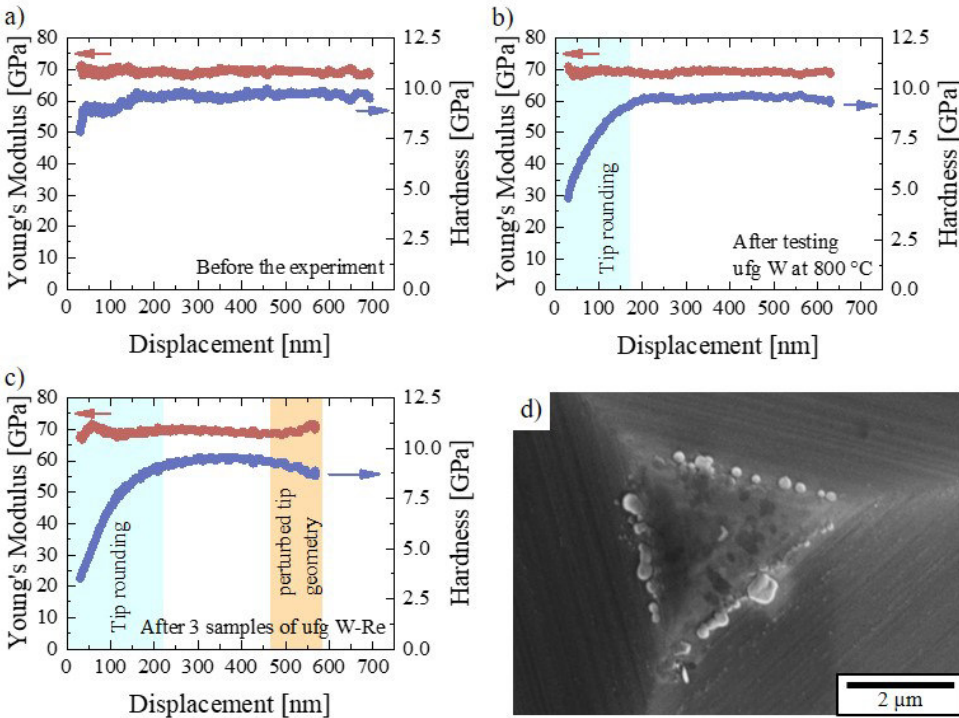


Figure 3.9: Evolution of tip degradation after high temperature nanoindentation of ufg W-Re alloys up to 800 °C. a)-c) Shows the derived Young's modulus and hardness from indentation on the reference material fused silica. d) SEM image of the indenter after testing three samples of ufg W-Re.

Various different indenter and sample material pairings were tried out during this thesis, in the following a short summary of promising combinations as well as abortive trials are described. Diamond was

successfully used for nc Al-Ni-Ce alloys up to 325 °C. Al₂O₃ indenters were used for a variety of different wrought Cu-alloys up to 500 °C and showed only slight geometrical rounding due to tip wear. WC tips for probing cg W and W-Re alloys exhibit rather advanced tip rounding, either through diffusion or wear when used up to 800 °C. WC could be well used for Al up to 300 °C, but failed at 400 °C (Fig. 3.7). Further, testing ufg Ta-alloys could be successfully accomplished up to 550 °C without noticeable change in tip geometry. The most promising tip material was SiC. Successful experiments on ufg W and W-Re alloys were conducted several times up to 800 °C with only limited tip rounding (Fig. 3.9). Metallic Co was tested up to 600 °C without any issues. While at 700 °C the sample material sticking to the tip made further experiments impossible, the geometry was not affected (Fig. 3.8). A good performance was also observed for testing Ta-alloys up to 550 °C with no sign of tip wear. The only crucial failure was observed for testing titanium-aluminides at 750 °C through a combination of wear and adhesion.

4 Application Examples

In the following section some application examples are presented to outline the versatility of nanoindentation methods for both, ambient and high temperature applications. Also a comparison between results obtained on the InSEM system and the well established nanoindenter platform G200 from KLA (CA, USA) is drawn.

4.1 Comparison Between Different Nanoindenter Platforms

As a reference material for this comparative study K-doped (60 ppm) Tungsten sheets with a thickness of 215 μm were used in the as-received, ufg, as well as recrystallized (rex) condition (2400 $^{\circ}\text{C}$ for 2 h in H_2). Micrographs of the two different states are presented in Figs. 4.1a and b, observed in transverse direction of the rolling process. The recrystallized condition was contrasted with a Murakami etchant observed in a LOM, while fine graininess in case of the ufg condition were resolved with an SEM in BSE contrast. The former exhibits large grains with a size of several ten micrometers as well as abnormal grain growth at the surface of the sheet [41]. In contrast, the grains in the ufg sample are elongated in rolling direction with a decisive grain diameter in normal direction of a few hundred nanometers.

Nanoindentation experiments were performed in normal direction of the W sheets and the surface was electrolytically polished with 2% NaOH in H_2O at 13 V for 90 s prior to the experiments. For comparison of different nanoindenter platforms the two different samples were probed with the InSEM system and a G200 platform at RT. While the InSEM can apply a maximum load of 50 mN, indentation with the G200 systems allows for a maximum force of 500 mN. Hence, the maximum achievable indentation depths (experiments were performed up to the maximum load) vary significantly between the two different systems. Also, the standard settings for indentation strain rates are different, with $\dot{P}/P = 0.05 \text{ s}^{-1}$ for the G200 and 0.1 s^{-1} for the InSEM. The CSM unit on the G200 superimposes a sinusoidal load signal resulting in a displacement amplitude of 2 nm at a frequency of 45 Hz, and while the amplitude remains the same for the InSEM, the standard frequency is 100 Hz. To account for the strain rate sensitivity additional strain rate jump tests [9] were executed, where the strain rate was reduced by an order of magnitude between 300 and 400 nm in case of the InSEM. For the G200 a reduction to 0.005 s^{-1} between 500 and 1000 nm as well as to even lower strain rates of 0.001 s^{-1} between 1500 and 2000 nm was performed.

In Fig. 4.1c and d the well matching hardness and Young's modulus over indentation depth are presented for representative indentation experiments. In all the cases the mechanical properties were extracted between 450 and 500 nm to account for variations of the hardness with displacement due to the indentation size effect [42]. The Young's modulus is independent of the indentation depth, although a slightly higher scatter in the data can be observed for experiments performed on the G200 platform. In case of the rex sample a value of 429.8 ± 14.6 for the G200 and 424.6 ± 3.4 GPa for the InSEM was measured. The higher scatter of the values over indentation depth is thus represented by a higher standard deviation in case of the G200. Slightly increased values of 438.3 ± 12.5 for the G200 and 448.1 ± 4.8 GPa for the InSEM could be found for the ufg sample material. The values are graphically

summarized in Fig. 4.1g. For W, a slightly lower Young's modulus of 405 GPa is reported [43]. As the Young's modulus should be independent of the microstructure, the remaining indentations performed with the G200 platform were further investigated by means of LOM and LSCM to investigate any possible systematic errors (Fig. 4.1e and f).

Already in the LOM images taken in differential interference contrast, to qualitatively account for differences in height, a slight convex deviation from the ideal triangular shape of the remaining indent can be seen for both samples. It is further evident, that in case of the rex microstructure, the materials pile-up along the three indenter sides is spread over a distance of several micrometers, while in case of the ufg microstructure it is locally concentrated around the remaining indent. Similar results were reported for different Al-alloys [44], with an increasing pile-up behavior for refined microstructures. It is assumed, that this is caused by the low work-hardening potential of severely deformed materials, as the plastic zone can spread over a larger volume due to work-hardening in a cg material, thus causing a lower pile-up around the indenter [45, 46]. This qualitative findings are quantitatively confirmed, when the indentations were examined profilometrically with an LSCM. Three different height-profiles (P1, P2 and P3) were extracted from the data and the maximum pile-up height was averaged. A value of 268 ± 99 nm in case of the rex sample and 340 ± 18 nm was found for the ufg microstructure. It should be noted that the larger standard deviation in case of the rex sample is not caused by strong variation between multiple indents, but rather by the pronounced difference in pile-up height of the three different indenter sides. Such a behavior can be related to the slip geometry of quasi-monocrystalline behavior and the resulting plastic anisotropy in case of the recrystallized microstructure [47]. In summary, the pile-up behavior was more pronounced for the ufg W. This leads to an underestimation of the actual contact area, causing an overestimation of Young's modulus and hardness [48] and hence explains the slightly higher values for the Young's modulus in case of the as-received sample.

From nanoindentation strain rate jump tests a slightly increased strain rate sensitivity was found for the rex sample (0.028 ± 0.006 from the G200 and 0.026 ± 0.003 in case of the InSEM) compared to 0.021 ± 0.006 (G200) and 0.017 ± 0.002 (InSEM) for the ufg microstructure. Those results are graphically summarized in Fig. 4.1h. The different values are well within standard deviation of the measurements, thus confirming the validity of the technique although performed on different platforms with varying strain rates and different indentation depths. The minor role of the indentation size effect and the related displacement dependence of hardness on the measured strain rate sensitivity was already demonstrated in [49].

As the strain rate sensitivity is known, the different indentation strain rates can be considered for the hardness values obtained in the CSR experiments according to Eq. 2.7. A summary of these considerations is graphically illustrated in Fig. 4.1i. For a certain microstructural condition the hardness was measured either at a strain rate of 0.05 s^{-1} (G200) or 0.1 s^{-1} (InSEM). The hardness for the respective other strain rate can then be calculated. In case of the rex material this returns values of 6.10 ± 0.10 GPa (G200, measured) and 6.05 ± 0.06 GPa (InSEM, calculated) for $\dot{P}/P = 0.05 \text{ s}^{-1}$. In case of the higher strain rate ($\dot{P}/P = 0.1 \text{ s}^{-1}$) a hardness of 6.16 ± 0.05 GPa (InSEM) was measured and 6.21 ± 0.11 GPa (G200) calculated. Similar considerations were carried out for the material with ufg microstructure: At $\dot{P}/P = 0.05 \text{ s}^{-1}$ a hardness of 9.02 ± 0.22 GPa (G200, measured) and 8.78 ± 0.09 GPa (InSEM, calculated) was obtained, while for $\dot{P}/P = 0.1 \text{ s}^{-1}$ values of 8.88 ± 0.08 GPa (InSEM, measured) and 9.11 ± 0.24 GPa

(G200, calculated) were extracted.

The gathered strain rate corrected hardness values obtained at varying nanoindenter platforms are within standard deviation. However, it should be noted that results obtained for the ufg material exhibit slightly higher values for experiments performed on the G200. This is probably a result of a less homogenized microstructure and possible variations of grain size through the thickness of the W sheet. The results of this case study demonstrate, that mechanical properties obtained from different nanoindenter platforms are well comparable between each other, as long as the depth- and strain rate dependence of hardness is considered.

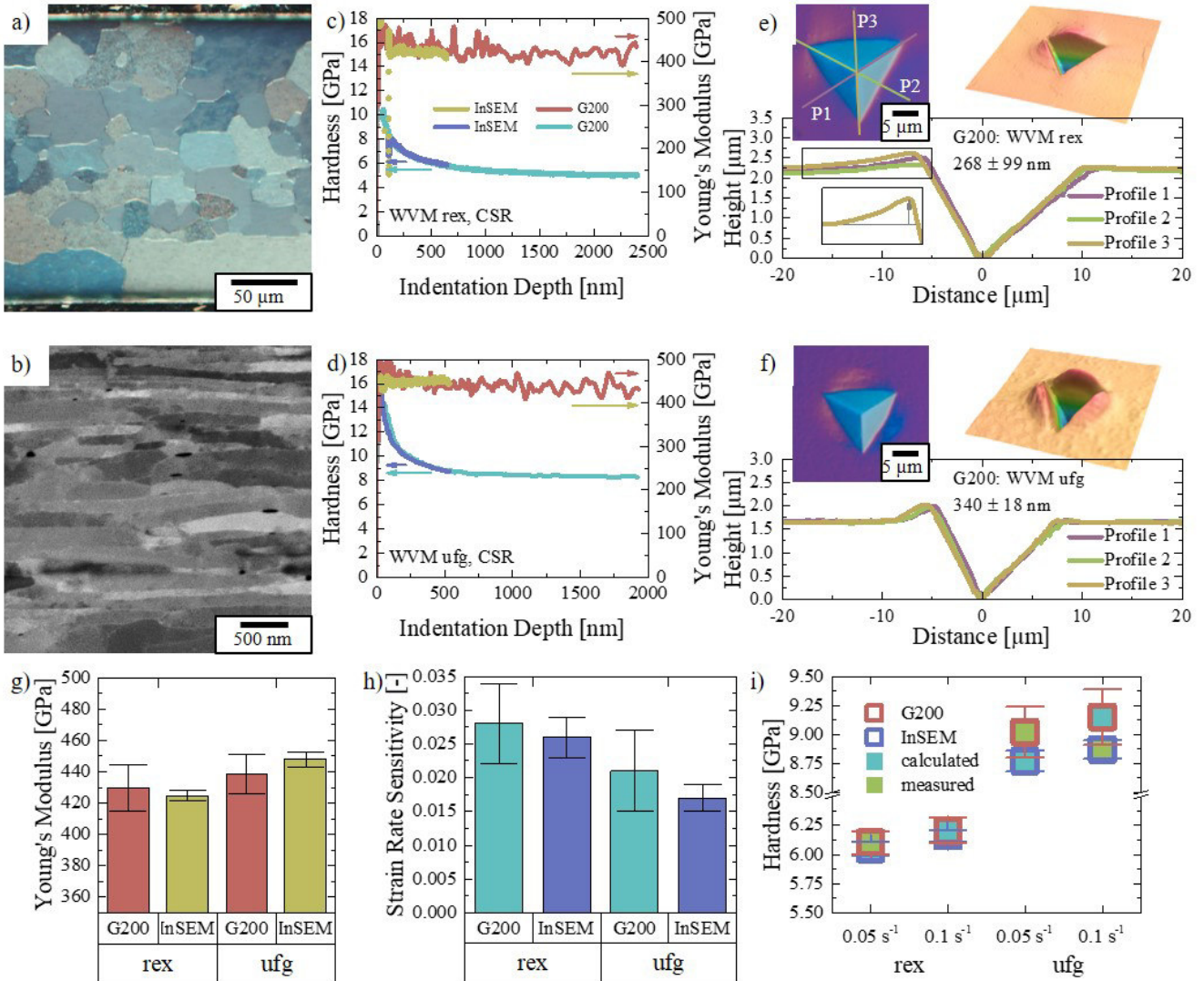


Figure 4.1: Graphical summary of the experiments performed on a K-doped W in two different microstructural conditions: a) LOM image of the rex sample b) SEM image of the as-received, ufg sample. c) and d) show the development of representative hardness and Young's modulus over indentation depth curves obtained with the InSEM and G200 nanoindenter platforms. e) and f) represent investigations regarding the pile-up behavior for indentations performed with the G200 system including LOM images and 3D profilometry obtained with a LSCM. In g)-i) the results of the nanoindentation experiments for Young's modulus, strain rate sensitivity and hardness are graphically summarized.

4.2 Identification of the Deformation-Bearing Phase in a Two-Phase Duplex Steel - Room Temperature Property Mapping

A high-alloy duplex steel (1.4501) with the main alloying elements having a nominal composition of 25 wt.% Cr, 3.6 wt.% Mo, 7 wt.% Ni, 0.25 wt.% N, 0.7 wt.% Cu and 0.7 wt.% W was used for this study in an annealed state. The microstructure consists of two different phases, ferrite and austenite, respectively [50]. A tensile test specimen, that was loaded to breakage, showed clear necking before fracture, indicating strong plastic deformation in this part of the specimen. Samples for RT nanoindentation were taken from the tensile specimen as schematically drawn in Fig. 4.2a. One directly from the region of necking, representing the deformed sample and one from the head, that was undeformed. An array of indentations with a spacing of 4 μm were carried out and post-test electron back-scatter diffraction (EBSD) was used to assign the indents to their certain phases (Figs. 4.2b and c). The experiments were performed at a strain rate of $\dot{P}/P = 0.1 \text{ s}^{-1}$ to a maximum indentation depth of 200 nm.

The measured Young's modulus showed significant variation in the range of 200 to 270 GPa over the whole sample (Fig. 4.2d). Generally, the elastic modulus of the ferritic phase was higher ($260 \pm 9 \text{ GPa}$) compared to the average values for austenite ($241 \pm 19 \text{ GPa}$). This is consistent with previously published data on highly alloyed duplex steels [51, 52]. The high Young's modulus compared to pure Fe, where values around 210 GPa are reported, could be caused by the high amount of alloying elements. Cr in particular is known for its increasing effect on the elastic stiffness [53]. A pronounced elastic anisotropy is evident when comparing the values for austenite grains orientated close to the $\{111\}$ and $\{101\}$ to those of other, random orientation. Consistent with our data, the $\langle 111 \rangle$ and $\langle 101 \rangle$ directions are known as the elastically stiffest in an austenitic crystal [54, 55]. No obvious elastic anisotropy could be observed in ferrite as grains with only three different orientations were measured in the randomly positioned indentation array. This is also represented by a lower scatter bar in Fig. 4.2f.

The observed hardness in the undeformed sample (Fig. 4.2e) demonstrates an obvious difference between the harder ferrite ($5.72 \pm 0.53 \text{ GPa}$) and the softer austenite ($4.78 \pm 0.14 \text{ GPa}$). A difference in phase dependent hardness was reported previously [36], caused by the lower yield stress of austenite compared to ferrite [56]. The $\{111\}$ orientated grain interestingly exhibits the lowest hardness, although it is usually reported as the strongest direction [57]. However, Chen *et al.* [58] recently observed strong hardness deviation of more than 20% for Berkovich nanoindentation on $\{111\}$ orientated austenite grains. This discrepancy could be related to sample rotation about the indenter axis *i.e.* the activated slip systems and thereby hardness strongly depend on the alignment of the three indenter contact surfaces with respect to the crystal orientation.

Upon comparing the derived mechanical properties between the undeformed and deformed samples, no significant change in the Young's modulus could be observed (Fig. 4.2f). This supports the validity of the results, as elasticity is unaffected by crystal defects caused by plastic deformation. In contrast, the hardness of the austenitic phase increases remarkably compared to the undeformed state, see Fig. 4.2g. Similar observations were reported by Liu *et al.* [59]. As the grain size of the investigated material was large compared to the probed sample volume of a single indent, grain boundaries do not affect the materials hardness. Instead, the increase in strength of austenite has to be related to an increased dislocation density caused by work-hardening upon deformation. While both, ferrite and austenite,

are in principle capable to work-harden significantly [60], the invariable hardness in the case of ferrite points towards an unchanged defect density through deformation. It can therefore be argued, that global plasticity in case of the tensile test is mainly carried by the austenite in this two-phase duplex steel, consistent with its lower yield strength.

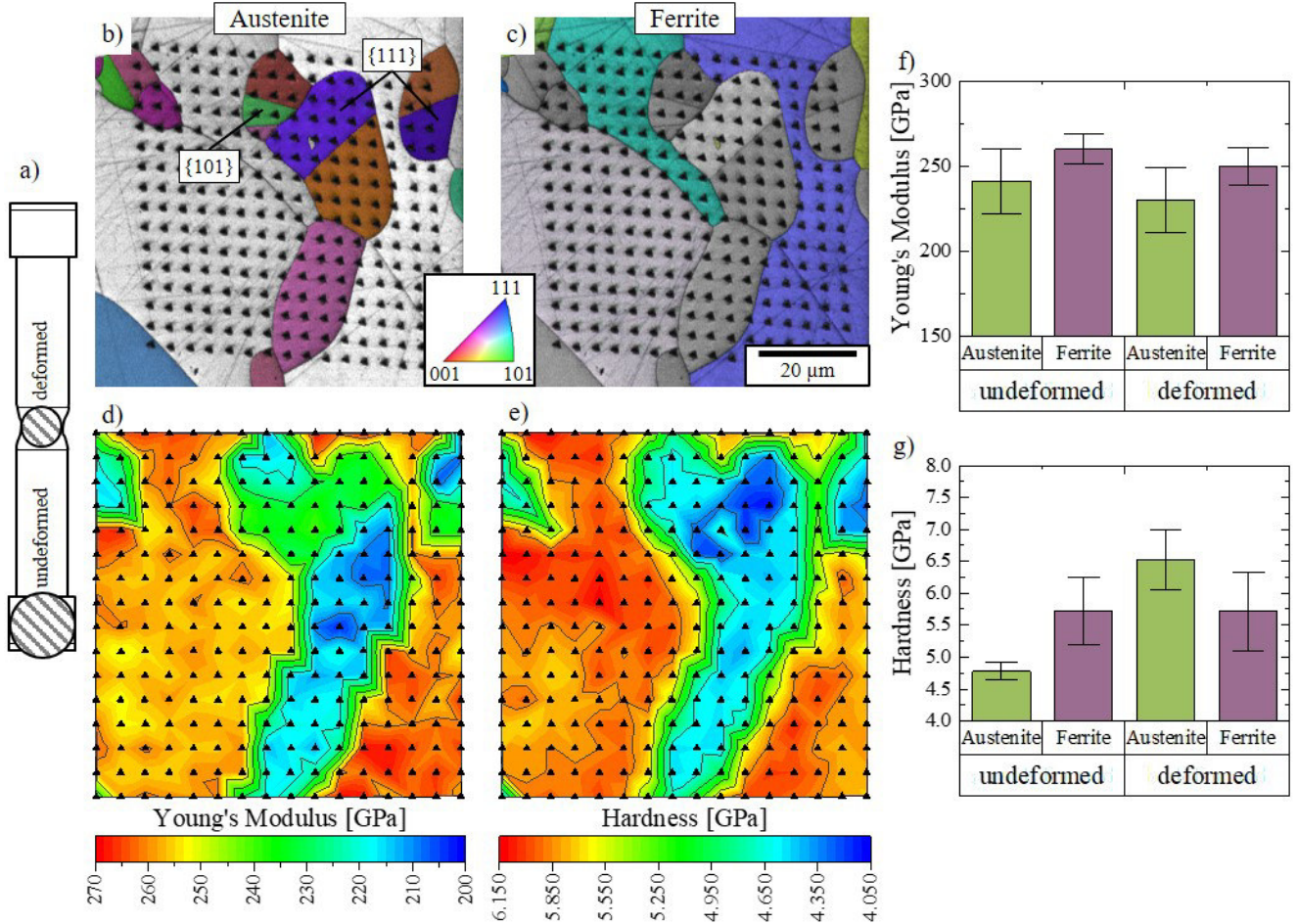


Figure 4.2: Graphical summary of the experiments performed on a duplex steel: a) Sampling from a tensile test specimen. EBSD-imaging of an array of indents on the undeformed sample showing color inverse pole figures combined with greyscale image quality maps for b) austenite and c) ferrite. Results of the nanoindentation mapping: d) Young's modulus and e) hardness. Effect of plastic deformation on the mechanical properties of the two phases: f) Young's modulus and g) hardness.

4.3 High Temperature Performance of Different Cu-Alloys

For this investigation two different, heavily deformed Cu-alloys, namely Cu₂Be, Cu₇Ag (composition in wt.%) and accumulative roll bonded Cu₂₀Nb (composition in vol.%) were tested up to 300 °C. The samples were received as 50 μm thick sheets whereby an adapted experimental setup had to be developed to probe these thin foils. Therefore, a Mo disc with a thickness of approximately 1 mm and 12 mm in diameter was used as a carrier for the samples. The polished Cu-foils were then mounted on the Mo-carrier with the high temperature ceramic glue OmegabondTM600 (Omega Engineering Inc., Deckenpfronn, Germany) as schematically illustrated in Fig. 4.3a. Due to a large variation in the thermal expansion coefficients of this experimental framework slow heating ramps (2.5 °C min⁻¹) were necessary to prevent the ceramic glue from loosening of the sample. Nonetheless, a constant Young's modulus over indentation depth (Fig. 4.3c) for the whole investigated temperature range supports the validity of the data and emphasizes the feasibility of the experimental setup.

Cu-Be and Cu-Ag exhibit their mechanical strength through precipitation hardening caused by a decreasing solubility of the alloying elements in the Cu matrix with decreasing temperature [61]. Through a solution heat treatment and subsequent annealing, nanometer sized precipitation are formed [62]. In Cu-Be metastable early stages of the ordered body-centered cubic γ -phase [63] cause an increase in hardness. Cu-Ag forms an eutectic solid solution, therefore precipitation hardening follows from coherent silver-rich segregation zones [64]. In contrast, Nb exhibits no noteworthy solubility for Cu. A Cu-Nb nanocompound was realized by accumulative roll bonding (ARB) [65, 66] in 12 cycles, resulting in theoretically more than 8000 (2^{12+1}) alternating layers of Cu and Nb within the thickness of the foil.

For the three different materials very similar values for the elastic modulus were obtained: 133.0 ± 1.2 , 129.3 ± 1.8 and 126.9 ± 1.8 GPa for Cu-2Be, Cu-7Ag and Cu-20Nb, respectively. This is well in the range for highly deformed Cu [67] and Cu-Nb composited [68]. A decreasing trend in the Young's modulus was evident with increasing temperature (Fig. 4.3b).

The measured RT hardness of the different samples, however, show clear differences. Cu₂Be exhibits a significantly higher hardness (6.6 ± 0.1 GPa) compared to Cu₇Ag and Cu₂₀Nb (4.4 ± 0.1 GPa and 4.5 ± 0.1 GPa, respectively). The difference between the two precipitation hardening alloys can be explained when considering the atomic proportion of the respective alloying element. Due to the difference in atomic mass, 2 wt.% Be equals to 12.6 at.%, whereas 7 wt.% Ag corresponds to 4.2 at.%. Combined with the fact that the precipitations in case of Cu-Be contain up to 50 % of Cu in its stable form [63], whereas in Cu-Ag they consist mainly of Ag [64], it can be argued that the amount of strength-increasing precipitations is higher in Cu₂Be. For the Cu-Nb compound the high strength arises from the high density of interfaces between the face-centered cubic (fcc) Cu and bcc Nb, following a Hall-Petch type of relationship [68] and resulting in similar RT mechanical strength as the Cu₇Ag alloy.

Observing the hardness over testing temperature (Fig. 4.3b), the Cu₇Ag alloy exhibits the weakest high temperature performance in terms of hardness decrease (45 % compared to the RT value). The hardness of Cu₂Be decreases by 18 % (1.2 GPa) and Cu₂₀Nb by 24 % (1.1 GPa), however, the different starting levels need to be considered. Although the decrease in hardness is significantly higher than the reduction in Young's modulus (-15 %, -21 % and -8 % for Cu₂Be, Cu₇Ag and Cu₂₀Nb, respectively), it is not necessarily a sign of microstructural instabilities. Cu-Ag alloys usually exhibit significant precipitation coarsening and grain growth at testing temperatures exceeding 400 °C, resulting in a drop in flow stress

[69], while for Cu-Nb nanocompounds a maximum operational temperature of 400 °C was suggested [70].

In this study an alternative sample mounting setup for thin metallic foils was presented, enabling the extraction of valid mechanical properties with high temperature nanoindentation. From the observed findings it can be concluded that the mechanical performance of the Cu2Be alloy is superior in terms of strength or hardness. Cu7Ag and Cu20Nb exhibit similar properties at RT, however the high temperature characteristics of Cu20Nb was better than Cu7Ag.

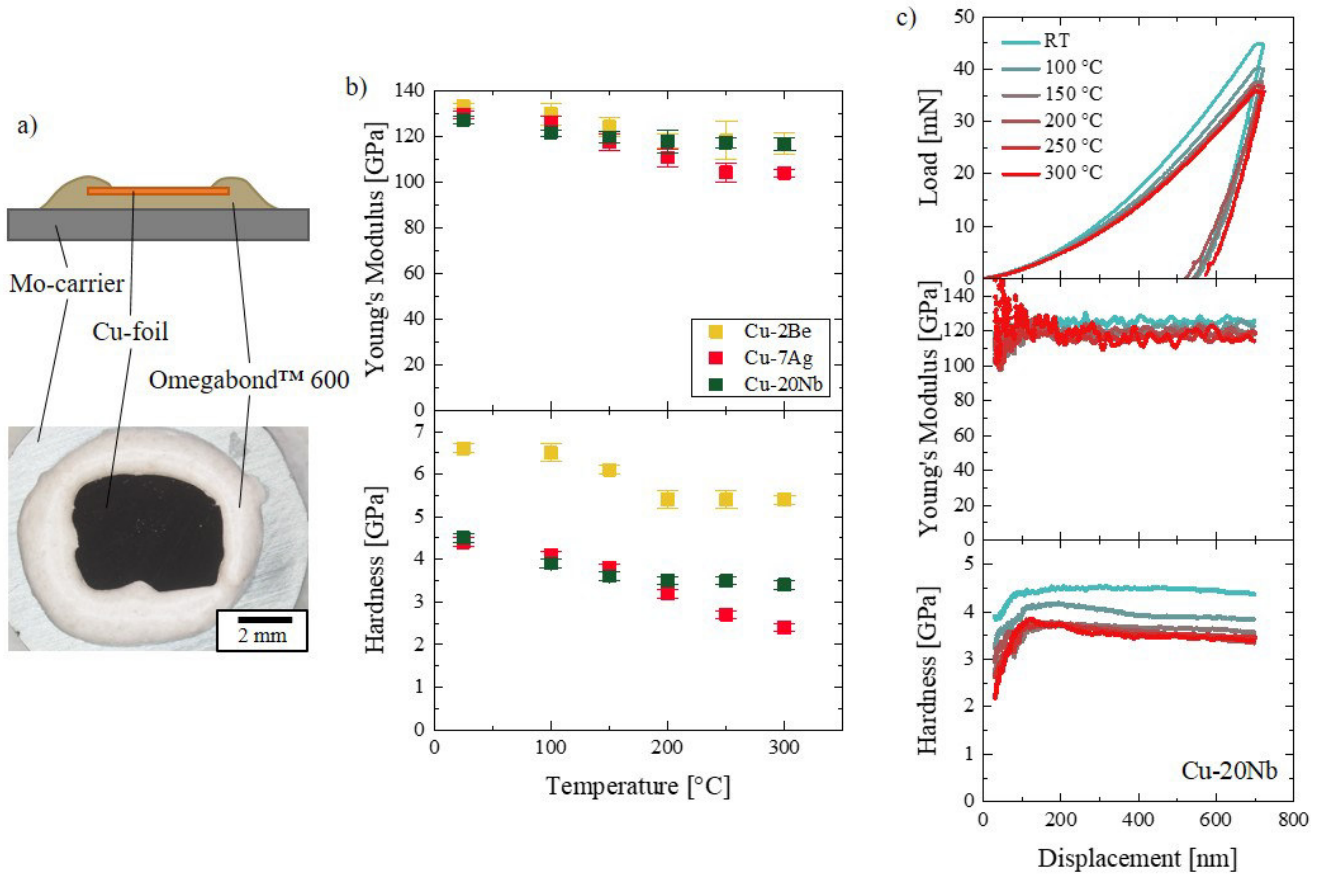


Figure 4.3: Graphical summary of the experiments performed on different Cu sheets: a) Sample mounting of a 50 μm Cu foil. b) Young's modulus and hardness over temperature for three different Cu alloys. c) Representative load, Young's modulus and hardness curves over displacement for a Cu-20Nb alloy.

5 Summary of Publications

The following chapter explains the main findings and results of the PhD thesis by summarizing the listed publications. The workflow of this thesis, as presented in Fig. 5.1 can be separated into two analysis paths. The fundamentals of plasticity in bcc metals and alloys with confined microstructure was systematically investigated. Started with depicting the influence of alloying elements on the friction stress controlled plasticity in conventionally coarse grained tungsten (**Publication A**), the interplay of grain boundaries with solute atoms and the thermal stability of ultra-fine grained microstructures was highlighted (**Publication B**). Finally, samples designed with well defined interface types were investigated to clarify the role of different types of grain boundaries on dislocation controlled plasticity in bcc metals with confined grain size (**Publication C**). Further, a proof of concept was carried out to demonstrate the feasibility of micromechanical materials characterization methods upon bulk phase transformation, with cobalt as a model material (**Publication D**).

Altogether, the versatility and applicability of HT nanoindentation techniques were demonstrated to identify the dominating deformation mechanisms, making it an ideal tool for material research and development.

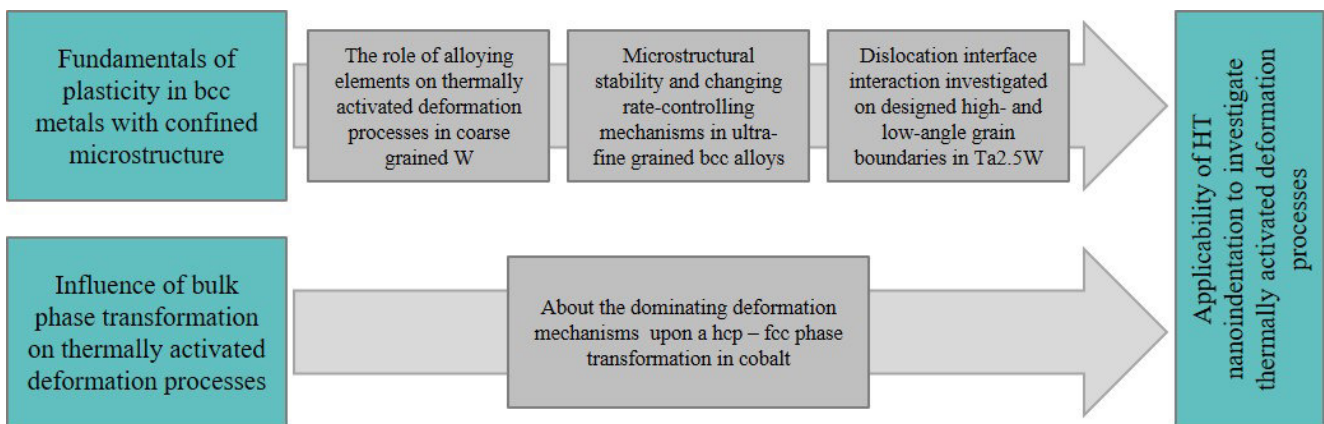


Figure 5.1: Workflow of this PhD thesis.

5.1 Publication List

Publication A

Thermally activated deformation mechanisms and solid solution softening in W-Re alloys investigated by high temperature nanoindentation: J. Kappacher, A. Leitner, D. Kiener, H. Clemens, V. Maier-Kiener. *Materials and Design* 189 (2020) 108499.

Publication B

Controlling the high temperature deformation behavior and thermal stability of ultra-fine grained W by Re alloying: J. Kappacher, O. Renk, D. Kiener, H. Clemens, V. Maier-Kiener. *Journal of Materials Research* (2021).

Publication C

How grain boundary characteristics influence plasticity close to and above the critical temperature of ultra-fine grained bcc Ta_{2.5}W: J. Kappacher, O. Renk, D. Kiener, H. Clemens, V. Maier-Kiener. Submitted to an SCI-journal.

Publication D

High temperature nanoindentation as a tool to investigate plasticity upon phase transformations demonstrated on Cobalt: J. Kappacher, M. Tkadletz, H. Clemens, V. Maier-Kiener. Submitted to an SCI-journal.

Remarks:

In the appended publications, all co-authors actively contributed to the preparation of the published manuscript in fruitful discussions. Supervision and experimental impetus came mainly from V. Maier-Kiener. The experiments, data analysis and composition of the publications were performed by myself, with the following exceptions:

- Publication A** V. Maier-Kiener essentially assisted the implementation of strain rate jump tests, supported the experiments and shared her expertise in elevated temperature nanoindentation techniques.
- Publication B** Sample fabrication was utilized by M. Wurmshuber. Microstructural characterization via EBSD was supported by O. Renk.
- Publication C** Sample design and fabrication was developed together with O. Renk, who further performed the microstructural characterization.
- Publication D** Experimental setup and conception was evolved together with V. Maier-Kiener. M. Tkadletz supported the high temperature X-rays diffraction experiments and S. Jakob performed the EBSD investigations.

Further Publications:

Combination of nanoindentation and microscopy for the examination of aluminum alloys in coarse- and ultra fine-grained condition:

J. Kappacher, A. Leitner, H. Clemens, V. Maier-Kiener. *Praktische Metallographie* 56, 7 (2019) 432-442.

Beryllium - A challenge for preparation and mechanical characterization:

M. Siller, J. Kappacher, R. Rolli, H. Clemens, V. Maier-Kiener. *Praktische Metallographie* 56, 10 (2019) 624-633.

Disordered interfaces enable high temperature thermal stability and strength in a nanocrystalline aluminum alloy:

G.H. Balbus, J. Kappacher, D.J. Sprouster, F. Wang, J. Shin, Y.M. Eggeler, T.J. Rupert, J.R. Trelewicz, D. Kiener, V. Maier-Kiener, D.S. Gianola. Submitted to an SCI-Journal.

5.2 Conference Contributions

Kombination von Nanoindentation und Mikroskopie zur Untersuchung von Aluminium-Legierungen im grob- und ultrafeinkörnigen Zustand.

Oral presentation, 15. Internationale Metallographie Tagung, 19.09.2018, Leoben, Austria.

Investigating mechanical properties of W-Re alloys - A high temperature nanoindentation study.

Oral presentation, TMS2019 - 148th Annual Meeting and Exhibition, 11.03.2019, San Antonio, TX.

Investigations of thermally activated deformation process in W-Re alloys by high temperature nanoindentation up to 800 °C .

Oral presentation, 65. Metallkunde-Kolloquium, 24.04.2019, Lech am Arlberg, Austria.

Challenges and first results of ultra-high temperature nanoindentation on W-Re binary alloys.

Oral presentation, KLA Nanomechanical Testers User Workshop, 02.05.2019, Langen, Germany.

Thermally activated deformation mechanisms - High temperature nanoindentation on W-Re alloys.

Poster presentation, Best Poster Award - First Place, ECI Nanomechanical Testing in Materials Research and Development, 02.10.2019, Torremolinos, Spain.

Plastic deformation behavior of cobalt upon phase transformation revealed by high temperature nanoindentation.

Oral presentation, KLA e-Usermeeting, 09.06.2020, online.

How phase transformation changes the plastic deformation behavior of cobalt - a high temperature nanoindentation study.

Oral presentation, DGM Arbeitskreistreffen Rasterkraftmikroskopie und nanomechanische Methoden, 09.07.2020, online.

5.3 Supervised Theses

F. Römer (2021) Mikrostructureller Einfluss auf die Nanoindentierung von Molybdän-Rhenium Legierungen. Bachelor thesis, Montanuniversität Leoben.

L. Lumper (2021) Mechanical constitution of stable and metastable phases in Cu₂₀Sn. Master thesis, Montanuniversität Leoben.

5.4 Fundamentals of Plasticity in bcc Metals with Confined Microstructure

Dislocation plasticity in bcc metals at low homologous temperatures (usually below $0.2 T_m$) is commonly known to be controlled by a high lattice friction [71]. The flow stress is composed of a thermal as well as an athermal contribution [72, 73]. While the latter one stems from long-range obstacles, such as grain boundaries or statistically stored dislocations, the thermal contribution originates from a non-planar core structure of the $1/2\langle 111 \rangle$ screw dislocations, limiting their mobility compared to edge dislocations. Hence, the rate limiting mechanism for deformation is the movement of screw dislocations through kink-pair formation to overcome the Peierls potential [74, 75]. This further results in a pronounced strain rate sensitivity. As temperatures increase, the Peierls barrier becomes thermally activated, whereby the observed flow stress is strongly temperature dependent and the strain rate sensitivity diminished up to $0.2 T_m$. Kink-pair formation and its consequence for mechanical properties is well described in theoretical [76, 77] as well as experimental works [71, 73, 78]. The phenomenon was also directly observed in transmission electron microscopy [79, 80].

Alloying of the bcc metal W with Re results in the well known solid solution softening effect [81–84]. This intrinsic response originates from filling of the d bands, modifying the intermetallic bonding [85]. As a consequence, the core of the $1/2\langle 111 \rangle$ screw dislocations changes from a symmetric to an asymmetric arrangement [86], leading to a reduction in the Peierls stress [87].

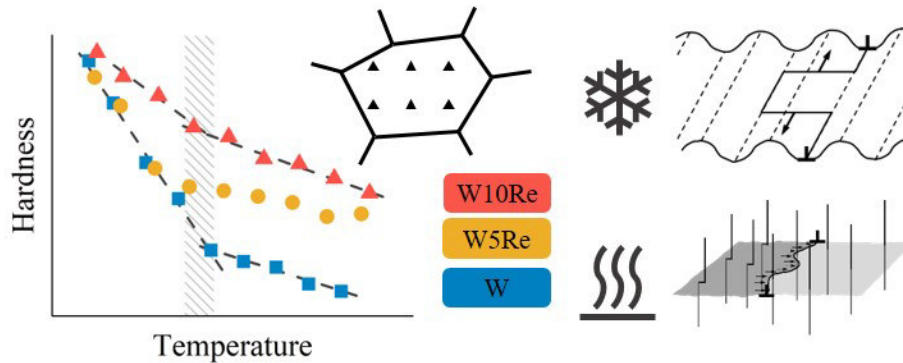
In **Publication A** the influence of the alloying element Re in W on the plastic deformation behavior was investigated from RT to 800°C on W, W5Re and W10Re (in wt.%) with HT nanoindentation methods. Thereby a large range of homologous temperature is covered, allowing for a careful observation of both, the thermal and athermal deformation regime. As the grain size of the investigated samples was large compared to the probed volume during nanoindentation, the results display the intrinsic effect of the alloying element Re on W, with minor contribution from grain boundaries or other interfaces.

Johann Kappacher, Alexander Leitner, Daniel Kiener, Helmut Clemens, Verena Maier-Kiener
Thermally activated deformation mechanisms and solid solution softening in
W-Re alloys investigated via high temperature nanoindentation
Materials and Design 189 (2020) 108499.

From the measured hardness over temperature, a clear distinction between two different deformation regimes was observed. Below $0.2 T_m$ the materials strength was found strongly temperature dependent, with a high strain rate sensitivity in the order of 0.02 to 0.04 and an activation volume around $10b^3$ for pure W. All these characteristics pointed towards a kink-pair mechanisms as the rate-controlling step in plastic deformation, which was also confirmed by the derived activation energy for plastic deformation. In contrast, at higher temperatures, hardness was found to be less temperature sensitive, the strain rate sensitivity diminished and the activation volume developed to the order of a few hundred b^3 . The mechanical behavior is thus governed by dislocation-dislocation interaction.

The atomistic effect of Re on the mechanical properties could be well outlined. In the high temperature deformation regime the athermal hardness was increased through solid solution hardening. A reduction in the Peierls barrier led to a reduced temperature and strain rate sensitivity below $0.2 T_m$, while the activation volume was increased. Further, in the low temperature regime the activation energy for plastic deformation was reduced through alloying with Re, consistent with a reduced Peierls potential, while at high temperatures no influence was observed.

In summary it could be shown that HT nanoindentation is well suited to assess the rate controlling deformation mechanisms and the role of alloying elements on the plastic behavior of a material of interest.



Grain refinement through severe plastic deformation techniques enables the synthesis of ufg materials [88–91] with outstanding properties in terms of strength and damage tolerance. As the grain size is refined to submicron or nanoscaled dimensions, the rate controlling deformation mechanism changes, though is still controlled by dislocation motion. For example in fcc metals deformation is no longer controlled by dislocation-dislocation interaction, rather, annihilation processes of dislocations at grain boundaries become more important [92]. This results in an increased strain rate sensitivity and an activation volume in the range of a few $10b^3$ [93–96]. The rate dependence of flow stress is rather independent of temperature up to $0.2 T_m$, but increases as temperature exceeds this critical value [97–100]. Recently, Renk *et al.* [22] confirmed for a variety of ufg fcc metals that the origin of this behavior is the thermally activated accommodation of lattice dislocations within the grain boundaries.

Contrarily, for bcc metals an ultra-fine grained microstructure results in a decreased strain rate sensitivity [96, 101]. This is commonly associated with a major strength contribution from the increased amount of grain boundaries, providing rather athermal, long range obstacles for dislocation motion, while only limited strength-contribution arises from the local Peierls barrier [75, 102].

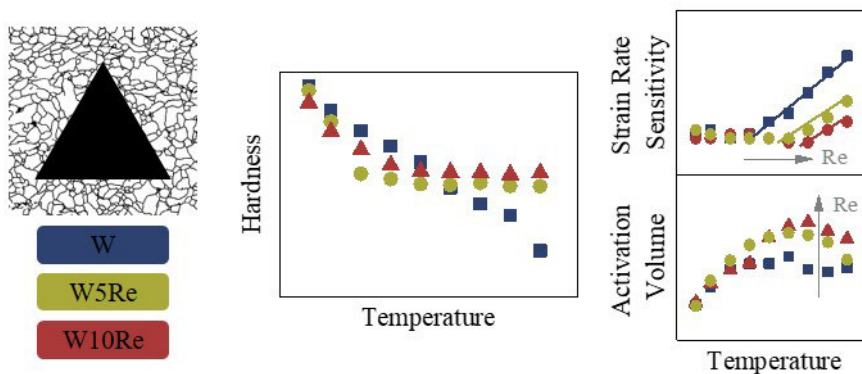
In **Publication B** the sample material from the previous study was deformed via high pressure torsion (HPT). The resultant microstructure was well comparable between the different samples with a grain size around 250 to 300 nm. Static annealing experiments over a broad temperature range were performed to outline the thermal stability of the investigated, highly metastable microstructure of the severely deformed materials. HT nanoindentation was conducted to identify the rate controlling deformation mechanisms and the influence of alloying elements, as a systematic investigation of the latter is absent in current literature for ufg bcc metals.

Johann Kappacher, Oliver Renk, Daniel Kiener, Helmut Clemens, Verena Maier-Kiener
Controlling the high temperature deformation behavior and thermal stability
of ultra-fine grained W by Re alloying
Journal of Materials Research (2021).

Temperature dependent hardness as well as static annealing experiments emphasized the beneficial role of the alloying element Re on the thermal stability of the ufg microstructure. While in pure W grain growth was already observed from 600 °C, the pinning effect of Re atoms on the grain boundaries assures thermal stability up to 900 °C for the alloyed variants. As a result, ufg W showed a steady decrease of hardness over temperature.

Similar to the results in **Publication A** two pronounced deformation regimes could be observed in case of the ufg W-Re alloys. Up to 0.15 - 0.20 T_m hardness is strongly temperature dependent, followed by an athermal plateau. Also the activation volume and activation energy at low homologous temperatures would indicate kink-pair formation as the dominating mechanism. However, a clear effect of Re on the Peierls barrier in the ufg W-Re alloys, that was well captured with the same experimental setup in case of the coarse grained condition was absent. This includes a reduced temperature and strain rate sensitivity, and increased activation volume as well as a reduced activation energy for plastic deformation below 0.20 T_m . Thus, it was suggested, that local chemical effects for dislocations interacting with grain boundaries below 0.2 T_m could be more dominant than previously recognized.

Derived from the observed activation volumes and energies it was evident, that dislocation-grain boundary processes become the rate controlling mechanisms above 0.20 T_m . Comparable to ufg fcc metals the predominant processes are dynamic recovery processes at grain boundaries. The enhanced strain rate sensitivity could be explained by the kinetics of these processes, that are determined by the boundary diffusivity and hence proceed facilitated above a certain temperature. The shift of the temperature, where the strain rate sensitivity increases, through alloying with Re towards higher values is consistent with intergranular stress relaxation, scaling with the inverse of the grain boundary diffusion coefficient.



As demonstrated in **Publication B**, alloying can have a remarkable influence on the dislocation-grain boundary interaction of bcc metals in the high-temperature deformation regime, where the plastic behavior is comparable with ufg fcc metals [103]. This is caused by the strong influence of grain boundary diffusivity on the dynamic recovery processes at grain boundaries [104, 105]. Decoration of grain boundaries with alloying atoms is however not the only way to influence the interface diffusivity. Renk *et al.* recently demonstrated, how the misorientation angle of adjacent grains influences the temperature- and strain rate dependence of nanostructured Ni by probing samples consisting of a majority of high- and low angle grain boundaries, as well as twin boundaries [106]. As bcc refractory metals are commonly used as high temperature structural material, it is of urgent importance to understand the plastic behavior of high-performance bcc metals in this temperature regime.

To contribute to a better understanding of the role of different grain boundary types in ufg bcc metals, in **Publication C** three different Ta2.5W samples were probed. One in the recrystallized state to depict single crystalline behavior and a conventionally HPT deformed sample with a grain boundary characteristic consisting mainly of HAGB. Further, cyclic HPT deformation was conducted to receive an ufg sample mainly containing LAGBs. The resultant grain or cell size was well below 300 nm. Ta2.5W was chosen for several reasons: its high melting point combined with a low critical temperature, where kink-pairs are fully thermally activated, provide a large experimental temperature field, where an fcc-like deformation behavior is evident before thermally induced grain coarsening occurs. Ta is further known for its relatively easy deformability with HPT and the addition of W should provide additional thermal stability of the ufg microstructure.

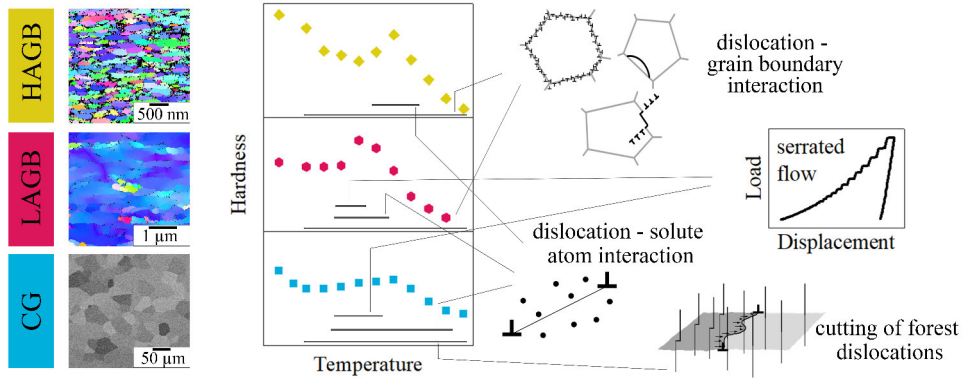
Johann Kappacher, Oliver Renk, Daniel Kiener, Helmut Clemens, Verena Maier-Kiener
How grain boundary characteristics influence plasticity close to and above
the critical temperature of ultra-fine grained bcc Ta2.5W
Submitted to an SCI journal.

In the recrystallized state, the thermal activation of the kink-pair formation could be well captured at 100 °C, derived from a temperature-invariant hardness and low strain rate sensitivity at higher temperatures. Above this temperature a strong temperature dependence of the hardness was observed for samples consisting mainly of HAGBs, while the LAGB sample behaved rather athermal. Also the strain rate sensitivity was found to increase more strongly above 300 °C (around $0.2 T_m$) for the sample with HAGBs. The difference in temperature- and rate dependence of the flow stress was related to the influence of the different grain boundary character to the dominating deformation mechanism. The higher grain boundary diffusivity in case of the less dense packed HAGBs results in a reduced relaxation time for dislocations at these interfaces, underlining the importance of the grain boundary character for accommodation of lattice dislocations within these interfaces.

Furthermore, the interaction of dislocations with dissolved oxygen atoms was discussed. Already 20 ppm of this impurity species significantly influences plasticity between 200 and 500 °C for the cg microstructure. The effect manifests as an increased hardness, even leading to a Portevin-Le Chatelier

effect with serrated flow characteristics and a negative strain rate sensitivity between 200 and 300 °C.

The different interfaces of the ufg material variants were found to have a significant influence on the dislocation-impurity interaction. Different temperature regimes, where the flow stress was affected account for the diffusion relation of this processes, even suppressing the discrete yielding in case of the HAGBs.



5.5 Influence of Bulk Phase Transformation on Thermally Activated Deformation Processes

HT nanoindentation is well suited to evaluate microstructural instabilities of highly metastable, ufg metals as previously reported and also demonstrated in **Publication B**. Earlier studies outlined the feasibility of this technique to investigate the flow stress towards glass transition temperatures of amorphous materials, *e.g.* in Zr-based bulk metallic glasses [107] or amorphous selenium [108]. Phase transitions on the other hand, where the atomic structure of a crystal changes was mainly investigated and observed stress-driven, for example in silicon [109, 110], germanium [111] or NiTi shape memory alloy [112].

To the best of the author's knowledge, no studies are available, that investigate allotropic transformation with HT nanomechanical methods and relate the thermally driven phase transition with the occurring plastic deformation mechanisms. A case study about the feasibility of this approach was conducted in **Publication D** with metallic cobalt as a model material. Upon heating cobalt experiences a phase transformation from a low temperature hexagonal close packed (hcp) to a high temperature fcc phase around 430 °C, which was analyzed by means of differential scanning calorimetry (DSC) and high temperature X-Ray diffraction (XRD).

Johann Kappacher, Michael Tkadletz, Helmut Clemens, Verena Maier-Kiener

High temperature nanoindentation as a tool to investigate plasticity upon
phase transformations demonstrated on Cobalt

Submitted to an SCI journal.

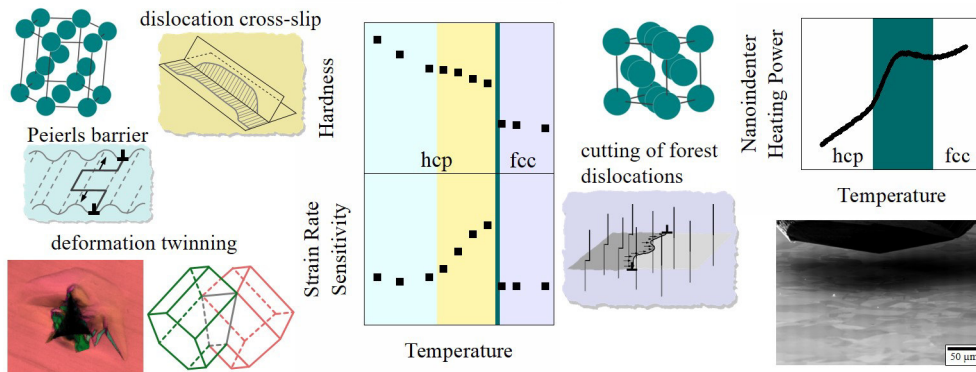
Accompanied with a change in crystal structure the flow stress was found to decrease remarkable, which could be related to available slip systems and ease of dislocation glide in the fcc compared to the hcp crystal structure. Elasticity on the other hand was largely unaffected. From a thermal activation analysis three different deformation regimes could be distinguished between RT and 600 °C.

Displacement bursts while testing the hcp phase were found to indicate deformation twinning, owed to the low stacking fault energy of cobalt, and were identified by EBSD measurements on remaining indents. An approach was made to quantify the twinning activity and the results were shown to coincide with the identified deformation mechanisms:

Between RT and 200 °C plasticity was found to be lattice friction controlled. Dislocations on the basal plane have to overcome a Peierls barrier, which was derived from the results of strain rate sensitivity, activation volume and activation energy. With increasing temperature dislocation cross slip proceed facilitated through thermal activation of dislocation cross slip, indicated by a reduced twinning activity, an increasing strain rate sensitivity, a temperature independent activation volume and a decreasing activation energy for plastic deformation.

As the crystal structure changes to fcc, at 450 °C dislocation glide promotes obstacle controlled *i.e.* through cutting of forest dislocations. This mechanism is typically observed and well described for a variety of coarse grained fcc metals. The measured strain rate sensitivity diminishes, activation volumes

are in the order of a few hundred b^3 and the activation energy for plastic deformation is in the range of 3.5 to 4.0 eV.



6 Concluding Remarks and Outlook

Given the opportunity to elaborately work on nanoindentation setups and especially with a high temperature system creates awareness of the versatility of this mechanical microprobe tool. However, the potential errors and limitations in such highly complex systems must be taken into consideration by the careful user for deriving the multitude of materials parameters. For a critical comparison with complimentary methods of investigation and data interpretation, both, the experimental setup as well as the sample of interest have to be well understood.

The conclusions drawn from the investigations conducted in the present study can be summarized as follows:

- Precise knowledge about thermal gradients and temperature management is required even for commercially available high temperature nanoindentation systems in order to extract reliable results of materials properties. This was outlined from the established tip temperature calibration procedures and temperature matching methods.
- Choice of an adequate indenter material and its commercial availability will be the main restriction for future high temperature nanomechanical setups.
- Materials with limited accessibility in terms of sample volume can be extensively investigated with nanoindentation techniques. *E.g.* for samples produced on a laboratory bench-scale, thin films or high priced elements, as demonstrated on a variety of HPT deformed samples, an Al-Ni-Ce thin film on silicon substrate or different Cu foils.
- One of the strengths of nanoindentation used as a mechanical microprobe is displayed when properties of multi-phase materials are laterally resolved and macroscopic materials behavior is derived as shown on a duplex steel tensile test specimen.
- Thermal activation analysis from temperature and strain rate dependent hardness values obtained by high temperature nanoindentation is a potent tool for materials science to resolve rate limiting deformation processes. The methodology was introduced and refined throughout the whole thesis.
- Careful consideration of the probed sample volume with respect to the samples microstructure allows for comparison of mechanical properties obtained at the nanoscale to macroscopic experiments. This could be well demonstrated in coarse grained W and W-Re alloys where adequate literature was available.
- Nanoindentation combined with high resolution microscopy gives a powerful opportunity to investigate stress-induced material response and helps to clarify certain features observed in nanoindentation data. As an example this was emphasized through EBSD for identifying deformation twinning in hcp cobalt.
- High temperature nanoindentation combined with complimentary thermal analysis methods, *e.g.* DSC or HT-XRD, can effectively be used to correlate phase transformation with resulting changed mechanical properties as demonstrated on metallic cobalt.

The present thesis outlines the applicability of high temperature nanoindentation as a versatile tool to derive thermally activated deformation processes. Further studies could extend the usability of the established high temperature experimental setup by implementing methods with non-self-similar tip geometries to extract flow curves on the local scale or develop *in-situ* experiments in the scanning electron microscope with micron-sized sample geometries, *e.g.* pillar compression or cantilever bending.

References

- [1] W. C. Oliver, G. M. Pharr, An improved technique for determining hardness and elastic modulus using load and displacement sensing indentation experiments, *J. Mater. Res.* 7 (6) (1992) 1564–1583.
- [2] J. Pethica, R. Hutchings, W. C. Oliver, Hardness measurement at penetration depths as small as 20 nm, *Phil. Mag. A* 48 (4) (1983) 593–606.
- [3] V. Ashworth, W. Grant, R. Proctor (Eds.), *Ion implantation into metals*, 1982.
- [4] A. Fischer-Cripps, *Nanoindentation*, Springer New York, 2002.
- [5] I. ISO, 14577-1 metallic materials-instrumented indentation test for hardness and materials parameters-part 1: Test method. 2015, ISO: Geneva.
- [6] W. C. Oliver, J. B. Pethica, Method for continuous determination of the elastic stiffness of contact between two bodies, *uS Patent* 4,848,141 (Jul. 18 1989).
- [7] J. Pethica, W. Oliver, Tip surface interactions in STM and AFM, *Phys. Scripta* 1987 (T19A) (1987) 61.
- [8] J. Alkorta, J. M. Martínez-Esnaola, J. G. Sevillano, Critical examination of strain-rate sensitivity measurement by nanoindentation methods: Application to severely deformed niobium, *Acta Mater.* 56 (4) (2008) 884–893.
- [9] V. Maier, K. Durst, J. Mueller, B. Backes, H. W. Höppel, M. Göken, Nanoindentation strain-rate jump tests for determining the local strain-rate sensitivity in nanocrystalline Ni and ultrafine-grained Al, *J. Mater. Res.* 26 (11) (2011) 1421–1430.
- [10] B. Lucas, W. Oliver, Indentation power-law creep of high-purity indium, *Metall. Mater. Trans. A* 30 (3) (1999) 601–610.
- [11] V. Maier, B. Merle, M. Göken, K. Durst, An improved long-term nanoindentation creep testing approach for studying the local deformation processes in nanocrystalline metals at room and elevated temperatures, *J. Mater. Res.* 28 (9) (2013) 1177.
- [12] M. Cordill, M. Lund, J. Parker, C. Leighton, A. Nair, D. Farkas, N. Moody, W. Gerberich, The nano-jackhammer effect in probing near-surface mechanical properties, *Int. J. Plasticity* 25 (11) (2009) 2045–2058.
- [13] K. Siu, A. Ngan, The continuous stiffness measurement technique in nanoindentation intrinsically modifies the strength of the sample, *Phil. Mag.* 93 (5) (2013) 449–467.
- [14] G. M. Pharr, J. H. Strader, W. Oliver, Critical issues in making small-depth mechanical property measurements by nanoindentation with continuous stiffness measurement, *J. Mater. Res.* 24 (3) (2009) 653–666.

- [15] B. Merle, V. Maier-Kiener, G. M. Pharr, Influence of modulus-to-hardness ratio and harmonic parameters on continuous stiffness measurement during nanoindentation, *Acta Mater.* 134 (2017) 167–176.
- [16] A. Atkins, D. Tabor, Plastic indentation in metals with cones, *J. Mech. Phys. Solids* 13 (3) (1965) 149–164.
- [17] A. Leitner, V. Maier-Kiener, D. Kiener, Extraction of flow behavior and Hall–Petch parameters using a nanoindentation multiple sharp tip approach, *Adv. Eng. Mater.* 19 (4) (2017) 1600669.
- [18] K. Durst, V. Maier, Dynamic nanoindentation testing for studying thermally activated processes from single to nanocrystalline metals, *Curr. Op. Solid St. M.* 19 (6) (2015) 340–353.
- [19] A. Leitner, V. Maier-Kiener, D. Kiener, Dynamic nanoindentation testing: is there an influence on a material’s hardness?, *Mater. Res. Lett.* 5 (7) (2017) 486–493.
- [20] D. Tabor, *The hardness of metals*, Oxford university press, 1951.
- [21] J. Wheeler, V. Maier, K. Durst, M. Göken, J. Michler, Activation parameters for deformation of ultrafine-grained aluminium as determined by indentation strain rate jumps at elevated temperature, *Mater. Sci. Eng. A* 585 (2013) 108–113.
- [22] O. Renk, V. Maier-Kiener, I. Issa, J. Li, D. Kiener, R. Pippan, Anneal hardening and elevated temperature strain rate sensitivity of nanostructured metals: their relation to intergranular dislocation accommodation, *Acta Mater.* 165 (2019) 409–419.
- [23] D.-H. Lee, I.-C. Choi, G. Yang, Z. Lu, M. Kawasaki, U. Ramamurty, R. Schwaiger, J.-i. Jang, Activation energy for plastic flow in nanocrystalline CoCrFeMnNi high-entropy alloy: A high temperature nanoindentation study, *Scripta Mater.* 156 (2018) 129–133.
- [24] O. Sherby, P. Armstrong, Prediction of activation energies for creep and self-diffusion from hot hardness data, *Metall. Mater. Trans. B* 2 (12) (1971) 3479–3484.
- [25] J. Wheeler, J. Michler, Elevated temperature, nano-mechanical testing in situ in the scanning electron microscope, *Rev. Sci. Instrum.* 84 (4) (2013) 045103.
- [26] J. Wheeler, J. Michler, Invited article: Indenter materials for high temperature nanoindentation, *Rev. Sci. Instrum.* 84 (10) (2013) 101301.
- [27] J. S.-L. Gibson, S. Schröders, C. Zehnder, S. Korte-Kerzel, On extracting mechanical properties from nanoindentation at temperatures up to 1000C, *Extreme Mech. Lett.* 17 (2017) 43–49.
- [28] J. Wheeler, D. Armstrong, W. Heinz, R. Schwaiger, High temperature nanoindentation: The state of the art and future challenges, *Curr. Op. Solid St. M.* 19 (6) (2015) 354–366.
- [29] J. Wheeler, P. Brodard, J. Michler, Elevated temperature, in situ indentation with calibrated contact temperatures, *Phil. Mag.* 92 (25-27) (2012) 3128–3141.

- [30] N. Everitt, M. Davies, J. Smith, High temperature nanoindentation—the importance of isothermal contact, *Phil. Mag.* 91 (7-9) (2011) 1221–1244.
- [31] S. Korte, W. Clegg, Micropillar compression of ceramics at elevated temperatures, *Scripta Mater.* 60 (9) (2009) 807–810.
- [32] S. Korte, R. J. Stearn, J. M. Wheeler, W. J. Clegg, High temperature microcompression and nanoindentation in vacuum, *J. Mater. Res.* 27 (1) (2012) 167.
- [33] Y. Li, X. Fang, S. Lu, Q. Yu, G. Hou, X. Feng, Effects of creep and oxidation on reduced modulus in high-temperature nanoindentation, *Mater. Sci. Eng. A* 678 (2016) 65–71.
- [34] U. Hangen, C.-L. Chen, A. Richter, Mechanical characterization of PM2000 oxide-dispersion-strengthened alloy by high temperature nanoindentation, *Adv. Eng. Mater.* 17 (11) (2015) 1683–1690.
- [35] C. Minnert, W. C. Oliver, K. Durst, New ultra-high temperature nanoindentation system for operating at up to 1100C, *Mater. Des.* (2020) 108727.
- [36] Y. Zhang, D. P. Mohanty, P. Seiler, T. Siegmund, J. J. Kruzic, V. Tomar, High temperature indentation based property measurements of IN-617, *Int. J. Plast.* 96 (2017) 264–281.
- [37] J. S.-L. Gibson, S. G. Roberts, D. E. Armstrong, High temperature indentation of helium-implanted tungsten, *Mater. Sci. Eng. A* 625 (2015) 380–384.
- [38] A. J. Harris, B. D. Beake, D. E. Armstrong, M. I. Davies, Development of high temperature nanoindentation methodology and its application in the nanoindentation of polycrystalline tungsten in vacuum to 950C, *Exp. Mech.* 57 (7) (2017) 1115–1126.
- [39] F. P. Bowden, D. Tabor, *The friction and lubrication of solids*, Vol. 1, Clarendon Press, 1954.
- [40] D. Tabor, The physical meaning of indentation and scratch hardness, *Br. J. Appl. Phys.* 7 (5) (1956) 159.
- [41] K. Farrell, A. Schaffhauser, J. Stiegler, Recrystallization, grain growth and the ductile-brittle transition in tungsten sheet, *Journal of the Less Common Metals* 13 (2) (1967) 141–155.
- [42] W. D. Nix, H. Gao, Indentation size effects in crystalline materials: a law for strain gradient plasticity, *Journal of the Mechanics and Physics of Solids* 46 (3) (1998) 411–425.
- [43] R. Lowrie, A. Gonas, Dynamic elastic properties of polycrystalline tungsten, 24–1800 C, *Journal of Applied Physics* 36 (7) (1965) 2189–2192.
- [44] J. Kappacher, A. Leitner, H. Clemens, V. Maier-Kiener, Combination of nanoindentation and microscopy for the examination of aluminum alloys in coarse- and ultrafine-grained condition, *Practical Metallography* 56 (7) (2019) 432–442.

- [45] B. Backes, K. Durst, M. Goeken, Determination of plastic properties of polycrystalline metallic materials by nanoindentation: Experiments and finite element simulations, *Philosophical Magazine* 86 (33-35) (2006) 5541–5551.
- [46] J. Gale, A. Achuthan, The effect of work-hardening and pile-up on nanoindentation measurements, *Journal of materials science* 49 (14) (2014) 5066–5075.
- [47] W. Yao, J. You, Berkovich nanoindentation study of monocrystalline tungsten: a crystal plasticity study of surface pile-up deformation, *Philosophical Magazine* 97 (17) (2017) 1418–1435.
- [48] A. Bolshakov, G. Pharr, Influences of pileup on the measurement of mechanical properties by load and depth sensing indentation techniques, *Journal of materials research* 13 (4) (1998) 1049–1058.
- [49] V. Maier, C. Schunk, M. Göken, K. Durst, Microstructure-dependent deformation behaviour of bcc-metals—indentation size effect and strain rate sensitivity, *Philosophical Magazine* 95 (16-18) (2015) 1766–1779.
- [50] J.-O. Nilsson, Super duplex stainless steels, *Mater. Sci. Technol.* 8 (8) (1992) 685–700.
- [51] X. F. Wang, X. P. Yang, Z. D. Guo, Y. C. Zhou, H. W. Song, Nanoindentation characterization of mechanical properties of ferrite and austenite in duplex stainless steel, in: *Adv. Mater. Res.*, Vol. 26, Trans Tech Publ, 2007, pp. 1165–1170.
- [52] K. R. Gadelrab, G. Li, M. Chiesa, T. Souier, Local characterization of austenite and ferrite phases in duplex stainless steel using MFM and nanoindentation, *J. Mater. Res.* 27 (12) (2012) 1573–1579.
- [53] G. Speich, A. Schwoeble, W. C. Leslie, Elastic constants of binary iron-base alloys, *Metall. Trans.* 3 (8) (1972) 2031–2037.
- [54] D. Wu, H. Kahn, J. Dalton, G. Michal, F. Ernst, A. Heuer, Orientation dependence of nitrogen supersaturation in austenitic stainless steel during low-temperature gas-phase nitriding, *Acta Mater.* 79 (2014) 339–350.
- [55] T. Chen, L. Tan, Z. Lu, H. Xu, The effect of grain orientation on nanoindentation behavior of model austenitic alloy Fe-20Cr-25Ni, *Acta Mater.* 138 (2017) 83–91.
- [56] R. Dakhlaoui, C. Braham, A. Baczański, Mechanical properties of phases in austeno-ferritic duplex stainless steel—surface stresses studied by X-ray diffraction, *Mater. Sci. Eng. A* 444 (1-2) (2007) 6–17.
- [57] J. Roa, G. Fargas, A. Mateo, E. Jiménez-Piqué, Dependence of nanoindentation hardness with crystallographic orientation of austenite grains in metastable stainless steels, *Mater. Sci. Eng. A* 645 (2015) 188–195.
- [58] S. Chen, Y. Miyahara, A. Nomoto, Crystallographic orientation dependence of nanoindentation hardness in austenitic phase of stainless steel, *Phil. Mag. Lett.* 98 (11) (2018) 473–485.
- [59] G. Liu, Y. Wang, S. Li, K. Du, X. Wang, Deformation behavior of thermal aged duplex stainless steels studied by nanoindentation, EBSD and TEM, *Mater. High Temp.* 33 (1) (2016) 15–23.

- [60] R. M'Saoubi, H. Chandrasekaran, Role of phase and grain size on chip formation and material work hardening during machining of single and dual phase steels, *Ironmak. Steelmak.* 31 (3) (2004) 258–264.
- [61] T. Massalski, P. Subramanian, H. Okamoto, L. Kasprzak, *Binary alloy phase diagrams: Handbook*, in 3 vols (1990).
- [62] H. Bohm, Über das Ausscheidungsverhalten der binären Kupferlegierungen und seine Beeinflussung durch Zusätze, *Z. Metallkd.* 52 (9) (1961) 564–571.
- [63] X. Guoliang, W. Qiangsong, M. Xujun, X. Baiqing, P. Lijun, The precipitation behavior and strengthening of a Cu–2.0 wt% Be alloy, *Mater. Sci. Eng. A* 558 (2012) 326–330.
- [64] S. Spaic, M. Pristavec, Ausscheidungsverhalten in Cu-Ag-Legierungen, *Z. Metallkd.* 88 (12) (1997) 925–928.
- [65] J. Carpenter, S. Vogel, J. LeDonne, D. Hammon, I. Beyerlein, N. A. Mara, Bulk texture evolution of Cu–Nb nanolamellar composites during accumulative roll bonding, *Acta Mater.* 60 (4) (2012) 1576–1586.
- [66] J. Wang, K. Kang, R. Zhang, S. Zheng, I. Beyerlein, N. Mara, Structure and property of interfaces in ARB Cu/Nb laminated composites, *JOM* 64 (10) (2012) 1208–1217.
- [67] V. Maier-Kiener, X. An, L. Li, Z. Zhang, R. Pippan, K. Durst, Influence of solid solution strengthening on the local mechanical properties of single crystal and ultrafine-grained binary Cu–AlX solid solutions, *J. Mater. Res.* 32 (24) (2017) 4583–4591.
- [68] I. J. Beyerlein, N. A. Mara, J. S. Carpenter, T. Nizolek, W. M. Mook, T. A. Wynn, R. J. McCabe, J. R. Mayeur, K. Kang, S. Zheng, et al., Interface-driven microstructure development and ultra high strength of bulk nanostructured Cu-Nb multilayers fabricated by severe plastic deformation, *J. Mater. Res.* 28 (13) (2013) 1799.
- [69] S. Schwub, *Mikrostruktur, mechanische Eigenschaften und Schädigungsmechanismen von Kupfer-Silber-Zirkonium Legierungen für Hochtemperaturanwendungen*, Ph.D. thesis, Friedrich-Alexander-Universität Erlangen-Nürnberg, Erlangen, Deutschland (2012).
- [70] M.-M. Primorac, M. D. Abad, P. Hosemann, M. Kreuzeder, V. Maier, D. Kiener, Elevated temperature mechanical properties of novel ultra-fine grained Cu–Nb composites, *Mater. Sci. Eng. A* 625 (2015) 296–302.
- [71] B. Sestak, A. Seeger, Gleitung und Verfestigung in kubisch-raumzentrierten Metallen und Legierungen, *Z. Metallkd.* 69 (4) (1978) 195–202.
- [72] A. Argon, *Strengthening mechanisms in crystal plasticity*, Vol. 4, Oxford University Press, New York, 2008.
- [73] A. Seeger, The temperature and strain-rate dependence of the flow stress of body-centred cubic metals: A theory based on kink–kink interactions, *Z. Metallkd.* 72 (6) (1981) 369–380.

- [74] B. G. Butler, J. D. Paramore, J. P. Ligda, C. Ren, Z. Z. Fang, S. C. Middlemas, K. J. Hemker, Mechanisms of deformation and ductility in tungsten—a review, *Int. J. Refract. Met. H.* 75 (2018) 248–261.
- [75] V. Maier, A. Hohenwarter, R. Pippan, D. Kiener, Thermally activated deformation processes in body-centered cubic Cr—how microstructure influences strain-rate sensitivity, *Scripta Mater.* 106 (2015) 42–45.
- [76] D. Segall, A. Strachan, W. A. Goddard III, S. Ismail-Beigi, T. Arias, Ab initio and finite-temperature molecular dynamics studies of lattice resistance in tantalum, *Phys. Rev. B* 68 (1) (2003) 014104.
- [77] J. Li, C.-Z. Wang, J.-P. Chang, W. Cai, V. V. Bulatov, K.-M. Ho, S. Yip, Core energy and peierls stress of a screw dislocation in bcc molybdenum: A periodic-cell tight-binding study, *Phys. Rev. B* 70 (10) (2004) 104113.
- [78] D. Brunner, V. Glebovsky, Analysis of flow-stress measurements of high-purity tungsten single crystals, *Mater. Lett.* 44 (3-4) (2000) 144–152.
- [79] D. Caillard, Kinetics of dislocations in pure Fe. Part II. in situ straining experiments at low temperature, *Acta Mater.* 58 (9) (2010) 3504–3515.
- [80] D. Caillard, TEM in situ straining experiments in Fe at low temperature, *Phil. Mag. Lett.* 89 (8) (2009) 517–526.
- [81] J. R. Stephens, W. R. Witzke, Alloy softening in group VIA metals alloyed with rhenium, *J. Less-Common Metals* 23 (4) (1971) 325–342.
- [82] A. Luo, D. Jacobson, K. Shin, Solution softening mechanism of iridium and rhenium in tungsten at room temperature, *Int. J. Refract. Met. H.* 10 (2) (1991) 107–114.
- [83] Y.-J. Hu, M. R. Fellingner, B. G. Butler, Y. Wang, K. A. Darling, L. J. Kecskes, D. R. Trinkle, Z.-K. Liu, Solute-induced solid-solution softening and hardening in bcc tungsten, *Acta Mater.* 141 (2017) 304–316.
- [84] Y. Zhao, J. Marian, Direct prediction of the solute softening-to-hardening transition in W–Re alloys using stochastic simulations of screw dislocation motion, *Model. Simul. Mater. Sc.* 26 (4) (2018) 045002.
- [85] W. D. Klopp, Review of ductilizing of group VIA elements by rhenium and other solutes, NASA TN D-4955.
- [86] L. Romaner, C. Ambrosch-Draxl, R. Pippan, Effect of rhenium on the dislocation core structure in tungsten, *Phys. Rev. Lett.* 104 (19) (2010) 195503.
- [87] P. L. Raffo, Yielding and fracture in tungsten and tungsten-rhenium alloys, *J. Less-Common Metals* 17 (2) (1969) 133–149.

- [88] R. Z. Valiev, R. K. Islamgaliev, I. V. Alexandrov, Bulk nanostructured materials from severe plastic deformation, *Prog. Mater. Sci.* 45 (2) (2000) 103–189.
- [89] A. Zhilyaev, T. Langdon, Three-dimensional representations of hardness distributions after processing by high-pressure torsion, *Prog. Mater. Sci.* 53 (2008) 893–979.
- [90] Y. Saito, H. Utsunomiya, N. Tsuji, T. Sakai, Novel ultra-high straining process for bulk materials—development of the accumulative roll-bonding process, *Acta Mater.* 47 (2) (1999) 579–583.
- [91] R. Z. Valiev, T. G. Langdon, Principles of equal-channel angular pressing as a processing tool for grain refinement, *Prog. Mater. Sci.* 51 (7) (2006) 881–981.
- [92] M. A. Meyers, A. Mishra, D. J. Benson, Mechanical properties of nanocrystalline materials, *Prog. Mater. Sci.* 51 (4) (2006) 427–556.
- [93] Y. Li, X. Zeng, W. Blum, Transition from strengthening to softening by grain boundaries in ultrafine-grained Cu, *Acta Mater.* 52 (17) (2004) 5009–5018.
- [94] J. May, H. Höppel, M. Göken, Strain rate sensitivity of ultrafine-grained aluminium processed by severe plastic deformation, *Scripta Mater.* 53 (2) (2005) 189–194.
- [95] H. Conrad, Plastic deformation kinetics in nanocrystalline fcc metals based on the pile-up of dislocations, *Nanotechnology* 18 (32) (2007) 325701.
- [96] Q. Wei, S. Cheng, K. Ramesh, E. Ma, Effect of nanocrystalline and ultrafine grain sizes on the strain rate sensitivity and activation volume: fcc versus bcc metals, *Mat. Sci. Eng. A* 381 (1-2) (2004) 71–79.
- [97] J. Su, Z.-b. Tang, C.-x. Wang, T. Ye, T. Suo, Y.-l. Li, Compressive behavior and deformation kinetics of ultrafine grained aluminum processed by equal channel angular pressing, *Int. J. Smart Nano Mater.* 8 (1) (2017) 56–77.
- [98] L. Hollang, E. Hieckmann, D. Brunner, C. Holste, W. Skrotzki, Scaling effects in the plasticity of nickel, *Mater. Sci. Eng. A* 424 (1-2) (2006) 138–153.
- [99] T. Suo, Y.-l. Li, K. Xie, F. Zhao, K.-S. Zhang, Q. Deng, Experimental investigation on strain rate sensitivity of ultra-fine grained copper at elevated temperatures, *Mech. Mater.* 43 (3) (2011) 111–118.
- [100] N. Isaev, T. Grigorova, P. Zabrodin, Strain-rate sensitivity of the flow stress of ultrafine-grain aluminum at temperatures 4.2–295K, *Low Temp. Phys.* 35 (11) (2009) 898–904.
- [101] J. May, H. W. Höppel, M. Göken, Strain rate sensitivity of ultrafine grained fcc-and bcc-type metals, in: *Mater. Sci. Forum*, Vol. 503, Trans Tech Publ, 2006, pp. 781–786.
- [102] Q. Wei, T. Jiao, K. Ramesh, E. Ma, L. Kecskes, L. Magness, R. Dowding, V. Kazykhanov, R. Valiev, Mechanical behavior and dynamic failure of high-strength ultrafine grained tungsten under uniaxial compression, *Acta Mater.* 54 (1) (2006) 77–87.

- [103] D. Kiener, R. Fritz, M. Alfreider, A. Leitner, R. Pippan, V. Maier-Kiener, Rate limiting deformation mechanisms of bcc metals in confined volumes, *Acta Mater.* 166 (2019) 687–701.
- [104] A. Nazarov, Kinetics of grain boundary recovery in deformed polycrystals, *Interface Science* 8 (4) (2000) 315–322.
- [105] L. Priester, Grain boundaries: from theory to engineering, Vol. 172, Springer Science & Business Media, 2012.
- [106] O. Renk, V. Maier-Kiener, C. Motz, J. Eckert, D. Kiener, R. Pippan, How the interface type manipulates the thermochemanical response of nanostructured metals: A case study on nickel, *Materialia* (2021) 101020.
- [107] J. Wheeler, R. Raghavan, J. Michler, Temperature invariant flow stress during microcompression of a Zr-based bulk metallic glass, *Scripta Mater.* 67 (2) (2012) 125–128.
- [108] C. Su, E. G. Herbert, S. Sohn, J. A. LaManna, W. C. Oliver, G. M. Pharr, Measurement of power-law creep parameters by instrumented indentation methods, *J. Mech. Phys. Solids* 61 (2) (2013) 517–536.
- [109] S. Ruffell, J. Bradby, J. Williams, D. Munoz-Paniagua, S. Tadayyon, L. Coatsworth, P. Norton, Nanoindentation-induced phase transformations in silicon at elevated temperatures, *Nanotechnology* 20 (13) (2009) 135603.
- [110] J.-i. Jang, M. Lance, S. Wen, T. Y. Tsui, G. Pharr, Indentation-induced phase transformations in silicon: influences of load, rate and indenter angle on the transformation behavior, *Acta Mater.* 53 (6) (2005) 1759–1770.
- [111] J.-i. Jang, M. Lance, S. Wen, G. Pharr, Evidence for nanoindentation-induced phase transformations in germanium, *Appl. Phys. Lett.* 86 (13) (2005) 131907.
- [112] J. Pfetzinger-Micklich, R. Ghisleni, T. Simon, C. Somsen, J. Michler, G. Eggeler, Orientation dependence of stress-induced phase transformation and dislocation plasticity in NiTi shape memory alloys on the micro scale, *Mater. Sci. Eng. A* 538 (2012) 265–271.

Thermally activated deformation mechanisms and solid solution softening in W-Re alloys investigated via high temperature nanoindentation

Johann Kappacher, Alexander Leitner, Daniel Kiener, Helmut Clemens, Verena Maier-Kiener

Department of Materials Science, Montanuniversität Leoben, Austria

Abstract:

Thermally activated deformation mechanisms in three different W-Re alloys were investigated by performing high temperature nanoindentation experiments up to 800 °C. With increasing Re content the athermal hardness increases, while the temperature-dependent thermal contribution is strongly decreased. This results in a reduced strain rate sensitivity for W-Re alloys compared to pure W. The origin of this effect is a reduction of the Peierls potential due to Re, manifesting in an increased activation volume at lower temperatures. This gives rise to a solid solution softening effect, while at high-temperature application the mechanical behavior is governed by dislocation-dislocation interaction and solution strengthening.

Keywords:

refractory metals, high temperature deformation, plastic deformation, strain rate sensitivity

1. Introduction

Tungsten, the metal with the highest melting point T_m of 3422 °C, and its alloys are extensively used for high-temperature applications [1–3]. The most outstanding temperature-related characteristic of W in particular, and body-centered cubic (*bcc*) metals in general, is the drastic decrease in flow stress with increasing temperature [4, 5]. This is owed to the non-planar structure of the cores of $1/2\langle 111 \rangle$ screw dislocations, resulting in a high lattice resistance for slip [6, 7]. Thus, the shear stress for plastic deformation at low temperatures is high compared to face-centered cubic (*fcc*) metals. This phenomenon is commonly attributed to the Peierls stress and diminishes at temperatures above $\sim 0.2 T_m$ due to thermal activation of kink-pairs that migrate easily along the screw dislocation line [8, 9]. That part is therefore designated as thermal contribution to the flow stress and is responsible for the pronounced rate-dependent deformation behavior of W at room temperature (RT). Above $\sim 0.2 T_m$ screw and edge dislocations exhibit a similar mobility. This temperature regime is therefore designated as athermal, meaning that no additional thermal activation is required for deformation [4, 5].

Although its high melting point makes W a promising candidate for high-temperature applications, it has some major drawbacks. Due to its high brittle to ductile transition temperature it has a low fracture toughness, low elongation to failure and generally a low formability at ambient temperature [8]. To face these issues, alloying with Re was developed, as this leads to a ductilization effect [6, 10–12]. Because of the rarity of Re rendering it a very expensive metal, W-Re alloys are not used extensively on a large scale. The most common applications nowadays are as thermocouples or focal tracks of anodes for X-ray tubes [13]. For the development of plasma-facing components in fusion reactors it is furthermore necessary to understand the effect of Re in W [14–18].

Experimental evidence that Re decreases the Peierls potential in W were found in the late 60s [19]. More recently, Romaner *et al.* [6] proved the concept that alloying with Re changes the properties of the $1/2\langle 111 \rangle$ screw dislocation from a symmetric to an asymmetric core and hence leads to a reduction in Peierls stress. The origin of this intrinsic effect stems from filling of the *d* band, resulting in a modification of the intermetallic bonding. It is known for almost half a century that solid solution

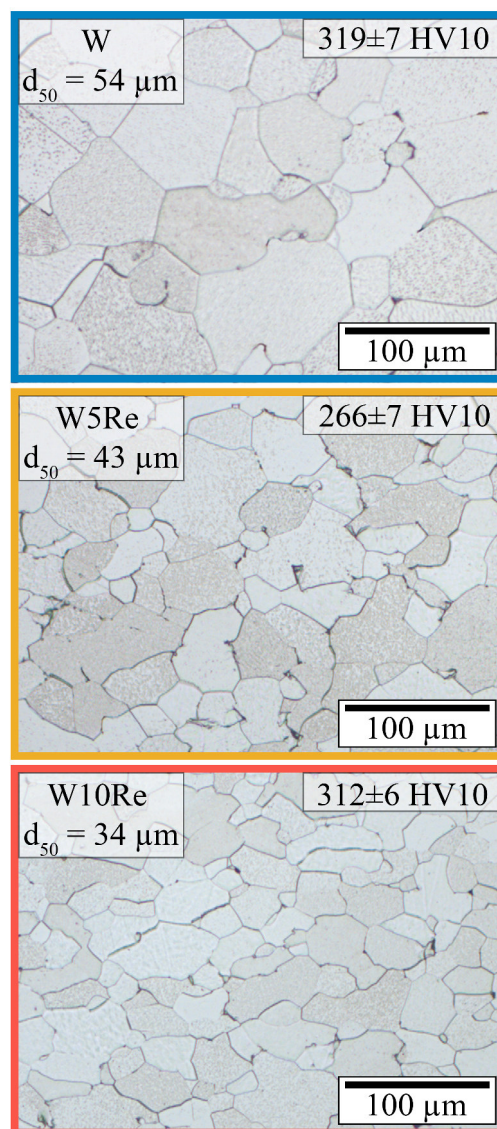


Figure 1: Light optical micrographs of the investigated coarse-grained materials. The grain boundaries were contrasted with a Murakami etching. Vickers hardness HV10 and mean grain sizes are indicated in the according image.

softening occurs in group VI elements when alloying with elements from group V to VIII [11]. The effect is strongly temperature dependent and disappears at temperatures above $\sim 0.2 T_m$ [11, 20]. Also, the solute content where the minimum hardness is reached depends strongly on the number of *s* and *d* electrons of the alloying element, leading to a highest solute content at the hardness-minimum for Re and lowest for Ni. At RT, a minimum in hardness is observed around 5% Re, which decreases with increasing temperature [20–23].

To experimentally study such effects in small volumes without the need for large quantities of expensive alloys, nanoindentation is the method of choice.

Hardness and Young's modulus of a material can be investigated at high accuracy and reproducibility [24]. With increasing popularity of this technique, advanced testing protocols became available [25], allowing to determine the strain rate sensitivity and activation volume of plastic deformation processes [26, 27]. These methods, combined with the possibility to test at elevated temperatures [28–31], provide a powerful tool to study thermally activated mechanisms for a better understanding of material behavior at higher temperatures.

2. Materials and Methods

Three different alloy compositions were tested in this study, namely commercially pure W, W5Re and W10Re (in wt%). All samples were provided by Plansee SE (Reutte, Austria). The initial coarse-grained microstructure resulted from a solution heat treatment at 1700 °C for 2 h. Light optical micrographs, including the average grain size are shown in figure 1. Additional Vickers hardness (HV10) measurements were performed on an Emco-Test M4C025G3M.

Nanoindentation experiments were conducted on an InSEM-HT (Nanomechanics Inc., KLA, Oak Ridge, TN) with a continuous stiffness measurement unit. The frequency of the superimposed force signal was 100 Hz with a displacement amplitude of 2 nm. The system is mounted in a Tescan Vega3 scanning electron microscope (Tescan, Brno, Czech Republic) under high vacuum ($< 5.0 \times 10^{-4}$ mbar) to prevent sample surface degradation or oxidation of the indenter at elevated temperatures [28]. A tungsten carbide Berkovich tip (Synton-MDP, Nidau, Switzerland) was used for all experiments. The frame stiffness and area function of the tip were obtained by indentation tests on a reference sample of fused quartz at RT according to the analysis of Oliver and Pharr [24]. To ensure correct contact temperatures a tip temperature calibration was performed by direct indentation into a thermocouple, as suggested by Wheeler and Michler [32]. Tip and sample are heated independently and carefully adjusted to stabilize the correct isothermal contact temperature. To follow any possible degradation of the indentation tip, after every tested sample indentations were performed on fused quartz. Also after high-temperature testing the samples surfaces were examined in a light optical microscope to exclude any surface oxidation.

Nanoindentation experiments were conducted from RT (25 °C) up to 800 °C with temperature increments of 100 °C. To acquire Young's modulus E and hardness H , experiments with a constant indentation strain rate [33] $\dot{\epsilon} = 0.5\dot{P}/P = 0.2 \text{ s}^{-1}$ up to a maximum indentation depth of 600 nm or to maximum load (50 mN) were performed. Hardness and Young's modulus at each temperature was averaged between indentation depths of 300 to 450 nm. To obtain strain rate sensitivity $m = \partial(\ln(H))/\partial(\ln(\dot{\epsilon}))$ and activation volume $V^* = C^* \cdot \sqrt{3} \cdot k_B \cdot T / (m \cdot H)$ of the materials, additional strain rate jump tests were performed,

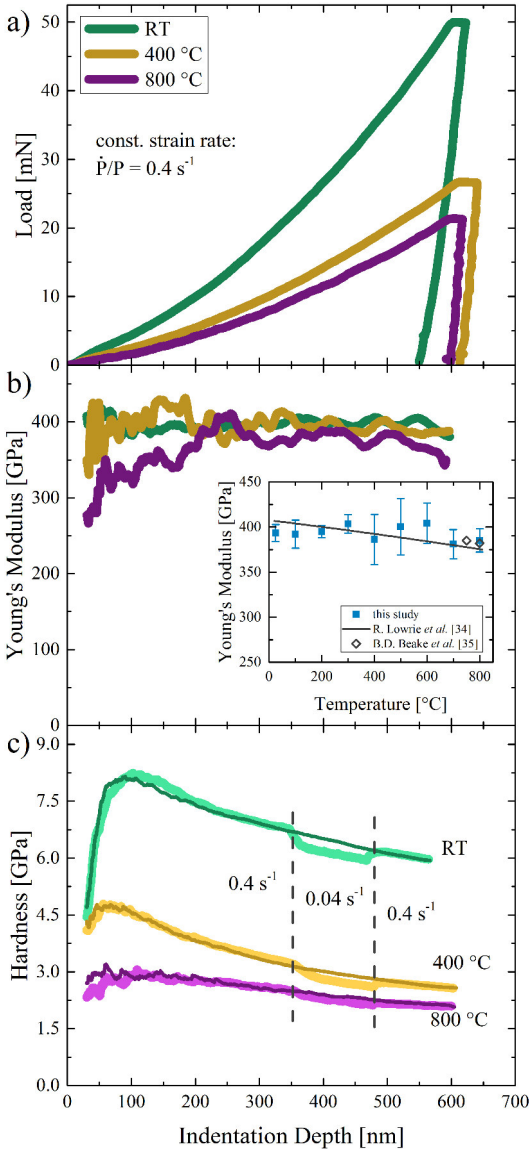


Figure 2: Representative indentation data for W at RT, 400 °C and 800 °C: a) load displacement curves, b) Young's modulus and c) hardness plotted over indentation depth for tests with constant indentation strain rate. The inset in b) shows the Young's modulus over temperature for technically pure W. In c) additional curves for strain rate jump tests are presented.

as introduced by Maier *et al.* [27], where C^* is a constraint factor of 2.8. Up to 350 nm the indentation strain rate was kept constant at $\dot{P}/P = 0.4 \text{ s}^{-1}$, followed by an abrupt rate change to $\dot{P}/P = 0.04 \text{ s}^{-1}$ for 125 nm and finally going back to the initial $\dot{P}/P = 0.4 \text{ s}^{-1}$ for another 125 nm. At least six valid indents were performed for every indentation protocol, material, as well as temperature.

3. Results

Comparing the Vickers hardness values for the three investigated materials in figure 1 indicates a pronounced solid solution softening effect. While W and W10Re exhibit almost identical values of 319 ± 7 and 312 ± 6 HV10, W5Re is significantly softer (266 ± 7 HV10). This is clearly linked to a change in the intrinsic material behavior, as for the continuously decreasing grain size from $54 \mu\text{m}$ (W) to $34 \mu\text{m}$ (W10Re) an increase in hardness according to Hall-Petch would be expected.

Figure 2 shows representative indentation data on W at RT, 400°C and 800°C . The top (a) and center (b) indicate load and Young's modulus versus displacement for constant indentation strain rate tests. In the inset of figure 2b Young's modulus for W is shown as a function of temperature with additional literature values [34, 35]. The continuously recorded constant Young's modulus over indentation depth, as well as the accordance of our data with literature emphasize the accuracy of this data even at high temperatures. Finally, in figure 2c hardness over displacement is displayed for both testing protocols, constant indentation strain rate as well as strain rate jump tests. As expected for coarse-grained materials a decrease in hardness with increasing indentation depth, a so-called indentation size effect [36], can be observed, but was not investigated in detail, as the main focus of this study is on thermally activated deformation processes.

The measured hardness as a function of the homologous temperature T/T_m for the three tested materials is illustrated in figure 3. T_m for W is 3695 K, while the solidus temperature for W5Re and W10Re strongly decreases to 3493 K and 3418 K, respectively [37]. The evolution of hardness over temperature is qualitatively similar for all three materials. From ambient to medium temperatures ($\sim 400^\circ\text{C}$) we observe a rapid decrease in hardness, followed by a less temperature-sensitive, athermal part at higher temperatures. The transition temperature between these two different behaviors is

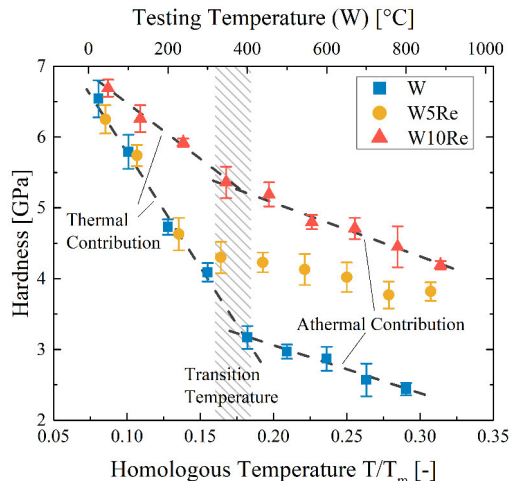


Figure 3: Evolution of hardness over homologous temperature T/T_m for the three investigated materials at constant indentation strain rates. Thermal and athermal contribution to hardness are highlighted for W and W10Re. The transition temperature between these two regimes is well pronounced around $0.2 T_m$.

slightly below $0.2 T_m$. With increasing Re-content the level of athermal hardness is increased, while the slope of the thermal part or temperature-sensitivity $\partial H/\partial(T/T_m)$ is decreased. Solid solution softening is evident at RT hardness values of 6.54, 6.25 and 6.69 GPa for W, W5Re and W10Re and can be observed for W5Re for 100°C and 200°C as well. Overcoming 300°C the effect reverses and solid solution hardening takes place.

Strain rate sensitivity, activation volume and activation energy are plotted as a function of temperature in figure 4. For the strain rate sensitivity (figure 4a) of W we observe an increase from 0.021 at RT to a peak of 0.037 at 300°C , followed by a steady decrease with increasing temperature. Alloying with Re lowers the strain rate sensitivity and no significant increase from ambient to medium temperatures can be observed. Overcoming approximately 400°C all three alloys show a steady decrease over temperature. The activation volume, normalized to the cubed Burgers vector b of W (0.274 nm), in figure 4b generally increases with rising temperature. Starting from a value of $8b^3$ for W at RT, it increases to above $200b^3$ at 800°C . The alloyed variants show a slightly higher activation volume below 400°C . This effect disappears at temperatures exceeding 500°C , where the activation volume is found independent of the alloy composition. From the hardness and Young's modulus data the apparent activation energy Q can be ascertained

using the modulus-compensated hot hardness analysis [38, 39] $H/E = G' \cdot \exp(Q \cdot m / (R \cdot T))$, where G' is a pre-exponential factor and R the gas constant. m -values are averaged in the associated temperature regime. This is summarized in figure 4c, where the data can be well described by a linear fit in two different temperature regimes.

4. Discussion

A typical evolution of hardness over temperature for *bcc* metals with a pronounced thermal and athermal contribution to flow stress [4, 5] can be observed in figure 3a. The athermal hardness values for W amounting to 40% of the RT hardness as well as a transition temperature around 400 °C are in excellent agreement with literature data [29, 40, 41]. Below 0.2 T_m alloying with Re manifests as a reduced temperature-sensitivity $\partial H / \partial (T/T_m)$. In the athermal deformation regime an increase in hardness for the alloyed materials can be observed, as is usually the case for solid solution strengthening [4]. The increase in athermal contribution on the one hand and the decrease in temperature sensitivity of the thermal contribution on the other hand leads to a solid solution softening for W5Re at RT up to 200 °C.

Figure 4a shows a pronounced rate-sensitivity for W at RT, which is typical for *bcc* metals [4, 9, 42]. An increase in strain rate sensitivity can be observed up to 300 °C, followed by a steady decrease at higher temperatures. It is assumed that the initial increase below 0.2 T_m , which is common for 'technically pure' or doped *bcc* metals, stems from a thermally activated interaction of kinks with impurity atoms [5, 42–44]. The decrease of strain rate sensitivity at temperatures above 0.2 T_m results from thermal activation of dislocation movement via kinks [9]. As alloying with Re increases the athermal hardness, it generally decreases the strain rate sensitivity. This behavior is commonly observed during solid solution softening in refractory metals [19, 45] and is closely related to the reduced temperature sensitivity in the temperature regime below 0.2 T_m . Notably, the strain rate sensitivity for W5Re remains constant, or even increases slightly between RT and 100 °C. It can be assumed that, as for the technically pure W, thermally activated interaction of dislocations with impurity atoms governs this behavior. This behavior diminishes at higher temperatures due to the dominating effect of the substitutional Re atoms

in the W lattice, a phenomenon that is described as 'scavenging' of interstitial impurities by solute atoms [46].

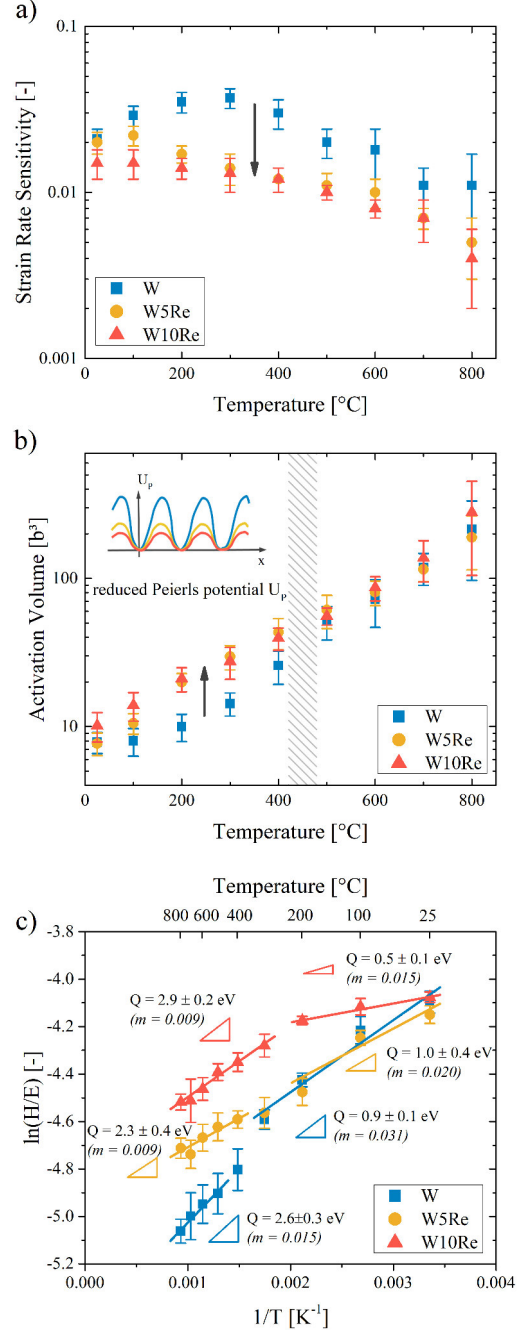


Figure 4: Strain rate sensitivity a), activation volume b) and activation energy c) as a function of temperature. In a) the arrow indicates the reduced strain rate sensitivity due to alloying with Re, while in b) the arrow highlights the increased activation volume as a result of the reduced Peierls potential. The temperature regime, where the activation volume is independent of the Re content (above 400 °C) is emphasized as well. c) shows how activation energies of plastic deformation are determined with the modulus-compensated hot hardness analysis for two different temperature regimes.

The activation volume describes the atoms collectively involved in the rate limiting deformation process [25] and is an indicator for the dominant plastic deformation mechanism. A value of around $10b^3$ at RT (figure 4b) points to a kink-pair mechanism [7], which is dominant at ambient temperatures for *bcc* metals in general [4, 9, 43]. At temperatures below 500 °C, the activation volume is significantly increased for the alloyed materials. This is related to a reduction in the Peierls potential due to the reorganization of the screw dislocation core by Re and the resulting increase in mobility, as reported in [6, 19]. Increasing the temperature to above 500 °C raises the activation volume to values larger than $100b^3$. This indicates that the deformation mechanism changes to dislocation-dislocation interaction via forest hardening, a more *fcc*-like behavior [5, 42, 43, 47]. It should be noted that there is no change in the activation volume of the technically pure W between RT and 100 °C. A conceivable explanation for that could be that impurity atoms hinder the thermal activation of kinks in that temperature regime. This assumption is supported by a similar observation for single crystal Cr [43, 47]. At testing temperatures of 500 °C and above, corresponding to $0.2 T_m$ for all three materials, the activation volume is independent of the Re content. As expected, this suggests that the rate limiting dislocation interaction in the athermal deformation regime is not affected by the alloying element.

The activation energy at low temperatures is significantly reduced for W10Re (0.5 ± 0.1 eV), while 0.9 ± 0.1 eV for W is close to the activation energy of kink-pair formation at the critical resolved shear stress between 127 and 227 °C (1.11 eV) [48], although others found slightly higher values [49, 50]. In references [47] and [49] it is assumed that kink-pair formation below $0.2 T_m$ can be subdivided into a line-tension and elastic interaction dominated regime. One could presume a similar behavior in the W-data in figure 4 from the small bend at 200 °C. To verify such a transient, narrower temperature increments would be necessary. In the present study, values are averaged over the whole thermally activated deformation regime, as the main focus lies on the temperature regime exceeding $0.2 T_m$, where only limited data can be found in literature. No significant influence of Re (2.6 ± 0.3 eV, 2.3 ± 0.4 eV and 2.9 ± 0.2 eV for W, W5Re and W10Re, respectively) on the activation energy was observed.

5. Conclusion

Advanced high temperature nanoindentation methods were applied to study thermally activated deformation mechanisms in binary W-Re alloys. For that purpose three different coarse-grained alloys, namely commercially pure W, W5Re and W10Re were tested.

A reduction of the Peierls potential in W due to Re alloying was observed as an increased activation volume of plastic deformation below $0.2 T_m$. This results in a significantly decreased strain rate sensitivity and temperature dependency for the alloyed material variants. While the hardness in the athermal temperature regime was increased through conventional solid solution strengthening, the temperature-sensitivity in the thermal regime was drastically reduced. These two oppositional influences lead to the occurrence of solid solution softening in W5Re up to 300 °C.

To the authors' knowledge this is the first study that focuses on the plastic deformation behavior of W-Re alloys at temperatures significantly above the transition temperature from thermal to athermal flow stress. While solid solution softening can in some conditions be observed at low temperatures, at forming or application temperatures the mechanical behavior is governed by dislocation-dislocation interaction and a solution strengthening effect.

Acknowledgments

The authors want to thank Plansee SE for providing the material. D.K. acknowledges funding by the European Research Council under Grant number 771146 (TOUGHIT).

References

- [1] S. Oghi, On the coarsening of non-sag tungsten lamp filament wires, *J. Phys. Soc. Jpn.* 11 (5) (1956) 593–598. doi:<https://doi.org/10.1143/JPSJ.11.593>.
- [2] T. Palacios, J. Reiser, J. Hoffmann, M. Rieth, A. Hoffmann, J. Pastor, Microstructural and mechanical characterization of annealed tungsten (w) and potassium-doped tungsten foils, *Int. J. Refract. Met. H.* 48 (2015) 145–149. doi:<https://doi.org/10.1016/j.ijrmhm.2014.09.005>.
- [3] I. Šmid, H. Pacher, G. Vieider, U. Mszanowski, Y. Igitkhanov, G. Janeschitz, J. Schlosser, L. Plöchl, Lifetime of be-, fcc- and w-armoured iter diverter plates, *J. Nucl. Mater.* 233 (1996) 701–707. doi:[https://doi.org/10.1016/S0022-3115\(96\)00309-1](https://doi.org/10.1016/S0022-3115(96)00309-1).

- [4] A. Argon, *Strengthening mechanisms in crystal plasticity*, Vol. 4, Oxford University Press, New York, 2008.
- [5] A. Seeger, The temperature and strain-rate dependence of the flow stress of body-centred cubic metals: A theory based on kink-kink interactions, *Z. Metallkd.* 72 (6) (1981) 369–380.
- [6] L. Romaner, C. Ambrosch-Draxl, R. Pippan, Effect of rhenium on the dislocation core structure in tungsten, *Phys. Rev. Lett.* 104 (19) (2010) 195503. doi:https://doi.org/10.1103/PhysRevLett.104.195503.
- [7] B. Sestak, A. Seeger, Gleitung und verfestigung in kubisch-raumzentrierten metallen und legierungen, *Z. Metallkd.* 69 (4) (1978) 195–202.
- [8] B. G. Butler, J. D. Paramore, J. P. Ligda, C. Ren, Z. Z. Fang, S. C. Middlemas, K. J. Hemker, Mechanisms of deformation and ductility in tungsten—a review, *Int. J. Refract. Met. H.* 75 (2018) 248–261. doi:https://doi.org/10.1016/j.ijrmhm.2018.04.021.
- [9] V. Maier, A. Hohenwarter, R. Pippan, D. Kiener, Thermally activated deformation processes in body-centered cubic cr—how microstructure influences strain-rate sensitivity, *Scripta Mater.* 106 (2015) 42–45. doi:https://doi.org/10.1016/j.scriptamat.2015.05.001.
- [10] G. Geach, J. Hughes, *Plansee proceedings*, Plansee Proceedings XXII (1956) 245–253.
- [11] W. D. Klopp, Review of ductilizing of group via elements by rhenium and other solutes, NASA TN D-4955.
- [12] H. Gao, R. Zee, Effects of rhenium on creep resistance in tungsten alloys, *J. Mater. Sci. Lett.* 20 (10) (2001) 885–887. doi:https://doi.org/10.1023/A:1010915012522.
- [13] A. Elsas, T. Zimmer, Höhere belastung von drehanodenröhren durch verwendung von legierten anoden, *Rofo. Fortschr. Rontg.* 97 (10) (1962) 511–514.
- [14] H. Bolt, V. Barabash, W. Krauss, J. Linke, R. Neu, S. Suzuki, N. Yoshida, A. U. Team, Materials for the plasma-facing components of fusion reactors, *J. Nucl. Mater.* 329 (2004) 66–73. doi:https://doi.org/10.1016/j.jnucmat.2004.04.005.
- [15] T. Tanno, M. Fukuda, S. Nogami, A. Hasegawa, Microstructure development in neutron irradiated tungsten alloys, *Mater. Trans.* (2011) 1447–1451 doi:https://doi.org/10.2320/matertrans.MBW201025.
- [16] J. Webb, S. Gollapudi, I. Charit, An overview of creep in tungsten and its alloys, *Int. J. Refract. Met. H.* doi:https://doi.org/10.1016/j.ijrmhm.2019.03.022.
- [17] C. E. Beck, S. G. Roberts, P. D. Edmondson, D. E. Armstrong, Effect of alloy composition & helium ion-irradiation on the mechanical properties of tungsten, tungsten-tantalum & tungsten-rhenium for fusion power applications, *MRS Online Proceedings Library Archive* 1514 (2013) 99–104. doi:https://doi.org/10.1557/opl.2013.356.
- [18] A. Xu, C. Beck, D. E. Armstrong, K. Rajan, G. D. Smith, P. A. Bagot, S. G. Roberts, Ion-irradiation-induced clustering in w-re and w-re-os alloys: A comparative study using atom probe tomography and nanoindentation measurements, *Acta Materialia* 87 (2015) 121–127. doi:https://doi.org/10.1016/j.actamat.2014.12.049.
- [19] P. L. Raffo, Yielding and fracture in tungsten and tungsten-rhenium alloys, *J. Less-Common Metals* 17 (2) (1969) 133–149. doi:https://doi.org/10.1016/0022-5088(69)90047-2.
- [20] Y. Zhao, J. Marian, Direct prediction of the solute softening-to-hardening transition in w-re alloys using stochastic simulations of screw dislocation motion, *Model. Simul. Mater. Sc.* 26 (4) (2018) 045002. doi:https://doi.org/10.1088/1361-651X/aaacef.
- [21] J. R. Stephens, W. R. Witzke, Alloy softening in group via metals alloyed with rhenium, *J. Less-Common Metals* 23 (4) (1971) 325–342. doi:https://doi.org/10.1016/0022-5088(71)90043-9.
- [22] A. Luo, D. Jacobson, K. Shin, Solution softening mechanism of iridium and rhenium in tungsten at room temperature, *Int. J. Refract. Met. H.* 10 (2) (1991) 107–114. doi:https://doi.org/10.1016/0263-4368(91)90028-M.
- [23] Y.-J. Hu, M. R. Fellingner, B. G. Butler, Y. Wang, K. A. Darling, L. J. Kecskes, D. R. Trinkle, Z.-K. Liu, Solute-induced solid-solution softening and hardening in bcc tungsten, *Acta Mater.* 141 (2017) 304–316. doi:https://doi.org/10.1016/j.actamat.2017.09.019.
- [24] W. C. Oliver, G. M. Pharr, An improved technique for determining hardness and elastic modulus using load and displacement sensing indentation experiments, *J. Mater. Res.* 7 (6) (1992) 1564–1583. doi:https://doi.org/10.1557/JMR.1992.1564.
- [25] V. Maier-Kiener, K. Durst, Advanced nanoindentation testing for studying strain-rate sensitivity and activation volume, *J. Mater. Res.* 69 (11) (2017) 2246–2255. doi:https://doi.org/10.1007/s11837-017-2536-y.
- [26] R. Schwaiger, B. Moser, M. Dao, N. Chollacoop, S. Suresh, Some critical experiments on the strain-rate sensitivity of nanocrystalline nickel, *Acta Mater.* 51 (17) (2003) 5159–5172. doi:https://doi.org/10.1016/S1359-6454(03)00365-3.
- [27] V. Maier, K. Durst, J. Mueller, B. Backes, H. W. Höppel, M. Göken, Nanoindentation strain-rate jump tests for determining the local strain-rate sensitivity in nanocrystalline ni and ultrafine-grained al, *J. Mater. Res.* 26 (11) (2011) 1421–1430. doi:https://doi.org/10.1557/jmr.2011.156.
- [28] J. Wheeler, D. Armstrong, W. Heinz, R. Schwaiger, High temperature nanoindentation: The state of the art and future challenges, *Curr. Opin. Solid St. M.* 19 (6) (2015) 354–366. doi:https://doi.org/10.1016/j.cossms.2015.02.002.

- [29] A. J. Harris, B. D. Beake, D. E. Armstrong, M. I. Davies, Development of high temperature nanoindentation methodology and its application in the nanoindentation of polycrystalline tungsten in vacuum to 950 c, *Exp. Mech.* 57 (7) (2017) 1115–1126. doi:<https://doi.org/10.1007/s11340-016-0209-3>.
- [30] B. D. Beake, A. J. Harris, Nanomechanics to 1000 c for high temperature mechanical properties of bulk materials and hard coatings, *Vacuum* 159 (2019) 17–28. doi:<https://doi.org/10.1016/j.vacuum.2018.10.011>.
- [31] J. S.-L. Gibson, S. Schröders, C. Zehnder, S. Korte-Kerzel, On extracting mechanical properties from nanoindentation at temperatures up to 1000 c, *Extreme Mech. Lett.* 17 (2017) 43–49. doi:<https://doi.org/10.1016/j.eml.2017.09.007>.
- [32] J. Wheeler, J. Michler, Elevated temperature, nano-mechanical testing in situ in the scanning electron microscope, *Rev. Sci. Instrum.* 84 (4) (2013) 045103. doi:<https://doi.org/10.1063/1.4795829>.
- [33] B. Lucas, W. Oliver, Indentation power-law creep of high-purity indium, *Metall. Mater. Trans. A* 30 (3) (1999) 601–610. doi:<https://doi.org/10.1007/s11661-999-0051-7>.
- [34] R. Lowrie, A. Gonas, Dynamic elastic properties of polycrystalline tungsten, 24–1800 c, *J. Appl. Phys.* 36 (7) (1965) 2189–2192. doi:<https://doi.org/10.1063/1.1714447>.
- [35] B. D. Beake, A. J. Harris, J. Moghal, D. E. Armstrong, Temperature dependence of strain rate sensitivity, indentation size effects and pile-up in polycrystalline tungsten from 25 to 950 c, *Mater. Des.* 156 (2018) 278–286. doi:<https://doi.org/10.1016/j.matdes.2018.06.063>.
- [36] W. D. Nix, H. Gao, Indentation size effects in crystalline materials: a law for strain gradient plasticity, *J. Mech. Phys. Solids* 46 (3) (1998) 411–425. doi:[https://doi.org/10.1016/S0022-5096\(97\)00086-0](https://doi.org/10.1016/S0022-5096(97)00086-0).
- [37] E. Savitskii, M. Tytkina, S. Ipatova, E. Pavlova, Properties of tungsten-rhenium alloys, *Met. Sci. Heat Treat.* 2 (9) (1960) 483–486.
- [38] O. Renk, V. Maier-Kiener, I. Issa, J. Li, D. Kiener, R. Pippan, Anneal hardening and elevated temperature strain rate sensitivity of nanostructured metals: Their relation to intergranular dislocation accommodation, *Acta Mater.* 165 (2019) 409–419. doi:<https://doi.org/10.1016/j.actamat.2018.12.002>.
- [39] O. Sherby, P. Armstrong, Prediction of activation energies for creep and self-diffusion from hot hardness data, *Metall. Mater. Trans. B* 2 (12) (1971) 3479–3484. doi:<https://doi.org/10.1007/BF02811630>.
- [40] J. S.-L. Gibson, S. G. Roberts, D. E. Armstrong, High temperature indentation of helium-implanted tungsten, *Mat. Sci. Eng. A* 625 (2015) 380–384. doi:<https://doi.org/10.1016/j.msea.2014.12.034>.
- [41] X. Xiao, D. Terentyev, A. Ruiz, A. Zinovev, A. Bakaev, E. E. Zhurkin, High temperature nanoindentation of tungsten: Modelling and experimental validation, *Mat. Sci. Eng. A* 743 (2019) 106–113. doi:<https://doi.org/10.1016/j.msea.2018.11.079>.
- [42] D. Brunner, V. Glebovsky, Analysis of flow-stress measurements of high-purity tungsten single crystals, *Mater. Lett.* 44 (3–4) (2000) 144–152. doi:[https://doi.org/10.1016/S0167-577X\(00\)00017-3](https://doi.org/10.1016/S0167-577X(00)00017-3).
- [43] D. Kiener, R. Fritz, M. Alfreider, A. Leitner, R. Pippan, V. Maier-Kiener, Rate limiting deformation mechanisms of bcc metals in confined volumes, *Acta Mater.* 166 (2019) 687–701. doi:<https://doi.org/10.1016/j.actamat.2019.01.020>.
- [44] J. W. Christian, B. Masters, Low-temperature deformation of body-centred cubic metals i. yield and flow stress measurements, *Proc. Royal Soc. Lond. A* 281 (1385) (1964) 223–239. doi:<https://doi.org/10.1098/rspa.1964.0180>.
- [45] S. Nemat-Nasser, R. Kapoor, Deformation behavior of tantalum and a tantalum tungsten alloy, *Int. J. Plasticity* 17 (10) (2001) 1351–1366. doi:[https://doi.org/10.1016/S0749-6419\(00\)00088-7](https://doi.org/10.1016/S0749-6419(00)00088-7).
- [46] K. Ravi, R. Gibala, The strength of niobium-oxygen solid solutions, *Acta Metall. Mater.* 18 (6) (1970) 623–634. doi:[https://doi.org/10.1016/0001-6160\(70\)90091-X](https://doi.org/10.1016/0001-6160(70)90091-X).
- [47] I.-C. Choi, C. Brandl, R. Schwaiger, Thermally activated dislocation plasticity in body-centered cubic chromium studied by high-temperature nanoindentation, *Acta Mater.* 140 (2017) 107–115. doi:<https://doi.org/10.1016/j.actamat.2017.08.026>.
- [48] A. Giannattasio, S. G. Roberts, Strain-rate dependence of the brittle-to-ductile transition temperature in tungsten, *Philos. Mag.* 87 (17) (2007) 2589–2598. doi:<https://doi.org/10.1080/14786430701253197>.
- [49] D. Brunner, Comparison of flow-stress measurements on high-purity tungsten single crystals with the kink-pair theory, *Mater. T. JIM* 41 (1) (2000) 152–160. doi:<https://doi.org/10.2320/matertrans1989.41.152>.
- [50] L. Dezerald, L. Proville, L. Ventelon, F. Willaime, D. Rodney, First-principles prediction of kink-pair activation enthalpy on screw dislocations in bcc transition metals: V, nb, ta, mo, w, and fe, *Phys. Rev. B* 91 (9) (2015) 094105. doi:<https://doi.org/10.1103/PhysRevB.91.094105>.

Controlling the high temperature deformation behavior and thermal stability of ultra-fine grained W by Re alloying

Johann Kappacher¹, Oliver Renk², Daniel Kiener¹, Helmut Clemens¹, Verena Maier-Kiener¹

¹ *Department of Materials Science, Montanuniversität Leoben, Austria* ² *Erich Schmid Institute of Materials Science, Austrian Academy of Sciences, Leoben, Austria*

Abstract:

Due to their outstanding properties ultra-fine grained tungsten and its alloys are promising candidates to be used in harsh environments, hence it is crucial to understand their high temperature behavior and underlying deformation mechanisms. Therefore, advanced nanoindentation techniques were applied to ultra-fine grained tungsten-rhenium alloys up to 1073 K. A continuous hardness decrease up to $0.2 T_m$ is rationalized by a still dominating effect of the Peierls stress. However, the absence of well-established effects of Rhenium alloying, resulting in a reduced temperature dependence of strength for coarse grained microstructures, was interpreted as an indication for a diminishing role of kink-pair formation in ultra-fine grained metals with sufficiently fine grain size. Despite slight grain growth in W, dislocation-grain boundary interaction was identified as the dominating deformation mechanism above $0.2 T_m$. Interaction and accommodation of lattice dislocations with grain boundaries was affected by a reduced boundary diffusivity through alloying with Re.

Keywords:

grain boundaries, nano-indentation, nuclear materials

1. Introduction

Driven by increased requirements for high-performance applications, material developments tend towards the use of refined microstructures, as according to Hall and Petch [1, 2] the strength of a material can be increased that way. Severe plastic deformation techniques [3–6] enable synthesis of ultra-fine grained (ufg) and nanocrystalline (nc) materials on a bulk scale, hence the properties of such materials were studied with growing interest [7–10].

For the development of plasma-facing components in nuclear fusion reactors body-centered cubic (bcc) tungsten is a promising candidate due to its exceptional physical properties [11, 12]. With a high melting point, T_m , of 3695 K, good resistance for void swelling or sputtering as well as good thermal conductivity, which remains stable under irradiation, it is ideal for applications in such harsh environments [13, 14]. Decreasing the grain size to the ufg or nc regime even improves the radiation tolerance, as grain boundaries act as sinks for defects [15, 16]. The effect of the alloying element Rhenium is of particular interest, as due to a change of the core structure of the screw dislocations, ductility at ambient temperature can be improved [17, 18]. On the other hand, when W faces such nuclear environments it will be transmuted, resulting in an increase in Re content [19]. Re strongly influences the deformation behavior of coarse grained (cg) W at low temperatures [17, 18]. It induces a transition from a symmetric to an asymmetric core of the $1/2\langle 111 \rangle$ screw dislocation and leads to a reduction of the Peierl's barrier [20]. For cg W alloying with Re results in a reduced temperature- and strain rate sensitivity of the hardness and an increased activation volume below $0.2 T_m$ [21]. To fully utilize the considerable strengthening effect of ufg materials, it is therefore necessary to understand the combined influence of grain boundaries and Re content on the mechanical properties and the underlying deformation behavior, especially at high temperatures. To identify the rate controlling mechanisms of plastic deformation, important parameters such as the strain rate sensitivity, m , and the corresponding (apparent) activation volume, V^* , can be determined [22]. The latter is commonly normalized to the cubed Burgers vector b^3 in order to facilitate comparison between different materials.

In conventional cg face-centered cubic (fcc) metals a rather low m of around 10^{-3} and V^* -values of a few $100b^3$ are observed [23–25]. This indicates that dislocation-dislocation interactions such as cutting of forest dislocations are the rate controlling deformation mechanism [26]. With a decrease of the grain size to

submicron or nanoscaled dimensions intragranular dislocation interactions vanish. Here, emission or absorption processes of dislocations at grain boundaries become important. Accordingly, the resulting strain rate sensitivity increases by about an order of magnitude [23, 24], while V^* decreases to a few $10b^3$ [27, 28]. This is indicative of a change of the deformation mode from dislocation-dislocation to dislocation-grain boundary interactions [26]. The observed strain rate sensitivity is rather temperature independent up to 0.2 to $0.3 T_m$ [29–32], but increases as temperature rises. The cause of this behavior is thermally activated accommodation of lattice dislocations within the grain boundaries [33, 34] with increasing temperatures.

For bcc metals the flow stress below $0.2 T_m$ is composed of a thermal as well as an athermal part [22, 35]. The thermal contribution originates from the non-planar core structure of the $1/2\langle 111 \rangle$ screw dislocations, resulting in a limited mobility compared to edge dislocations. Hence, the movement of screw dislocations via the kink-pair mechanism is the rate limiting step for deformation [36]. The resulting pronounced strain rate sensitivity for cg or single crystalline (sx) bcc metals was intensively investigated for Cr ($m = 0.02 - 0.07$) [37–39], but also for other bcc elements such as Fe ($m = 0.05$) [28], Ta ($m = 0.06$) [28], V ($m = 0.045$) [28, 40], and W ($m = 0.02 - 0.03$) [21, 41].

Different to fcc metals, a decrease in grain size reduces the strain rate sensitivity of bcc metals [28, 38–40, 42, 43]. This is generally attributed to a major strengthening contribution from grain refinement, providing rather athermal, long range obstacles for dislocations, while the local Peierls barrier provides only limited contribution to the overall strength [37, 43, 44]. The corresponding activation volumes are reported to be below $10b^3$. Commonly this is associated with the kink-pair mechanism being still active, independent of the grain size during plastic deformation at low temperatures [28, 39, 41].

Overcoming $0.2 T_m$, the kink-pairs are fully thermally activated, screw and edge dislocations exhibit the same mobility and only athermal barriers contribute to the materials strength [35]. For cg materials this implies a reduced strain rate sensitivity at the order of 10^{-3} and activation volumes above $100b^3$ depending on the dislocation density, suggesting dislocation-dislocation interactions to remain the rate controlling process [21, 36]. Contrary, ufg bcc materials show an increased rate sensitivity and activation volumes of a few $10b^3$ above this critical temperature. This indicates a behavior similar to ufg fcc metals, where dislocation-grain boundary inter-

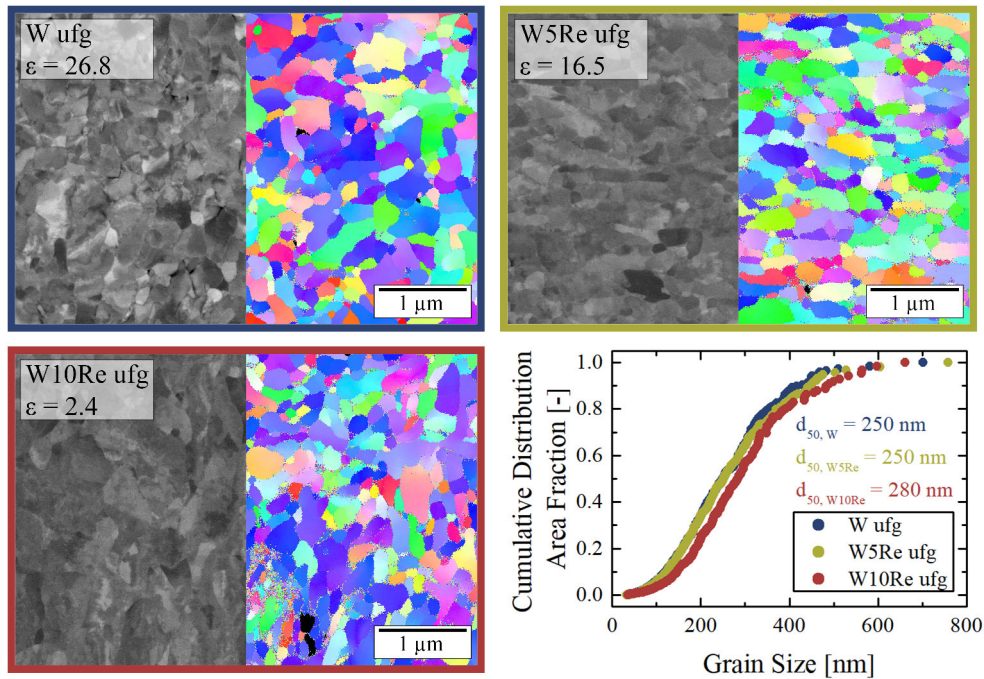


Figure 1: Microstructures (axial direction) of the investigated ufg W-Re alloys. The left side of the micrographs represent SEM images taken in BSE contrast, while the right sides are EBSD grain orientation maps. The mean grain sizes are indicated in the cumulative distribution plots. The shear direction of the HPT process is horizontal in all images.

actions dominate plastic deformation [37, 39, 41].

To expand the current understanding regarding microstructural stability as well as the influence of alloying on the thermally activated deformation mechanisms in ufg bcc metals, this work aims to investigate the deformation behavior of ufg W and W-Re alloys. Therefore, high temperature (HT) nanoindentation experiments are utilized to access dominating deformation mechanisms of these materials up to 1073 K, while high resolution electron microscopy and static annealing treatments were conducted to analyze the microstructural stability in dependence of the Re content.

2. Results

Figure 1 represents back-scattered electron (BSE) images as well as colored inverse pole figure (IPF) maps obtained from electron back-scatter diffraction (EBSD) of the investigated high pressure torsion (HPT) deformed materials before HT nanoindentation. The equivalent plastic strains are indicated in the respective image. A cumulative distribution plot of the grain size indicates very comparable characteristics with average grain sizes of around 250, 250 and 280 nm for W, W5Re and W10Re (composition in wt%), respectively. As typical for HPT deformed samples [45] the majority of the grain boundaries (>86 %) have a high-angle character (*i.e.* misorientation angles > 15°).

In figure 2 EBSD and BSE micrographs of the as-deformed and heat treated samples are presented. Additionally, cumulative distribution plots of the grain size evolution with annealing temperature are shown. Due to the slightly different plastic strains achieved during the HPT deformation process, the samples intended for the annealing experiments exhibit marginally different grain sizes (see section 5: Methodology). W has a grain size of around 290 nm in the as-HPT deformed state and shows slight grain growth to 320 nm already after annealing at 1073 K for 120 min. The selected annealing time corresponds to the holding time used for thermal stabilization during the HT nanoindentation experiments. W5Re, which has been subjected to the same equivalent strain in the HPT process, has a smaller grain size of around 230 nm, but grain growth to 270 nm starts only at 1273 K when annealed for 120 min. Due to the reduced strain that could be applied in case of W10Re, the grain size variation between the different samples is larger, but around 230 nm in the as-deformed state. Similar to the W5Re samples, significant grain growth was detected only at 1273 K, causing an increase to 280 nm after a holding time of 120 min.

RT hardness of the heat treated samples measured by nanoindentation as a function of annealing temperature is illustrated in figure 3. In the as-HPT condition hardness values of 11.10 ± 0.17 GPa, 12.09 ± 0.15 GPa and 10.59 ± 0.28 GPa for W, W5Re and W10Re, respec-

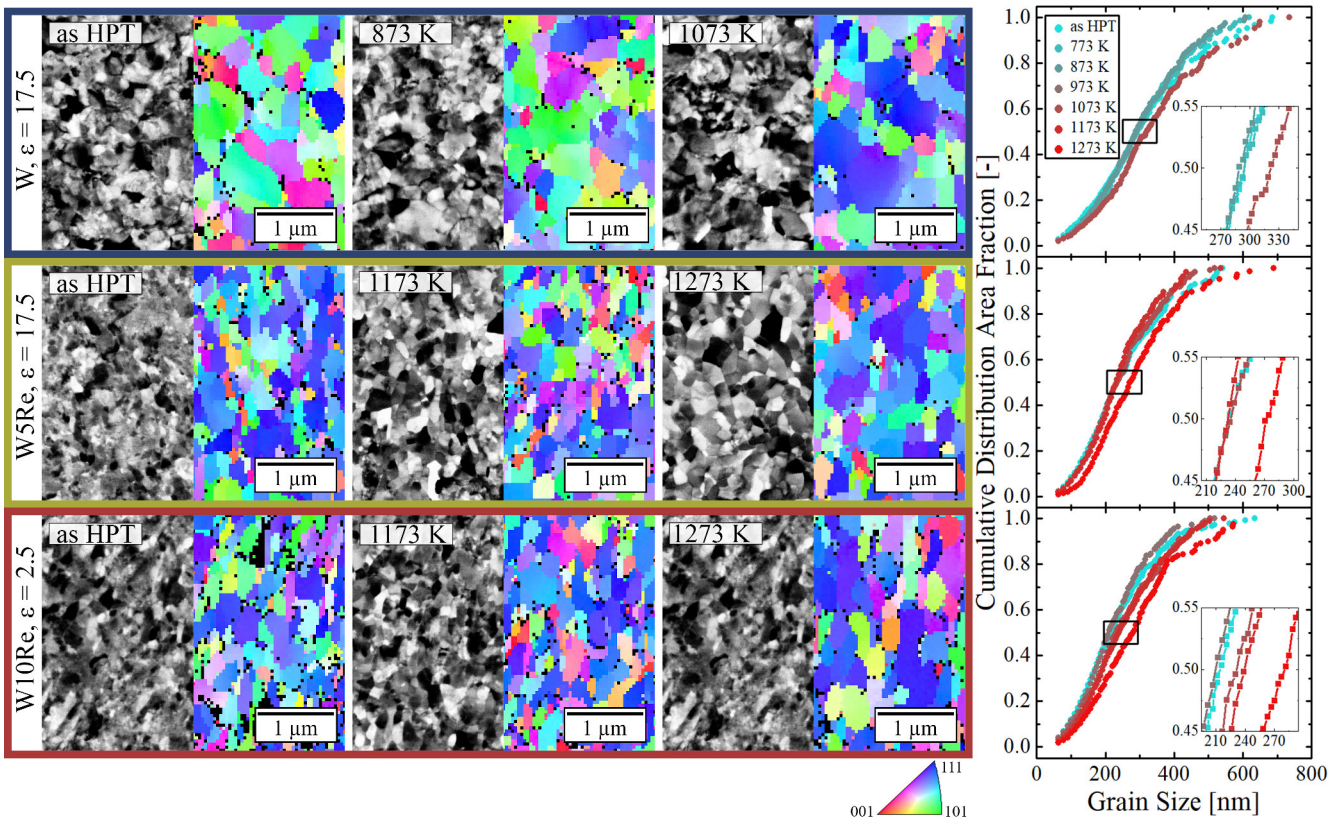


Figure 2: Microstructural evolution of W, W5Re and W10Re after annealing represented with SEM/BSE and EBSD micrographs. While W exhibits significant grain growth at 1073 K, W5Re and W10Re are thermally stable up to 1173 K. The duration of the heat treatment was 120 min for each indicated annealing temperature.

tively, were measured. Annealing the W samples at 723 K and 773 K does not result in any notable changes in hardness, while at 873 K a slight decrease of 4 % followed by a significant drop of 15 % at 1073 K was observed. For the alloyed variants no significant hardness reduction was detected up to 1173 K. Annealing at 1273 K, however, results in a decrease of 6 % and 11 % for W5Re and W10Re, respectively, in line with the grain size measurements.

In figure 4 representative indentation data is shown for ufg W at RT, 673 K and 1073 K. From the load displacement curves in figure 4a a distinct thermal dependence of hardness can be already noticed. The continuously recorded Young's moduli, E , show rather constant values over indentation depth and are in line with bulk data from Lowrie *et al.* [46], figure 4b. Figure 4c shows representative hardness versus displacement curves for both, constant strain rate as well as strain rate jump tests. A clear reduction in hardness with temperature is seen, while no influence of the testing protocol is evident.

The evolution of hardness, H , over homologous temperature based on the constant indentation strain rate experiments are displayed in figure 5a. The melting temperatures are 3695 K, 3493 K and 3418 K for W, W5Re

and W10Re, respectively [47]. For comparison, the temperature dependent hardness of the cg counterparts are presented in figure 5b [21]. Starting from very similar values at RT (11.64 ± 0.21 GPa, 11.51 ± 0.09 GPa and 11.19 ± 0.21 GPa for W, W5Re and W10Re, respectively) a strong decrease in hardness with testing temperature can be observed for all three materials. While for ufg W a steady decrease occurs over the whole testing temperature range, the hardness for W5Re and W10Re reaches a rather constant level for temperatures above 673 K.

The results of the strain rate jump tests and the derived activation parameters are shown in figure 6. The strain rate sensitivity, m , (figure 6a) exhibits two apparent regimes. At low temperatures, a constant strain rate sensitivity, independent of temperature and alloying elements, around 0.01 is observed. At higher temperatures, however, a pronounced increase of strain rate sensitivity with temperature can be detected. The temperature between these two regimes is shifted towards higher values with increasing Re content. With a linear fit the transition temperatures were estimated to be 600, 810 and 900 K for W, W5Re and W10Re, respectively. The calculated activation volumes, V^* , in figure 6b are slightly

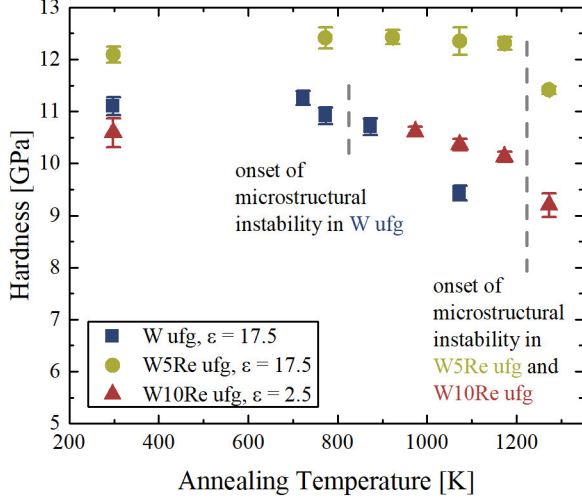


Figure 3: Evolution of RT hardness of the investigated materials as a function of annealing temperature. The duration of the heat treatments was fixed to 120 min, which corresponds to the average settle time to lower thermal drift during the HT nanoindentation experiments. While ufg W exhibits a significant decrease in hardness starting from 873 K, W5Re and W10Re are thermally stable up to 1173 K.

below $10b^3$ at RT. With increasing temperature the activation volume rises independent of the Re content. For comparison, the activation volumes of the same material, but in its cg condition are plotted in the same diagram [21]. While for the cg state V^* continuously increases, for the ufg states above $0.2 T_m$ the activation volume remains constant or even slightly decreases. In the high temperature regime W shows a lower activation volume of $19 \pm 6b^3$, when compared to W5Re ($30 \pm 11b^3$) and W10Re ($37 \pm 15b^3$). The third activation parameter that can be extracted from nanoindentation experiments to identify the rate controlling mechanism is the activation energy for plastic flow, Q .

$$Q \approx \Delta \mathcal{H} = \frac{H \cdot V^*}{\sqrt{3} \cdot C^* \cdot T} \cdot \frac{\partial(\ln H)}{\partial(1/T)} \quad (1)$$

It was approximated by the apparent activation enthalpy, $\Delta \mathcal{H}$, according to equation 1, introduced by Lee *et al.* [48], where C^* is a constraint factor of 2.8. The results are plotted as a function of temperature in figure 6c. Below $0.2 T_m$ values of 1.0 ± 0.5 , 1.6 ± 0.7 and 1.0 ± 0.3 eV for W, W5Re and W10Re were calculated, respectively. Above this critical temperature the two alloys exhibit low values of 0.2 ± 0.1 eV (W5Re) and 0.3 ± 0.1 eV (W10Re), while in ufg W an increased activation energy of 2.6 ± 0.9 eV can be observed.

3. Discussion

Regarding the microstructure of the HPT deformed materials, figure 1 reveals that in all cases the grain shape is globular or slightly elongated along the shear direction (horizontally) and the misorientation angle of the majority of boundaries is larger than 15° , *i.e.* they are high-angle grain boundaries [45]. Although different strains were applied to the three material variants, their grain sizes are almost identical. Also, the misorientation distribution for the different materials (not shown here) are qualitatively the same. Therefore, the grain boundary characters can be regarded as similar, allowing to assess the influence of Re alloying on the underlying deformation processes and the microstructural stability.

Static heat treatments regarding the microstructural evolution and RT hardness presented in figures 2 and 3 show that concerning the grain size of the ufg W samples a saturation of microstructural refinement is almost reached for strains of $\epsilon = 17.5$, as higher strains do not cause significant further refinement - 290 nm versus 250 nm after $\epsilon = 26.8$. The hardness of ufg W decreases slightly starting already at annealing temperatures of 873 K. In contrast to the hardness measurements, the grain size derived from EBSD measurements revealed significant grain growth starting at 1073 K after annealing for 120 min. A possible explanation could be that the step size for EBSD measurements of 40 nm impedes detection of slight grain growth events. This means that hardness measurements are more sensitive to slight microstructural changes, that are not easily accessible by EBSD. Compared to pure W, the alloyed sample W5Re was found to be thermally stable up to 1173 K. Here, grain growth accompanied by a hardness decrease starts at 1273 K. For W10Re, however, a stronger scatter for both, hardness and grain size, can be noticed. Probing different W10Re samples at the same strain before annealing revealed slightly different hardness values, reflected in a more prominent error bar. This can be attributed to the reduced equivalent strains that could be realized during HPT in case of W10Re, being far from saturation (at least $\epsilon > 17$ required), resulting in a less homogeneous microstructure. Similarly, the slight decrease of hardness for W10Re at annealing temperatures up to 1173 K (figure 3) as well as the scatter in grain size (figure 2) can be attributed to the prevailing inhomogeneous microstructure. Nevertheless, the thermal stability is similar to W5Re, with significant grain growth starting only at about 1273 K. The increase in thermal stability for W5Re and W10Re can be associated with the influence of solute atoms on the grain boundary mobility. An atmosphere of solute atoms is associated with

the grain boundary and its velocity is then controlled by the diffusion rate of the solute atoms in the bulk material, rather than by grain boundary diffusion in pure metals [49].

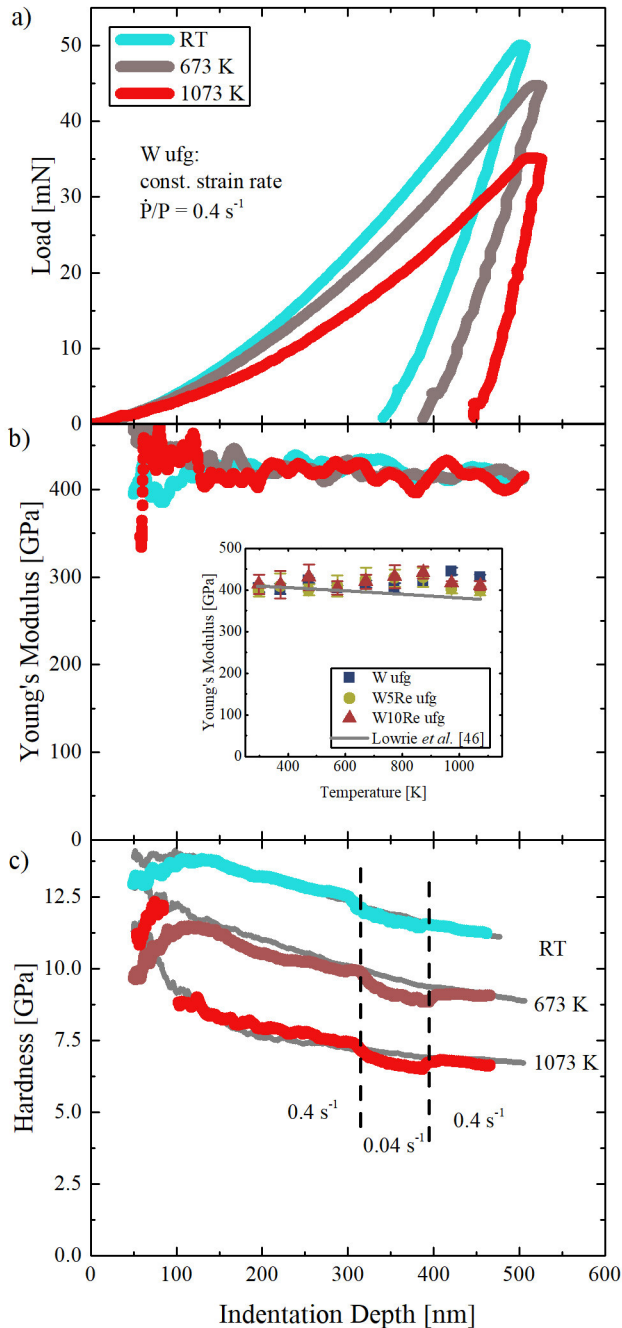


Figure 4: Representative indentation data for ufg W at RT, 673 K and 1073 K: a) load displacement curves, b) Young's modulus and c) hardness plotted over indentation depth for indents performed with constant indentation strain rate. The inset in b) shows the evolution of the Young's modulus with temperature and additional literature data for pure W [46]. In c) selected curves from the strain rate jump tests are presented in addition.

The constant Young's modulus over indentation depth (figure 4) and its excellent agreement with literature data

is a strong quantitative validation of our HT nanoindentation data. Notably, at 1073 K the measured Young's modulus is about 15 % higher compared to reference [46], which could arise from an increased pile-up behavior of the ufg materials at higher testing temperature [50]. Alloying with Re has no measurable effect on the Young's modulus, as supported by the results of Ayres *et al.* [51], who demonstrated that addition of 10 % Re has a negligible effect on the Young's modulus (*i.e.* 1.5 % at RT), which is below the standard deviations in our measurements. Hence, it is reasonable that the temperature-dependence of the Young's modulus in W-Re alloys is similar to pure W as seen in the present HT nanoindentation results.

Although the RT hardness values of the HT nanoindentation samples (figure 5a) are at a similar level, pure W and W5Re are slightly harder than W10Re. This can again be attributed to the slightly larger grain size of the W10Re sample and hence a reduced Hall-Petch hardening [1, 2]. Comparing the hardness values of W and the two Re alloyed variants over temperature, a very different behavior is observed. Commonly, cc metals with a bcc crystal structure show a drastically decreasing flow stress or hardness as temperature approaches $\sim 0.2 T_m$, where a rather constant plateau value is reached [22, 35] (compare figure 5b, data taken from reference [21]). In contrast, the ufg W sample shows a steady decrease of hardness over temperature without the occurrence of a pronounced athermal hardness plateau. Similar results were reported by Bonk *et al.* [52], who investigated cold rolled W with a grain size of 240 nm using high temperature tensile tests. Inspecting the microstructure after testing at 1073 K, grain growth from 250 nm to 300 nm could be noticed, as indicated in the inset in figure 5a. This thermally induced grain growth matches with the results of the static heat treatments (figure 3) and explains the absence of an athermal plateau and the observed continuous hardness decrease with increasing testing temperatures, respectively. A different behavior can be observed for the alloyed materials, where the Re atoms stabilize the ufg microstructure and suppress thermally induced grain growth up to the maximum testing temperature and an athermal plateau is evident. Although the grain size of W10Re is larger (280 nm compared to 250 nm) the athermal hardness level with 9.3 GPa is slightly higher compared to 9.0 GPa for W5Re. This increase can be associated with a solution hardening effect of Re, as observed for the cc counterparts at high temperatures [21]. However, comparing the athermal hardness plateau with cc W, W5Re and W10Re in figure 5b, a clearly different behavior can be

observed. For testing temperatures exceeding $\sim 0.2 T_m$, the ufg alloys reveal a truly athermal hardness plateau, where hardness becomes temperature invariant. In case of cg materials, however, hardness decreases further by about 20 % at these temperatures. Above $0.2 T_m$ dislocation motion and hence plastic deformation should be temperature independent, except for the contribution of the shear modulus, which only reduces marginally by 4 % within the temperature interval discussed. However, when using a Berkovich indenter, equivalent strains of 7.16 % are realized [53]. Hence, a sufficient number of dislocations and so work hardening is involved at low T_m , which becomes subdued at elevated temperatures due to dynamic recovery processes, reflected in decreasing hardness values. This is in line with work from Nemat-Nasser *et al.* [54, 55] showing that for cg Mo and Nb the work-hardening rate in a temperature range of 0.2 to $0.3 T_m$ decreases, *i.e.* dynamic recovery increases with temperature. As pronounced dislocation interactions are widely absent in the ufg W5Re and W10Re microstructures, a truly athermal behavior without any hardness reduction can be observed.

The rather similar transition temperatures just below $0.2 T_m$ in figure 5 for both the cg and ufg materials points towards the same mechanism responsible for the strong temperature dependence at low homologous temperatures. The activation volume, an indicator for the rate controlling process, is also very similar for both material states below $0.2 T_m$ (figure 6b). The respective average activation energies for plastic deformation are well within the range for kink-pair formation, where values between 1.10 and 1.75 eV are reported [56–59]. Taken together, these results point towards kink-pair formation as the rate-controlling deformation mechanism below $0.2 T_m$.

However, despite that, a main fingerprint of Re alloying is absent for the ufg condition. Due to its reduction of the Peierls potential [20] for cg W-Re alloys the temperature dependence of hardness as well as strain rate sensitivity and activation energy for plasticity are reduced below $0.2 T_m$ [60]. While these trends are well reproduced for the cg W-Re alloys [21], using the same experimental setup, it is not captured for the ufg conditions. This could be an indication that for bcc metals with a sufficiently fine grain size, the high shear stresses necessary for plastic deformation enhance screw dislocation mobility and the role of kink-pair formation as the rate controlling step for plasticity diminishes [61]. In fact, the stresses necessary to deform the ufg W and W-Re samples are almost twice as high compared to those required to deform the cg states (*i.e.* to form kink-pairs). These

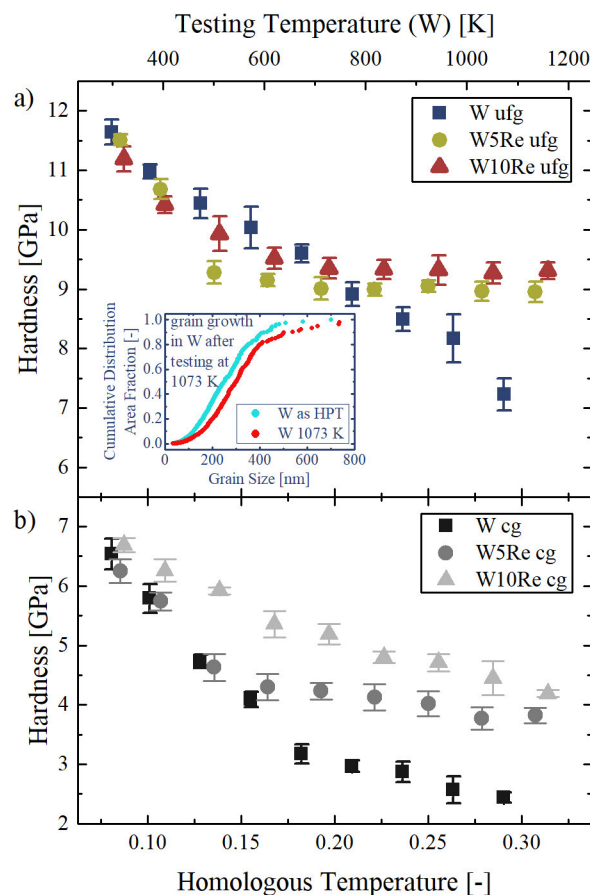


Figure 5: a) Evolution of hardness over testing temperature for the three investigated materials at constant indentation strain rates. W5Re and W10Re show a pronounced athermal deformation regime, while for W a gradual decrease of hardness over temperature can be observed. In b) previously reported data for the same materials in cg condition [21] is presented for comparison.

high stresses could facilitate mechanically driven kink-pair formation even at low temperatures.

The strain rate sensitivity tends to increase noticeably above a certain temperature, figure 6a. For such fine grained metals, the rate controlling processes above a critical temperature seem to be related to the interaction of dislocations with grain boundaries, either during propagation or the subsequent accommodation process [34]. The latter one, also referred to as intergranular stress relaxation, can be thermally facilitated above some temperature, explaining the increasing rate dependence of mechanical properties. Different accommodation processes are proposed in literature, for instance dislocation dissociation, core delocalization or incorporation. A delocalization of the dislocation core also leads to a thermal activation factor below $0.2 T_m$ although in this case the process would be mechanically driven. However, in any case the relaxation time scales inversely to the grain boundary diffusion coefficient [62]. This is con-

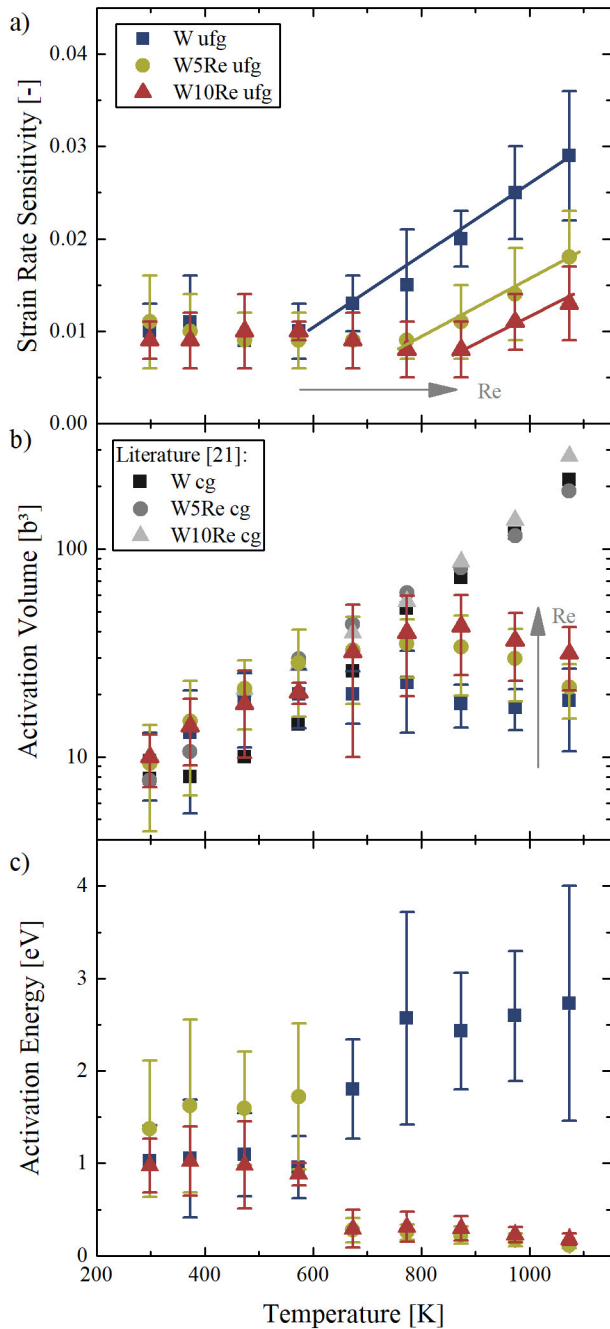


Figure 6: a) Strain rate sensitivity, b) activation volume and c) activation energy as a function of testing temperature. At temperatures below 673 K all three material parameters are unaffected by the alloying content. Re shifts the temperature, upon which m increases to higher values, while V^* is affected by the Re content at elevated testing temperatures. The activation volume for the three materials in cg condition is added for comparison [21]. At high temperatures the two alloys show a reduced, while ufg W exhibits an increased activation energy when compared to the values obtained below $0.2 T_m$.

sistent with our data, as the temperature where m rises is shifted towards higher values with increasing Re content, due to the reduction of grain boundary diffusivity.

Hence, higher temperatures are required for these diffusion controlled processes which increase the strain rate sensitivity. In line, also a comparison of the activation volumes between cg and ufg samples suggests a difference in the rate controlling mechanism for the ufg variants above the transition temperature as temperatures exceed $0.2 T_m$. In fact, V^* remains rather constant or to some extent even decreases slightly. A value of a few ten b^3 as well as an increased strain rate sensitivity points towards dislocation-grain boundary interaction as the dominant deformation mechanism [39]. Even though the grain size of W at 1073 K eventually becomes larger than W10Re, the activation volume is not significantly affected, as the grain size is still too small for extended dislocation storage and interaction. While according to equation 4 a higher hardness would lead to a lower activation volume in case of ufg W10Re, the addition of Re retards the thermal activation of dislocation-grain boundary interactions represented by a lower strain rate sensitivity. This contribution is stronger in the present case, thus leading to a higher activation volume for the alloyed material variants. We therefore conclude that alloying with Re intrinsically shifts the activation volume in ufg W to higher values at elevated temperatures. A possible explanation would be the effect of Re alloying on the core of screw dislocations [20]. Screw and edge dislocations have similar velocities through thermal activation above $0.2 T_m$. However, a contracted core of screw dislocations in case of the alloyed materials would give them a higher mobility, which eventually results in an increased activation volume. This picture is completed by the related activation energies, since plastic deformation mediated by dislocation-grain boundary interaction usually exhibits activation energies well below 1.0 eV [34, 48]. This is consistent with the results obtained for ufg W5Re and W10Re above 600 K. For ufg W, however, where significant grain growth occurred, the measured activation energy of 2.0 to 3.0 eV is closer to the value for grain boundary diffusion (around 3.9 eV [63]) that is responsible for grain growth.

4. Conclusion

Ultra-fine grained W and two binary W-Re alloys were investigated using advanced high temperature nanoindentation techniques to examine thermally activated deformation mechanisms over a broad range of temperatures. W, W5Re and W10Re were deformed by high pressure torsion to receive similar grain sizes (250 to 280 nm) and grain boundary characteristics. Upon annealing grain growth for ufg W starts at around 873 K, while alloying with Re suppresses it up to 1173 K. This

can be attributed to a pinning effect of the grain boundaries due to solute atoms. Consequently, a steady decrease of hardness over temperature for W was observed, while the microstructural stability of the W-Re alloys allows for a distinct athermal hardness plateau above $0.15 - 0.2 T_m$.

Comparison with results obtained on cg W and W-Re alloys show good agreement of the transition temperature between thermal and athermal evolution of hardness, activation volume and activation energy below $0.2 T_m$. While this suggests that the kink-pair mechanism also controls plasticity of the ufg samples, the absence of a clear effect of Re on the Peierls potential in the ufg W-Re alloys, suggests a shift of the rate-controlling mechanisms at the submicron scale. While still being subject to further research, it appears that local chemical effects for dislocations interacting with grain boundaries below $0.2 T_m$ can be more dominant than previously recognized.

Above $0.2 T_m$ dislocation-grain boundary mechanisms clearly become the rate controlling process, as evident from measured activation volumes and energies. The predominant processes are the interaction and accommodation of lattice dislocations with/at the grain boundaries. As their kinetics are determined by the boundary diffusivity, these processes will proceed facilitated above a certain temperature, explaining the enhanced strain rate dependence. Generally, Re shifts this increase in strain rate sensitivity to higher temperatures, consistent with intergranular stress relaxation scaling inversely with the grain boundary diffusion coefficient.

5. Methodology

Three different alloy compositions, W, W5Re and W10Re were provided by Plansee SE (Reutte, Austria) in a recrystallized state. The as-received samples were cut by electrical discharge machining into discs of 8 mm diameter and 1.2 mm in height. To receive an ufg microstructure these discs were subsequently deformed via high pressure torsion [10, 64] at 673 K applying a nominal pressure of 7.5 GPa at a rotation speed of 0.2 rpm. Elevated processing temperatures are required, as deformation of W by HPT is a difficult task owing to its high strength, going along with low ductility. Uniform deformation and grain refinement during HPT is, however, only possible as long as the strength of the sample remains below that of the anvils [65]. Alloying generally reduces the achievable grain size upon HPT, thus increases the strength, allowing only limited strains in case of the W-Re alloys before slippage occurs. Therefore, depending on the alloy, different equivalent plastic

strains were achieved according to equation 2 [45, 66], where n is the number of rotations, t the sample thickness and r the radius from the center of the disc. All microstructural as well as nanoindentation investigations on the HPT deformed samples were carried out in the axial direction of the discs after the samples were mechanically ground and mechano-chemically polished.

$$\varepsilon = \frac{2\pi n}{\sqrt{3t}} \cdot r \quad (2)$$

Micrographs of the material subjected to HT nanoindentation, including BSE images and EBSD based grain orientation maps, were acquired on a high resolution field emission SEM FEI Versa 3D DualBeam (Thermo Fisher Scientific, Waltham, MA), equipped with an EDAX Hikari XP EBSD-system (EDAX Inc., Mahwah, NJ). BSE images were recorded at 10 kV, while EBSD maps were acquired at 30 kV with a step size of 10 nm.

Static heat treatments were performed in a high vacuum furnace (HTM Reetz GmbH, Berlin, Germany) at a base pressure of $<5.0 \times 10^{-6}$ mbar. Samples were heated at a heating rate of 10 K min^{-1} until the desired temperature was reached, followed by a holding segment of 120 min before cooling back to RT at a rate of 10 K min^{-1} . A similar holding time was used as stabilization time during the high temperature nanoindentation experiments. Ufg W samples were annealed at 723, 773, 873, and 1073 K, ufg W5Re at 773, 923, 1073, 1173, and 1273 K and ufg W10Re at 973, 1073, 1173, and 1273 K. After the heat treatments RT nanoindentation experiments were performed on a G200 platform (KLA, Milpitas, CA). The system is equipped with a continuous stiffness measurement (CSM) unit, enabling the measurement of contact stiffness, thus hardness and Young's modulus, continuously over indentation depth. All tests were performed at a constant indentation strain rate [67] of $\dot{P}/P = 0.05 \text{ s}^{-1}$. A diamond Berkovich tip (Synton-MDP, Nidau, Switzerland) was used for these experiments. Hardness values are averaged between 500 and 1400 nm indentation depth. The microstructural evolution of the annealed samples was investigated using a QUANTAX EBSD-SEM system (Bruker Nano GmbH, Berlin, Germany) equipped to a LEO 1525 at 20 kV (Carl Zeiss Microscopy GmbH, Jena, Germany) using a step size of 40 nm. Around 2000 grains were measured for grain size evaluation. The equivalent strain, see Eq. 2, of the annealed materials was 17.5 for ufg W, 17.5 for ufg W5Re and 2.5 for ufg W10Re, respectively.

HT nanoindentation experiments were performed on an InSEM-HT (Nanomechanics Inc. KLA, Oak Ridge, TN) with a CSM unit and a separately heated tip and

sample to ensure an isothermal contact. The superimposed sinusoidal force signal had a frequency of 100 Hz and a displacement amplitude of 2 nm. The system is installed in a Tescan Vega3 SEM (Tescan, Brno, Czech Republic) under high vacuum conditions ($<5.0 \times 10^{-4}$ mbar). This excludes oxidation of the sample or degradation of the indenter at elevated temperatures [68] while at the same time allowing precise indent positioning as well as maintaining of the indentation process. A silicon carbide Berkovich tip (Synton-MDP, Nidau, Switzerland) was used for all high temperature experiments. Calibration of the frame stiffness and area function of the tip was performed by indentation tests on a reference sample of fused quartz at RT according to the analysis of Oliver and Pharr [69]. An additional tip temperature calibration was carried out by direct indentation into a thermocouple, as introduced by Wheeler and Michler [70]. After every tested sample additional indentations on fused quartz were performed to account for any possible degradation of the tip.

The nanoindentation experiments were performed from RT up to 1073 K in steps of 100 K. Young's modulus and hardness of the materials were obtained from experiments with constant indentation strain rate [67] $\dot{P}/P = 0.4 \text{ s}^{-1}$, with the reported values being averaged between 300 and 450 nm depth. The maximum indentation depth was either limited by the maximum force of 50 mN or a maximum indentation depth of 500 nm. In that case, the remaining indent is an equilateral triangle with an edge length of around $3.8 \mu\text{m}$, thus covering a significant amount of grain boundaries in the ufg materials.

$$m = \frac{\partial(\ln(H))}{\partial(\ln(\dot{\epsilon}))} \quad (3)$$

$$V^* = \frac{C^* \cdot \sqrt{3} \cdot k_B \cdot T}{m \cdot H} \quad (4)$$

Additional strain rate jump tests, as introduced by Maier *et al.* [71], were performed to deduce strain rate sensitivity m and apparent activation volume V^* . For that purpose the indentation strain rate was kept constant at $\dot{P}/P = 0.4 \text{ s}^{-1}$ until a displacement of 300 nm, followed by an abrupt change to $\dot{P}/P = 0.04 \text{ s}^{-1}$ for 80 nm and finally switching back to $\dot{P}/P = 0.4 \text{ s}^{-1}$ for another 80 nm. From the resulting change in hardness m and V^* can be calculated according to equations 3 and 4 with the Boltzmann constant k_B . The materials were investigated at different equivalent strains, namely 26.8 for ufg W, 16.5 for ufg W5Re and 2.4 for ufg W10Re. However, despite these differences the three samples could

be synthesized with similar grain sizes and grain boundary characters.

Acknowledgments

The authors want to thank Plansee SE for providing the material. J.K. wants to thank Michael Wurmshuber for his help with deforming the materials via high pressure torsion. D.K. acknowledges funding by the European Research Council under Grant number 771146 (TOUGHIT). This program is supported by the Austrian Federal Ministries for Climate Action, Environment, Energy, Mobility, Innovation and Technology (BMK) and for Digital and Economic Affairs (BMDW), represented by the Austrian research funding association (FFG), and the federal states of Styria, Upper Austria and Tyrol.

References

- [1] E. Hall, The deformation and ageing of mild steel: III discussion of results, *Proc. Phys. Soc. B* 64 (9) (1951) 747.
- [2] N. Petch, The cleavage strength of polycrystals, *J. Iron. Steel. I.* 174 (1953) 25–28.
- [3] R. Z. Valiev, T. G. Langdon, Principles of equal-channel angular pressing as a processing tool for grain refinement, *Prog. Mater. Sci.* 51 (7) (2006) 881–981.
- [4] A. Zhilyaev, T. Langdon, Three-dimensional representations of hardness distributions after processing by high-pressure torsion, *Prog. Mater. Sci.* 53 (2008) 893–979.
- [5] Y. Saito, H. Utsunomiya, N. Tsuji, T. Sakai, Novel ultra-high straining process for bulk materials—development of the accumulative roll-bonding (ARB) process, *Acta Mater.* 47 (2) (1999) 579–583.
- [6] R. Z. Valiev, R. K. Islamgaliev, I. V. Alexandrov, Bulk nanostructured materials from severe plastic deformation, *Prog. Mater. Sci.* 45 (2) (2000) 103–189.
- [7] H. Gleiter, Nanostructured materials: Basic concepts and microstructure, *Acta Mater.* 48 (1) (2000) 1–29.
- [8] J. Weertman, D. Farkas, K. Hemker, H. Kung, M. Mayo, R. Mitra, H. Van Swygenhoven, Structure and mechanical behavior of bulk nanocrystalline materials, *MRS Bull.* 24 (2) (1999) 44–53.
- [9] K. Kumar, H. Van Swygenhoven, S. Suresh, Mechanical behavior of nanocrystalline metals and alloys, *Acta Mater.* 51 (19) (2003) 5743–5774.
- [10] R. Pippan, S. Scheriau, A. Taylor, M. Hafok, A. Hohenwarter, A. Bachmaier, Saturation of fragmentation during severe plastic deformation, *Ann. Rev. Mater. Res.* 40 (2010) 319–343.
- [11] H. Bolt, V. Barabash, W. Krauss, J. Linke, R. Neu, S. Suzuki, N. Yoshida, Materials for the plasma-facing components of fusion reactors, *J. Nucl. Mater.* 329 (2004) 66–73.

- [12] T. Tanno, M. Fukuda, S. Nogami, A. Hasegawa, J.-C. He, A. Hasegawa, M. Fujiwara, M. Satou, T. Shishido, K. Abe, Microstructure development in neutron irradiated tungsten alloys, *Mater. Trans.* 52 (7) (2011) 1447–1451.
- [13] P. Norajitra, L. Boccaccini, A. Gervash, R. Giniyatulin, N. Holstein, T. Ihli, G. Janeschitz, W. Krauss, R. Kruessmann, V. Kuznetsov, Development of a helium-cooled divertor: material choice and technological studies, *J. Nucl. Mater.* 367 (2007) 1416–1421.
- [14] R. A. Causey, T. J. Venhaus, The use of tungsten in fusion reactors: a review of the hydrogen retention and migration properties, *Phys. Scripta* 2001 (T94) (2001) 9.
- [15] S. Wurster, R. Pippan, Nanostructured metals under irradiation, *Scripta Mater.* 60 (12) (2009) 1083–1087.
- [16] H. Kurishita, Y. Amano, S. Kobayashi, K. Nakai, H. Arakawa, Y. Hiraoka, T. Takida, K. Takebe, H. Matsui, Development of ultra-fine grained W–TiC and their mechanical properties for fusion applications, *J. Nucl. Mater.* 367 (2007) 1453–1457.
- [17] G. Geach, J. Hughes, Plansee proceedings, Plansee Proceedings XXII (1956) 245–253.
- [18] W. D. Klopp, Review of ductilizing of group VIA elements by rhenium and other solutes, NASA TN D-4955.
- [19] M. Gilbert, J.-C. Sublet, Neutron-induced transmutation effects in W and W-alloys in a fusion environment, *Nucl. Fusion* 51 (4) (2011) 043005.
- [20] L. Romaner, C. Ambrosch-Draxl, R. Pippan, Effect of rhenium on the dislocation core structure in tungsten, *Phys. Rev. Lett.* 104 (19) (2010) 195503.
- [21] J. Kappacher, A. Leitner, D. Kiener, H. Clemens, V. Maier-Kiener, Thermally activated deformation mechanisms and solid solution softening in W-Re alloys investigated via high temperature nanoindentation, *Mater. Des.* 189 (2020) 108499.
- [22] A. Argon, Strengthening mechanisms in crystal plasticity, Vol. 4, Oxford University Press, Oxford, 2008.
- [23] Y. Li, X. Zeng, W. Blum, Transition from strengthening to softening by grain boundaries in ultrafine-grained Cu, *Acta Mater.* 52 (17) (2004) 5009–5018.
- [24] J. May, H. Höppel, M. Göken, Strain rate sensitivity of ultrafine-grained aluminium processed by severe plastic deformation, *Scripta Mater.* 53 (2) (2005) 189–194.
- [25] H. Höppel, J. May, P. Eisenlohr, M. Göken, Strain-rate sensitivity of ultrafine-grained materials, *Z. Metallkd.* 96 (6) (2005) 566–571.
- [26] M. A. Meyers, A. Mishra, D. J. Benson, Mechanical properties of nanocrystalline materials, *Prog. Mater. Sci.* 51 (4) (2006) 427–556.
- [27] H. Conrad, Plastic deformation kinetics in nanocrystalline fcc metals based on the pile-up of dislocations, *Nanotechnology* 18 (32) (2007) 325701.
- [28] Q. Wei, S. Cheng, K. Ramesh, E. Ma, Effect of nanocrystalline and ultrafine grain sizes on the strain rate sensitivity and activation volume: fcc versus bcc metals, *Mat. Sci. Eng. A* 381 (1-2) (2004) 71–79.
- [29] J. Su, Z.-b. Tang, C.-x. Wang, T. Ye, T. Suo, Y.-l. Li, Compressive behavior and deformation kinetics of ultrafine grained aluminum processed by equal channel angular pressing, *Int. J. Smart Nano Mater.* 8 (1) (2017) 56–77.
- [30] L. Hollang, E. Hieckmann, D. Brunner, C. Holste, W. Skrotzki, Scaling effects in the plasticity of nickel, *Mater. Sci. Eng. A* 424 (1-2) (2006) 138–153.
- [31] T. Suo, Y.-l. Li, K. Xie, F. Zhao, K.-S. Zhang, Q. Deng, Experimental investigation on strain rate sensitivity of ultra-fine grained copper at elevated temperatures, *Mech. Mater.* 43 (3) (2011) 111–118.
- [32] N. Isaev, T. Grigorova, P. Zabrodin, Strain-rate sensitivity of the flow stress of ultrafine-grain aluminum at temperatures 4.2–295 K, *Low Temp. Phys.* 35 (11) (2009) 898–904.
- [33] N. Ahmed, A. Hartmaier, Mechanisms of grain boundary softening and strain-rate sensitivity in deformation of ultrafine-grained metals at high temperatures, *Acta Mater.* 59 (11) (2011) 4323–4334.
- [34] O. Renk, V. Maier-Kiener, I. Issa, J. Li, D. Kiener, R. Pippan, Anneal hardening and elevated temperature strain rate sensitivity of nanostructured metals: their relation to intergranular dislocation accommodation, *Acta Mater.* 165 (2019) 409–419.
- [35] A. Seeger, The temperature and strain-rate dependence of the flow stress of body-centred cubic metals: A theory based on kink–kink interactions, *Z. Metallkd.* 72 (6) (1981) 369–380.
- [36] B. Sestak, A. Seeger, Gleitung und Verfestigung in kubisch-raumzentrierten Metallen und Legierungen, *Z. Metallkd.* 69 (4) (1978) 195–202.
- [37] V. Maier, A. Hohenwarter, R. Pippan, D. Kiener, Thermally activated deformation processes in body-centered cubic Cr–Hf microstructure influences strain-rate sensitivity, *Scripta Mater.* 106 (2015) 42–45.
- [38] D. Wu, X. Wang, T. Nieh, Variation of strain rate sensitivity with grain size in Cr and other body-centred cubic metals, *J. Phys. D Appl. Phys.* 47 (17) (2014) 175303.
- [39] R. Fritz, D. Wimler, A. Leitner, V. Maier-Kiener, D. Kiener, Dominating deformation mechanisms in ultrafine-grained chromium across length scales and temperatures, *Acta Mater.* 140 (2017) 176–187.
- [40] Q. Wei, T. Jiao, K. Ramesh, E. Ma, Nano-structured vanadium: processing and mechanical properties under quasi-static and dynamic compression, *Scripta Mater.* 50 (3) (2004) 359–364.
- [41] D. Kiener, R. Fritz, M. Alfreider, A. Leitner, R. Pippan, V. Maier-Kiener, Rate limiting deformation mechanisms of bcc metals in confined volumes, *Acta Mater.* 166 (2019) 687–701.
- [42] J. May, H. W. Höppel, M. Göken, Strain rate sensitivity of ultrafine grained fcc-and bcc-type metals, in: *Mater. Sci. Forum*, Vol. 503, Trans Tech Publ, 2006, pp. 781–786.

- [43] Q. Wei, T. Jiao, K. Ramesh, E. Ma, L. Kecskes, L. Magness, R. Dowding, V. Kazykhanov, R. Valiev, Mechanical behavior and dynamic failure of high-strength ultrafine grained tungsten under uniaxial compression, *Acta Mater.* 54 (1) (2006) 77–87.
- [44] V. Maier, C. Schunk, M. Göken, K. Durst, Microstructure-dependent deformation behaviour of bcc-metals–indentation size effect and strain rate sensitivity, *Phil. Mag.* 95 (16-18) (2015) 1766–1779.
- [45] T. Hebesberger, H. Stüwe, A. Vorhauer, F. Wetscher, R. Pippan, Structure of Cu deformed by high pressure torsion, *Acta Mater.* 53 (2) (2005) 393–402.
- [46] R. Lowrie, A. Gonas, Dynamic elastic properties of polycrystalline tungsten, 24–1800 C, *J. Appl. Phys.* 36 (7) (1965) 2189–2192.
- [47] E. Savitskii, M. Tylkina, S. Ipatova, E. Pavlova, Properties of tungsten-rhenium alloys, *Met. Sci. Heat. Treat.* 2 (9) (1960) 483–486.
- [48] D.-H. Lee, I.-C. Choi, G. Yang, Z. Lu, M. Kawasaki, U. Ramamurty, R. Schwaiger, J.-i. Jang, Activation energy for plastic flow in nanocrystalline CoCrFeMnNi high-entropy alloy: A high temperature nanoindentation study, *Scripta Mater.* 156 (2018) 129–133.
- [49] F. J. Humphreys, M. Hatherly, *Recrystallization and related annealing phenomena*, Elsevier, Oxford, 2012.
- [50] B. D. Beake, A. J. Harris, J. Moghal, D. E. Armstrong, Temperature dependence of strain rate sensitivity, indentation size effects and pile-up in polycrystalline tungsten from 25 to 950° C, *Mater. Des.* 156 (2018) 278–286.
- [51] R. Ayres, G. Shannette, D. Stein, Elastic constants of tungsten-rhenium alloys from 77 to 298 K, *J. Appl. Phys.* 46 (4) (1975) 1526–1530.
- [52] S. Bonk, J. Hoffmann, A. Hoffmann, J. Reiser, Cold rolled tungsten (W) plates and foils: Evolution of the tensile properties and their indication towards deformation mechanisms, *Int. J. Refract. Met. H.* 70 (2018) 124–133.
- [53] A. Leitner, V. Maier-Kiener, D. Kiener, Extraction of flow behavior and Hall–Petch parameters using a nanoindentation multiple sharp tip approach, *Adv. Eng. Mater.* 19 (4) (2017) 1600669.
- [54] S. Nemat-Nasser, W. Guo, M. Liu, Experimentally-based micromechanical modeling of dynamic response of molybdenum, *Scripta Mater.* 40 (7) (1999) 859–872.
- [55] S. Nemat-Nasser, W. Guo, Flow stress of commercially pure niobium over a broad range of temperatures and strain rates, *Mater. Sci. Eng. A* 284 (1-2) (2000) 202–210.
- [56] D. Brunner, Comparison of flow-stress measurements on high-purity tungsten single crystals with the kink-pair theory, *Mater. Trans.* 41 (1) (2000) 152–160.
- [57] A. Giannattasio, S. G. Roberts, Strain-rate dependence of the brittle-to-ductile transition temperature in tungsten, *Phil. Mag.* 87 (17) (2007) 2589–2598.
- [58] L. Dezerald, L. Proville, L. Ventelon, F. Willaime, D. Rodney, First-principles prediction of kink-pair activation enthalpy on screw dislocations in bcc transition metals: V, Nb, Ta, Mo, W, and Fe, *Phys. Rev. B* 91 (9) (2015) 094105.
- [59] H. Li, C. Draxl, S. Wurster, R. Pippan, L. Romaner, Impact of d-band filling on the dislocation properties of bcc transition metals: The case of tantalum-tungsten alloys investigated by density-functional theory, *Phys. Rev. B* 95 (9) (2017) 094114.
- [60] P. L. Raffo, Yielding and fracture in tungsten and tungsten-rhenium alloys, *J. Less Common M.* 17 (2) (1969) 133–149.
- [61] Y. Cui, G. Po, N. Ghoniem, Temperature insensitivity of the flow stress in body-centered cubic micropillar crystals, *Acta Mater.* 108 (2016) 128–137.
- [62] L. Priester, On the accommodation of extrinsic dislocations in grain boundaries, *Interface Sci.* 4 (3-4) (1997) 205–219.
- [63] H. Mehrer, *Diffusion in Solid Metals and Alloys*, Vol. 26, Landolt-Börnstein, New Series, 1990.
- [64] O. Renk, R. Pippan, Saturation of grain refinement during severe plastic deformation of single phase materials: reconsiderations, current status and open questions, *Mater. Trans.* 60 (7) (2019) 1270–1282.
- [65] M. Wurmshuber, S. Dopfermann, S. Wurster, D. Kiener, Ultrafine-grained tungsten by high-pressure torsion–bulk precursor versus powder processing route, *IOP Conf. Ser. Mat. Sci.* 580 (2019) 012051.
- [66] H. P. Stüwe, Equivalent strains in severe plastic deformation, *Adv. Eng. Mater.* 5 (5) (2003) 291–295.
- [67] B. Lucas, W. Oliver, Indentation power-law creep of high-purity indium, *Metall. Mater. Trans. A* 30 (3) (1999) 601–610.
- [68] J. Wheeler, D. Armstrong, W. Heinz, R. Schwaiger, High temperature nanoindentation: The state of the art and future challenges, *Curr. Op. Solid St. M.* 19 (6) (2015) 354–366.
- [69] W. C. Oliver, G. M. Pharr, An improved technique for determining hardness and elastic modulus using load and displacement sensing indentation experiments, *J. Mater. Res.* 7 (6) (1992) 1564–1583.
- [70] J. Wheeler, J. Michler, Elevated temperature, nano-mechanical testing in situ in the scanning electron microscope, *Rev. Sci. Instrum.* 84 (4) (2013) 045103.
- [71] V. Maier, K. Durst, J. Mueller, B. Backes, H. W. Höppel, M. Göken, Nanoindentation strain-rate jump tests for determining the local strain-rate sensitivity in nanocrystalline Ni and ultrafine-grained Al, *J. Mater. Res.* 26 (11) (2011) 1421–1430.

How grain boundary characteristics influence plasticity close to and above the critical temperature of ultra-fine grained bcc Ta2.5W

Johann Kappacher¹, Oliver Renk², Daniel Kiener¹, Helmut Clemens¹, Verena Maier-Kiener¹

¹ *Department of Materials Science, Montanuniversität Leoben, Austria* ² *Erich Schmid Institute of Materials Science, Austrian Academy of Sciences, Leoben, Austria*

Abstract:

Dislocation-grain boundary interaction is widely accepted as the rate-controlling process for ultra-fine grained bcc metals in their high temperature deformation regime above the critical temperature. However, the influence of different types of grain boundaries remains widely unexplored so far. To this end we present here an advanced high temperature nanoindentation study on Ta2.5W specimens consisting of two distinctively different grain boundary types, but with similar submicron average spacing. While one set of samples consisted of a predominant fraction of high-angle boundaries, the second set contained mainly low-angle boundaries. Fully recrystallized samples served as a coarse grained reference batch. Using advanced nanoindentation at elevated temperatures up to 823 K, we find a temperature invariant hardness in case of the low- and a strongly pronounced temperature dependence for the high-angle grain boundary samples. This underlines the importance of grain boundary diffusivity for the predominant process of interfacial stress relaxation. Pronounced interaction of dislocations with oxygen impurity atoms was observed from 473 to 773 K for the coarse grained microstructure, yielding serrated flow as an indicator for a Portevin-Le Chatelier effect up to 573 K. Both interface types showed a significant influence to the dislocation-impurity interaction, whereby the high-angle grain boundaries suppress discrete flow characteristics.

Keywords:

nanocrystalline metals, grain-boundary structure, Portevin-Le Chatelier effect, thermally activated process, nanoindentation

1. Introduction

Over the last decade, modern technologies such as microelectronics, thin film technology or improved structural applications have led to an increased demand of materials with confined microstructure and architectures in the sub-micrometer regime. Already in the last century Hall and Petch [1, 2] found that with decreasing grain size the strength of a material can be improved. In recent years this phenomenon was intensively studied for ultra-fine grained (ufg) face-centered cubic (fcc) as well as body-centered cubic (bcc) metals [3–6]. The fundamental understanding of plasticity for conditions where interfaces govern the increasing strength of materials is hence of vital interest for academic and industrial research.

In case of dislocation controlled plastic deformation, the contribution of a single dislocation includes at least three mechanisms: nucleation, glide and storage or annihilation [7]. The slowest of these mechanisms, which usually depends on the activation energy, controls the overall plasticity and becomes the rate controlling process [8]. It is generally accepted that in a bcc lattice dislocation plasticity below the so-called knee-temperature or critical temperature, T_K , is controlled by a kink-pair mechanism [9, 10]. Above T_K screw and edge dislocations exhibit the same mobility and the materials strength becomes athermal. In this high temperature (HT) regime dislocation motion is controlled by obstacle-controlled dislocation glide such as cutting of forest dislocations, analogous to coarse grained (cg) fcc metals [11, 12].

Reducing the grain size of bcc metals to the ufg regime increases the athermal strength contribution and the strain rate sensitivity of ufg bcc metals is lower compared to their cg counterparts [4, 11, 13, 14]. This is attributed to an increased amount of long-range obstacles for dislocation motion provided by grain boundaries, while the contribution of the local Peierls barrier to the overall plasticity is reduced [13, 15, 16]. Despite these generally accepted findings, the rate controlling processes of bcc metals at the submicron scale remain intensively investigated. While several studies find that below T_K deformation is still controlled by kink-pair formation for grain sizes or single crystal sample dimensions down to ~150 nm [11, 17–19], some experiments and simulations indicate a change of the rate controlling processes and a diminishing role of screw dislocations [20–23].

Contrarily to cg bcc metals, the rate-dependence of plastic deformation increases above a certain temperature, indicating the increased contribution from

dislocation-grain boundary interaction for the dominating deformation mechanism [11, 13], in accordance with ufg fcc metals [24]. This critical temperature is around 0.2 of the melting temperature, thus the temperature regimes for thermal activation of dislocation-grain boundary interaction and kink-pair formation may partly overlap, depending on the grain size of the ufg material [13, 14]. For example, it was shown that alloying of W with Re can shift the increasing strain rate sensitivity towards higher temperatures, in accordance with the changed grain boundary diffusivity [25].

The kinetics, represented by the relaxation time τ , of these dynamic recovery processes at grain boundaries, i.e. thermally activated accommodation of lattice dislocations within grain boundaries [26] can be described as follows [27, 28]:

$$\tau = A \frac{k_B \cdot T \cdot s^3}{G \cdot \Omega \cdot D_{GB} \cdot \delta} \quad (1)$$

Apart from material constants such as the shear modulus, G , the atomic volume, Ω , and the boundary width δ ; the absolute temperature, T , and fundamental constants such as a pre-factor, A (about 1/200 for severely deformed nanostructures [27]), and the Boltzmann constant, k_B , τ solely depends on the boundary diffusivity D_{GB} and the spreading distance s , which is restricted to the grain size as an upper limit. Different types of interfaces exhibit a changed boundary diffusivity. That following, it was shown that low-angle grain boundaries provide a higher thermal stability compared to their high-angle counterparts, arising from reduced interfacial energies and diffusivities [29, 30]. Renk et al. [31] recently demonstrated that the type of interface in nanostructured fcc Ni strongly affects the temperature dependent plasticity. While for the more diffusive high-angle grain boundaries properties obey a distinct temperature dependence, low-angle grain boundaries behave rather athermal over a wide temperature range. Different to nanostructured fcc metals, no study regarding the influence of the grain boundary type on the temperature-dependent strength currently exists for bcc metals at elevated temperatures.

Since bcc refractory metals are commonly used as high temperature structural materials it is of urgent importance to understand the plastic deformation behavior above the knee-temperature, where deformation is found comparable to fcc metals. This is in particular true for high-performance nanostructures and the role of the respective interfaces. Therefore, Ta2.5W was chosen and analyzed in varying microstructural conditions. Comparing the temperature dependence of mechanical prop-

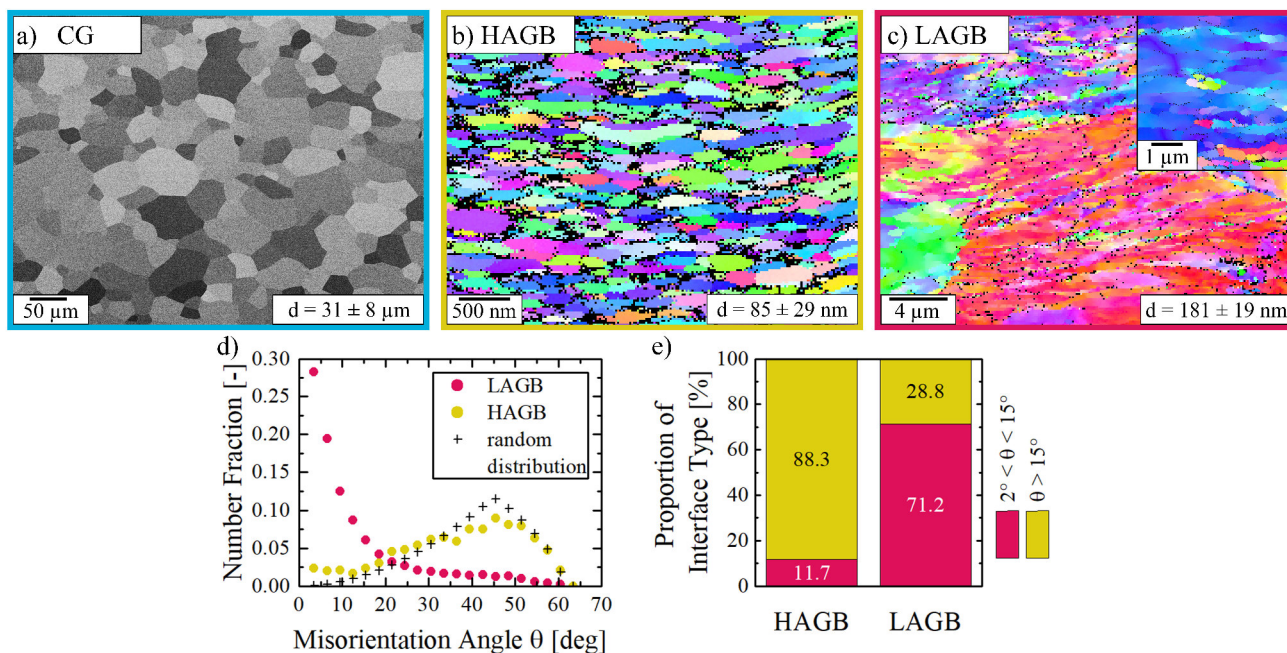


Figure 1: Microstructure of the investigated Ta2.5W samples: a) BSE image of the CG condition; b) and c) EBSD images of the HAGB and LAGB sample, respectively. The misorientation distribution of the HAGB and LAGB samples and the according boundary fractions are displayed in d) and e).

erties between a cg microstructure with ufg conditions, mainly consisting of either high-angle or low-angle grain boundaries allows for careful analysis of the influence of different interface types on plasticity in bcc metals. As Ta is known for its sensitivity to interstitial impurities [32], it is of further interest, how the different types of interface affect the interaction of dislocations with interstitials and/or grain boundaries.

2. Experimental

Technically pure Ta2.5W (all chemical compositions given in wt.%) was received from Plansee SE (Reutte, Austria). A chemical analysis for interstitial impurities revealed a concentration of $< 5 \text{ ppm C}$, $< 2 \text{ ppm H}$, as well as $19 \pm 1 \text{ ppm N}$ and $20 \pm 1 \text{ ppm O}$. The alloy Ta2.5W was selected as a model material for several reasons: due to the high melting point, T_m , of Ta, paired with a low T_K [33–35], there is a rather large temperature regime, where kink-pairs are fully thermally activated but the microstructure is still thermally stable. Due to the rather low T_K of Ta, compared *e.g.* to W, it can be rather well deformed via high pressure torsion (HPT) at room temperature, and thus microstructural saturation can be conveniently obtained [36]. Alloying with W serves to increase the thermal stability of the ufg microstructures at elevated temperatures [25]. To reach a recrystallized, cg (labeled CG) microstructure as a reference the sample was annealed for 2 h at 1773 K in a high vacuum fur-

nace (HTM Reetz GmbH, Berlin, Germany). Two ufg structures with a deliberate change of the grain boundary type, but a rather equal spacing were synthesized to elucidate the differences in the thermomechanical response, one sample mainly consisting of grain boundaries with high-angle character (*i.e.* misorientation angle $\theta > 15^\circ$) and a second one with mainly low-angle grain boundaries (*i.e.* $2^\circ < \theta < 15^\circ$), labeled as HAGB and LAGB, respectively. For the HAGB sample, discs of 8 mm diameter and 1 mm height were monotonously deformed via HPT [37] at ambient temperature for 10 rotations at a rotational speed of 0.2 rpm and a nominal pressure of 7.8 GPa. To create samples with LAGBs and an interface spacing in the sub-micrometer range cyclic high pressure torsion (CHPT) [38, 39] was applied. Therefore, recrystallized Ta2.5W samples (1773 K, 2 h) with 10 mm diameter and 1 mm height were cyclically deformed at a 5° twist angle for five cycles. The rotational speed was again 0.2 rpm and the applied nominal pressure 5.1 GPa.

In order to ensure microstructural stability, *i.e.* to anticipate recovery or slight grain growth in case of the HAGB sample, annealing for 2 h at 773 K was conducted in vacuum prior to mechanical testing. Microstructural investigations were performed in radial direction (RD) of the discs at a radius of 3 mm. The LAGB sample was microstructurally investigated in tangential direction (TD) of the sample and the chosen radius for further experi-

ments was 4.5 mm.

For microstructural characterization as well as nanoindentation experiments the samples were carefully mechanically ground and polished. To remove any remaining deformation layer a final chemical polishing step was carried out with a 1:1 mixture of OP-S (Struers GmbH, Willich, Germany) and 5 % KOH in H₂O. To reveal the microstructure of the CG sample back-scattered electron (BSE) images were taken on a Tescan Clara scanning electron microscope (SEM) (Tescan, Brno, Czech Republic) at 15 kV and the grain size was determined by means of line-intersection method. For the samples with submicron sized grains, microstructural imaging was received by an electron back-scatter diffraction (EBSD) setup from Bruker Nano GmbH (Berlin, Germany) equipped in a LEO 1525 field emission SEM (Carl Zeiss Microscopy GmbH, Jena, Germany) at 20 kV. Misorientation angles between adjacent grains were analyzed using the standard software package OIM analysis 7 from EDAX Inc. (Mahwah, NJ).

To investigate the mechanical properties, high temperature nanoindentation experiments were performed on an InSEM-HT nanoindenter from Nanomechanics Inc., KLA (Oak Ridge, TN) in axial direction (AD) of the samples. The system is equipped with a continuous stiffness measurement unit, superimposing a sinusoidal force signal with 100 Hz and a displacement amplitude of 2 nm to determine the contact stiffness continuously over indentation depth. For the CG and HAGB samples a WC, while for the LAGB sample a SiC Berkovich tip (both Synton MDP, Nidau, Switzerland) were used. The nanoindenter is installed in a Tescan Vega3 SEM (Tescan, Brno, Czech Republic) under high vacuum conditions ($< 10^{-4}$ mbar), allowing precise indent positioning as well as preventing high temperature oxidation of tip and sample. A tip temperature calibration was carried out by direct indentation into a thermocouple, as reported by Wheeler and Michler [40]. Area function and frame stiffness were obtained by room temperature (RT) indentation of fused quartz according to the analysis of Oliver and Pharr [41]. To follow any possible degradation of the tip after every sample testing series, additional indentations on fused quartz were performed at RT.

In order to obtain hardness, H , and Young's modulus, E , constant indentation strain rate experiments [42] were performed at $\dot{P}/P = 0.1 \text{ s}^{-1}$. The obtained values are averaged at an indentation depth of 700 to 800 nm for the CG sample and, due to the higher hardness and hence lower maximum indentation depth between 400

and 500 nm for LAGB and HAGB samples. Additional nanoindentation strain rate jump tests, as introduced by Maier *et al.* [43], with an abrupt change in strain rate by an order of magnitude to $\dot{P}/P = 0.01 \text{ s}^{-1}$ for at least 100 nm and finally switching back to $\dot{P}/P = 0.1 \text{ s}^{-1}$, were executed. At least ten valid indentation experiments were performed for every sample, temperature and test protocol. From the instantaneous hardness response [16] in respect to the changed indentation strain rate, the strain rate sensitivity, m , and the apparent activation volume, V^* , can be calculated according to Eqs. 2 and 3:

$$m = \frac{\partial(\ln(H))}{\partial(\ln(\dot{\epsilon}))} \quad (2)$$

$$V^* = \frac{C^* \cdot \sqrt{3} \cdot k_B \cdot T}{m \cdot H} \quad (3)$$

with C^* being a constraint factor of 2.8. V^* is commonly normalized to the cubed Burgers vector, b^3 , to facilitate comparison between different materials.

3. Results

3.1. Microstructure

In Fig. 1 the microstructure of the three investigated Ta2.5W samples, including statistical evaluation of the grain boundary characteristics, are presented. A BSE image of the recrystallized CG sample reveals globular equiaxed grains with an average diameter of $31 \pm 8 \mu\text{m}$ (Fig. 1a). Due to the large grain size compared to the maximum indentation depth of 900 nm, deformation is mainly governed by single crystalline behavior with diminishing influence of any sort of interfaces. The inverse pole figure maps obtained by EBSD of the HAGB sample (Fig. 1b) exhibit typical HPT-deformed grains with an elongation in TD. The decisive grain diameter (small dimension) in AD was determined by the line-intersection method to be $85 \pm 29 \text{ nm}$, with the majority of grain boundaries being of high-angle character (*i.e.* $\theta > 15^\circ$, Fig. 1e). The distribution of the misorientation angle (Fig. 1d) was found to be close to the random distribution. In Fig. 1c an overview of the microstructure of the LAGB sample is presented including an inset taken at higher magnification. Due to the CHPT deformation the subgrains are again elongated, with an average resolved cell size of $181 \pm 19 \text{ nm}$ in the small dimension. At the chosen radius of 4.5 mm the proportion of LAGBs ($2^\circ < \theta < 15^\circ$, Fig. 1e) was more than 70 %, which is also evident from the misorientation distribution in Fig. 1d.

3.2. Constant indentation strain rate experiments

The measured hardness over testing temperature for the three different samples is illustrated in Figs. 2a-c. The RT hardness values are 6.28 ± 0.02 , 4.63 ± 0.14 and 2.81 ± 0.07 GPa for the HAGB, LAGB and CG samples, respectively. The differences can be directly linked to an increased strength due to grain refinement. The observed evolution of hardness over temperature is significantly dependent on the different microstructures. The HAGB sample (Fig. 2a) revealed a continuous decrease of hardness to 5.38 ± 0.08 GPa up to 523 K. Between 573 and 723 K an increased hardness compared to the monotonous decrease can be observed with a peak of 5.89 ± 0.04 GPa at 623 K. At the maximum testing temperature of 823 K the hardness was 4.46 ± 0.08 GPa, while the RT hardness after this testing sequence was with 5.79 ± 0.04 GPa lower than the as-prepared state, indicating thermally induced grain growth.

In contrast to the pronounced temperature sensitivity of the HAGB sample, probing LAGBs (Fig. 2b) revealed a temperature invariant hardness up to 473 K. An increased hardness compared to the general trend can again be observed between 523 and 623 K, with a peak of 5.05 ± 0.18 GPa. At 773 K a hardness of 3.57 ± 0.11 GPa was detected, while after the maximum testing temperature the RT hardness (4.74 ± 0.10 GPa) slightly increased, although within standard deviation. The slightly higher scatter in the LAGB data, represented by a higher standard deviation of the measured values compared to the HAGB or CG sample can be assumed as a result of the less homogenized microstructure when compared to the cg behavior or the saturated grain size of the HAGB samples, as the size and shape of the developed dislocation boundaries depends on the crystallographic grain orientation.

The CG sample in Fig. 2c exhibits a strong temperature dependence of hardness up to 373 K ($0.11 T_m$). A further increase of the testing temperature results in an athermal hardness response (2.49 ± 0.07 GPa) up to 423 K. Between 473 and 723 K an increased hardness can be observed, with a peak of 2.65 ± 0.07 GPa at 623 K. At 823 K a value of 2.05 ± 0.05 GPa was measured, while the hardness after HT testing was found unchanged (2.83 ± 0.07 GPa).

In Fig. 2d the observed Young's modulus over temperature is presented along with additional literature values [44]. From the RT values of 180.4 ± 1.9 , 186.2 ± 3.9 and 180.9 ± 4.1 GPa for the HAGB, LAGB and CG sample, respectively, a monotonous decrease can be observed over the whole testing temperature range. The LAGB sample exhibits steadily higher values compared

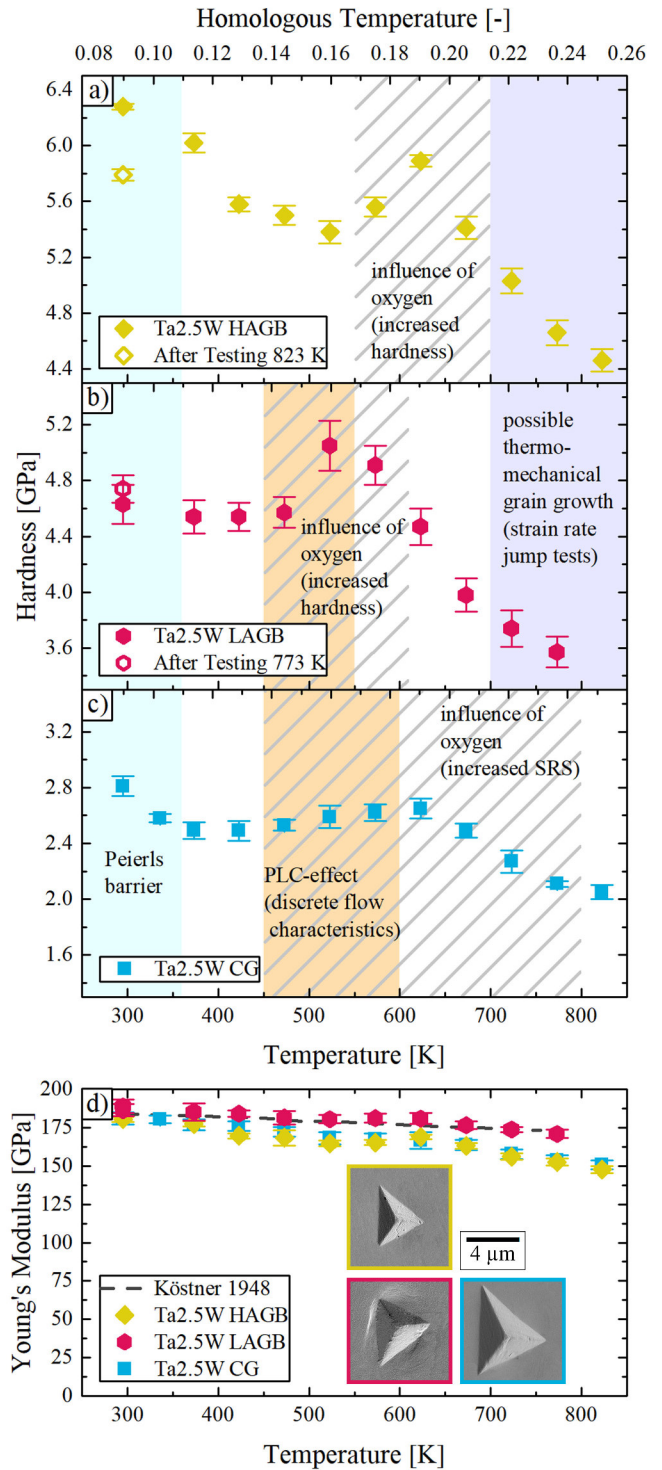


Figure 2: Evolution of hardness over temperature for the three different microstructures: a) HAGB, b) LAGB and c) CG. In d) the measured Young's modulus is plotted over temperature in addition to literature values [44]. The insets show residual indents at RT (see text).

to the CG or HAGB samples. A slightly increased pile-up behavior, as illustrated in the inset in Fig. 2d for remaining indents at RT was observed for the LAGB sample. While the impressions in the CG and HAGB sam-

ples were almost perfect triangles, the remaining indents on the LAGB sample reveal a convex deviation from the ideal indent shape. Observing the impressions of different testing temperatures did not reveal a significant change in the pile-up behavior with temperature.

During the loading sequence of constant indentation strain rate experiments discrete flow characteristics could be observed in the CG sample from 473 to 573 K. Due to the intrinsically load controlled nature of the InSEM-HT system this behavior manifests as regular bursts in indentation depth and consequently drops in hardness, as shown in Fig. 3a. Such a behavior is typically associated with the Portevin-Le Chatelier (PLC) effect as a result of dislocations interacting with solute atoms. Although the effect is well described for macroscopic deformation experiments, detailed analyses via nanoindentation focused mainly on Al alloys so far [45–48]. Comparing the appearance of the hardness over indentation depth (Fig. 3a) for different temperatures indicate a strong temperature dependence of this mechanism. While for 473 and 523 K it is regular and periodic over the whole indentation depth, at 573 K the hardness drops occurred less regular at random indentation depth. The effect is qualitatively most pronounced at 523 K, showing the most prominent and rapid hardness drops. While non such behavior could be observed at any temperature for the HAGB sample (Fig. 3c), the LAGB sample showed a slightly periodically curvy flow at 523 K (Fig. 3b). Additionally, during the low indentation strain rate of $\dot{P}/P = 0.01 \text{ s}^{-1}$ in the strain-rate jump tests, serrated flow could also be observed at 473 K. The events are, however, less pronounced compared to the CG material. For a better illustration, the temperatures where a PLC effect was observed are highlighted in orange in Figs. 2 and 3.

3.3. Nanoindentation strain rate jump tests

The results of the strain rate jump tests, strain rate sensitivity and apparent activation volume are plotted in Fig. 4 over temperature. At RT m -values of 0.014 ± 0.001 , 0.009 ± 0.001 and 0.010 ± 0.001 for the CG, HAGB and LAGB sample, respectively, were determined. For the CG sample towards T_K , the strain rate sensitivity decreases to 0.004 ± 0.001 with increasing temperature at 373 K (around $0.11 T_m$). As the testing temperature further increases a negative strain rate sensitivity can be observed (473 and 523 K), followed by a strongly rate sensitive strength regime between 623 and 773 K. At 823 K hardness is again almost strain rate independent with $m = 0.002 \pm 0.001$. In the HAGB sample m remains constant at 0.008 ± 0.001 up to 523 K, followed by a steady increase as temperature rises up to the maximum

testing temperature, where values of 0.040 ± 0.006 were measured. The strain rate sensitivity of the LAGB sample continuously decreases to 0.003 ± 0.001 at 423 K, with a negative strain rate sensitivity at 473 K and constant values from 573 to 773 K between 0.014 and 0.019. After the maximum testing temperature, the HAGB sample reveals a slightly reduced strain rate sensitivity of 0.006 ± 0.001 at RT, while the values for the LAGB and CG samples remained the same within the standard deviation.

The corresponding activation volume, as an indicator for the volume collectively involved in the rate controlling deformation mechanism [49], was found to be very similar at RT (21 ± 3 , 16 ± 2 and $20 \pm 3b^3$ for CG, HAGB and LAGB, respectively). Note that no activation volumes were calculated for temperatures where negative strain rate sensitivities were measured. The activation volume in the CG sample shows the strongest increase with temperature, reaching values of more than $100b^3$ at 373 K. Additionally, between 623 and 773 K lower values between 30 and $80b^3$ were observed. The HAGB sample exhibits the lowest increase with temperature, peaking at 523 K ($35 \pm 6b^3$), followed by a continuous decrease towards 823 K, where a value of $15 \pm 3b^3$ was measured. The LAGB sample follows the trend of an increasing activation volume between RT and 423 K ($107b^3$). Above 523 K values between 20 and $60b^3$ were determined. After high temperature nanoindentation the CG and LAGB samples exhibit an unchanged activation volume at RT, while for the HAGB sample a slight increase towards $25 \pm 5b^3$ was observed.

In Fig. 5 the evolution of hardness over indentation depth for representative strain rate jump tests are shown for the CG (a), LAGB (b) and HAGB (c) samples at different temperatures. While the change in strain rate by an order of magnitude develops in an instantaneous change in hardness for most of the presented curves, testing the HAGB sample at 723 K and higher temperatures results in a more transient behavior. Also the hardness after the change in strain rate back to the original value does not reach the same plateau as before the first jump. This is also true for the LAGB sample tested at 723 and 773 K. The change in strain rate also has a remarkable influence on the discrete flow characteristic caused by the PLC effect. In the CG sample, where such a behavior was observed during constant strain rate experiments from 473 to 573 K, the reduced strain rate results in a more pronounced serrated flow at 473 K, while at 523 and 573 K the hardness drops diminish. A similar behavior can be observed for the LAGB sample, where serrated flow is evident for low strain rates at 473 K, but not

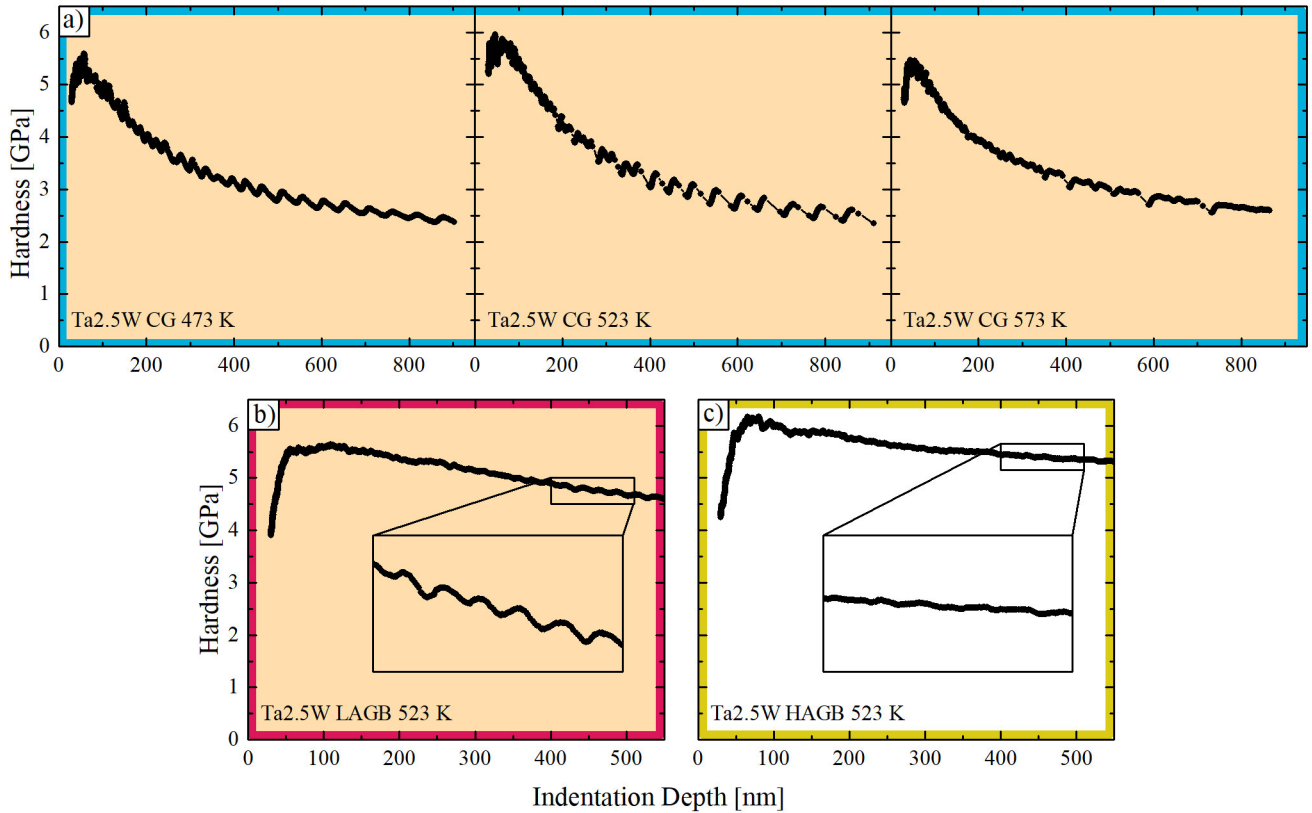


Figure 3: Hardness over indentation depth for selected temperatures to illustrate the discrete flow characteristics of the PLC effect in a) the CG condition. For the ufg samples consisting mainly of b) LAGBs a slightly wavy flow can be observed at 523 K, while such a behavior could not be detected for the c) HAGB sample.

at the standard strain rate of $\dot{P}/P = 0.1 \text{ s}^{-1}$. The performance reverses again at 523 K, where a wavy hardness over indentation depth can be observed for 0.1 s^{-1} , while a smooth flow characteristic is visible for 0.01 s^{-1} .

4. Discussion

Upon comparing the plastic deformation behavior as a function of temperature between the cg microstructure, sampling a minor contribution from interfaces, with samples where the probed volume consists mainly of either high- or low-angle grain boundaries, it is evident that the type of grain boundary has a significant impact on the deformation behavior. Notably, the well matching Young's modulus over temperature and its accordance with literature [44] confirms the validity of our data. Slightly increased modulus values in case of the LAGB sample are most probably related to the different indenter materials used, as a varying temperature dependence of the Young's modulus of the tip material as well as general inaccuracies of the values at RT can cause significant errors in the measured Young's modulus of the investigated material [50][44]. The higher values could also be influenced by the observed slight pile-up behav-

ior in case of the LAGB sample, resulting in a overestimation of hardness as well as elastic modulus [51].

4.1. Dislocation – solute atom interaction

The mechanical properties of bcc metals in general and the reactive Ta in particular, are sensitive to interstitial impurities such as O, N or C [32]. Internal friction experiments on Ta reveal a Snoek peak between 500 and 750 K [52, 53], which was related to migration of O atoms leading to partial pinning of dislocations [54, 55]. Such local atomic jumps can not only impede the movement of dislocations but also affect the stress relaxation by defect induced distortion [56]. In the temperature regime of the impurity-induced relaxation peak the hardness of the CG sample shows an anomalous increase with temperature (Fig. 2c) and an increased strain rate sensitivity (Fig. 4). Similar observations were made in macroscopic tensile tests where an increased flow stress was observed between 600 and 800 K for technically pure Ta2.5W with 53 ppm O [57]. Pink [58] reported an increased flow stress of Ta with 6 ppm O at 10 % strain between 573 and 773 K. He further outlined, that a single impurity species may hinder the dislocation motion and hence increase the flow stress in two

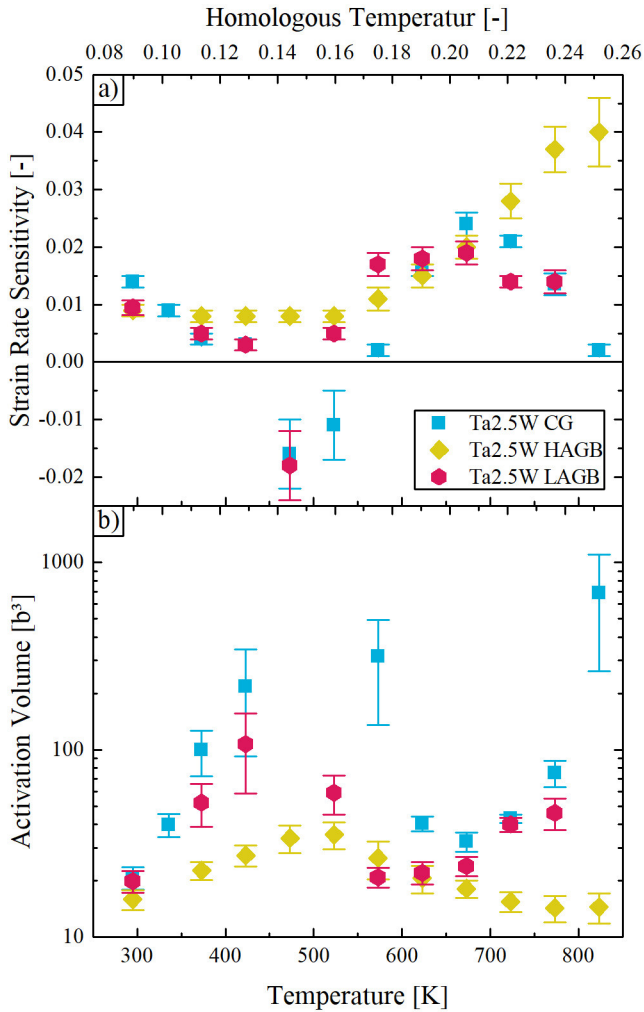


Figure 4: Results of the strain rate jump tests: a) strain rate sensitivity and b) activation volume over temperature. In case of a negative strain rate sensitivity no activation volume was calculated.

different ways: Either by forming Cottrell clouds or by a strain-induced ordering process related to the Snoek-effect. The rate-controlling step of the two mechanisms is different, hence they may occur at different temperature intervals. The former effect is, however, responsible for a serrated flow characteristic, as reported in [59] between 473 and 573 K. This strongly suggests that the uncommon increase of hardness with temperature is a result of thermally activated dislocation-impurity interactions.

It is generally accepted that the serrated flow behavior of the PLC effect originates from dynamic strain aging, *i.e.* thermally activated release of solute-decorated mobile dislocations, in conjunction with solute aging of forest dislocations [60, 61]. In a certain temperature and strain rate range, mobile dislocations that are temporarily pinned by forest dislocations become occupied with sufficiently mobile solutes. A negative strain rate

sensitivity can thus be observed, as the stress required to detach the solute-decorated dislocation is higher than keeping the dislocation in motion upon their release [62]. Hence, diffusion of the responsible solute atoms has to be high enough to age the pinned dislocations. Using a diffusion pre-factor, D_0 ($0.0044 \text{ cm}^2 \text{ s}^{-1}$), and an activation energy for diffusion, E_A , of $106.483 \text{ kJ mol}^{-1}$ [63, 64][57,58], the calculated diffusion coefficient for O in Ta is $1.02 \times 10^{-17} \text{ m}^2 \text{ s}^{-1}$ at 523 K. Other impurities, such as N or C have a several magnitudes lower diffusion coefficient [64, 65][58,59]. For the substitutional alloying element W, the diffusion coefficient can only be extrapolated from experiments performed at much higher temperatures, however, this results in a value in the order of $10^{-39} \text{ m}^2 \text{ s}^{-1}$ at 523 K [66]. Estimating a diffusion path for O interstitials in Ta through $x = 2 \cdot \sqrt{Dt}$ for 1 s gives a value of 6 nm. This is well within the range of the deformation rate applied in the nanoindentation experiments, which increases linearly with displacement up to around 40 nm s^{-1} at an indentation depth of 800 nm. Hence it can be argued that the interaction of O impurity atoms with dislocation cause a PLC-like behavior in the CG Ta2.5W alloy.

Interestingly, the influence of O in case of the ufg microstructure manifests different. Generalization of the influence of grain boundaries on the PLC behavior is difficult, as it is dependent on microstructure and (local) chemical composition, which, in case of the microstructure, strongly depends on material processing [47]. In Al-Mg alloys it was shown, that for AA5182 HPT deformation leads to a smooth load-displacement behavior during nanoindentation, while the same material exhibits serrated flow in the recrystallized condition [67]. Contrarily, ufg AA5754 shows pronounced discrete flow characteristics at low strain rates [68]. In the present study no PLC-effect could be observed in case of the ufg HAGB sample, while in case of the LAGB sample a PLC effect is evident at 473 and 523 K, although less pronounced compared to the CG microstructural condition. As the drops in hardness require collective motion of dislocation avalanches [69], HAGBs may act as barriers, suppressing a serrated flow. It could be argued that in case of LAGBs the effect is attenuated, but slip transfer between adjacent subcells is still possible, resulting in the observed periodically curvy flow.

While the HAGB sample exhibits a peak hardness at the same temperature as the CG specimen (623 K), the temperature regime where hardness is obviously influenced by solute atoms is narrowed between 573 and 673 K. An increasing strain rate sensitivity with temperature is evident starting at 573 K, however, such a

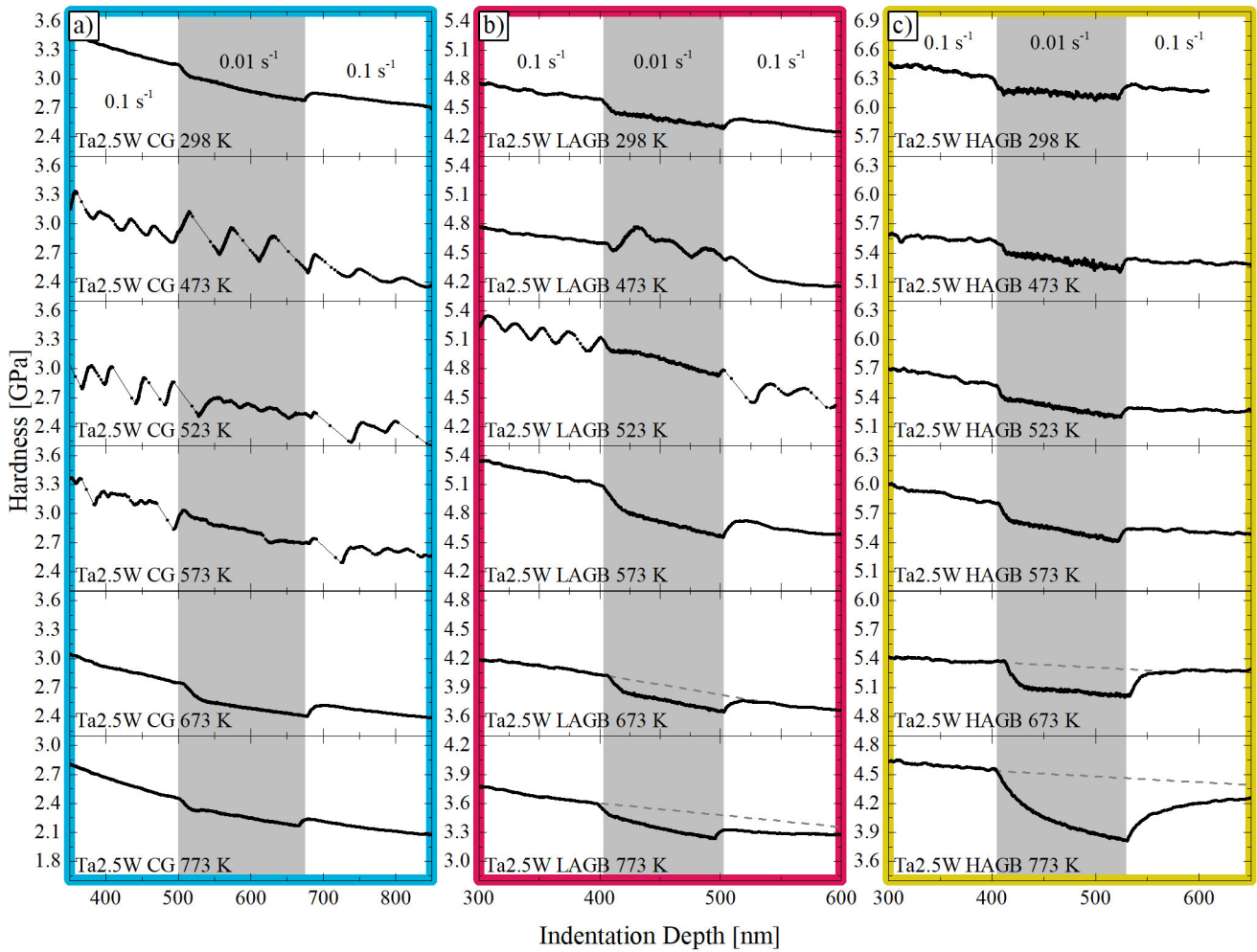


Figure 5: Magnification of the hardness response due to a change in strain rate during the strain rate jump tests for a) CG, b) LAGB and c) HAGB samples at selected temperatures.

behavior is typical for ufg bcc metals above a critical temperature [11, 13, 25], indicating a thermally activated facilitation of dislocation-grain boundary interaction through diffusion processes. It can be assumed that an increased strain rate sensitivity caused by the thermally activated accommodation of lattice dislocations within grain boundaries overlaps with the dislocation-impurity interaction and hence no clear distinction between the two effects on the strain rate sensitivity can be made. Generally, the interaction of dislocations with impurities strongly depends on the diffusivity of the solute atoms, which in turn is enhanced through interfaces such as grain boundaries, resulting in different temperatures where impurity effects occur. Another plausible explanation would be, that in the ufg microstructure impurity atoms preferably segregate towards grain boundaries, as even reported for other cg refractory metals [70, 71]. That way, the impurity concentration within the grain changes, and thus the influence of O would be dimin-

ished.

4.2. Microstructural thermo-mechanical stability and considerations regarding impurity enrichment

The large fraction of grain boundaries makes ufg microstructures prone to grain growth already at comparably low homologous temperatures. Annealing the HAGB sample prior to HT nanoindentation at 773 K for 2 h ensures thermal stability up to this temperature. Probing the sample at the maximum testing temperature of 823 K, however, results in grain growth, as can be derived from the reduced RT hardness (Fig. 2a) determined subsequently to the maximum testing temperature. The RT hardness of the LAGB sample after testing at the maximum temperature of 773 K demonstrates that measurements are conducted within the thermal stability limit of the microstructure.

However, grain boundary migration and hence grain coarsening can occur facilitated through applied stresses

[72–74]. Thereby, grain growth can take place in the plastic deformation zone underneath the indenter even below the thermal stability limit [31, 75]. A necessary indicator for such a behavior can be derived from the hardness response over indentation depth during strain rate jump tests (Fig. 5). For a thermo-mechanically stable microstructure, the jump back to the initial strain rate should result in the same hardness level. If this is not the case, as indicated with grey lines in Fig. 5 for both HAGB and LAGB samples above 723 K, the microstructure underneath the indenter is prone to grain growth, explaining the observed reduced hardness above this temperature [31].

As discussed above, O has a strong influence on the deformation behavior of Ta2.5W at elevated temperatures. Hence, the question to be addressed is whether the 20 ppm of O derived from chemical analyses are sufficient to cause the observed effects, or if impurities were taken up during high temperature testing. For enrichment of O within Ta2.5W two different steps need to be fulfilled: adsorption of residual gas within the vacuum chamber and diffusion of the solved atoms towards a sufficient distance from the surface. Diffusion from the surface can be estimated from Eq. 4 [76]:

$$c(x) = c_R \cdot \operatorname{erfc} \left(\frac{x}{2\sqrt{Dt}} \right) \quad (4)$$

Here, $c(x)$ represents the concentration of a diffusing species at a distance x from the surface, c_R is the constant concentration at the surface, D is the diffusion coefficient at a certain temperature and t the time. Considering D of O in Ta at the maximum testing temperature of 823 K ($7.67 \times 10^{-14} \text{ m}^2 \text{ s}^{-1}$ [64]) and an average measurement time of 3 h, an increase in the O content up to around 9 % of the surface concentration $c(x)/c_R$ can be assumed at a distance of 800 nm from the surface. Thus, from a diffusion perspective an enrichment of O in the material is conceivable. Cowgill and Stringer [77] investigated the surface contamination of Ta with O for a variety of temperatures and pressures considering a Langmuir isotherm and reported a surface coverage of 20 % at 823 K for a pressure of 67 mbar. It is further described that the surface coverage is linearly related to the applied pressure in case of a low pressure regime. Since in the current study the experiments were executed in vacuum below 10^{-4} mbar, almost six orders of magnitude lower compared to the investigations in [77], the O surface coverage of Ta can be assumed as negligible. Thus, the observed dislocation-oxygen interaction can be solely related to the initial O content in the material, also supported by the unchanged hardness of the

CG sample after testing at 823 K.

4.3. Regarding the rate-controlling deformation mechanisms

The temperature dependence of hardness in case of the CG sample (Fig. 2c) as well as the decreasing strain rate sensitivity and accordingly increasing activation volume indicate kink-pair formation as the rate controlling deformation mechanism below $0.11 T_m$ [9, 10]. Above 373 K hardness remains athermal, while the rate sensitivity is 0.003. An increasing activation volume with temperature can be interpreted with larger spreading of the kink-pairs due to thermal activation [13] while $100b^3$ at 373 K indicate a changing deformation mechanism towards dislocation-dislocation interaction [78]. It is worth noting that the low activation volumes between 623 and 773 K represent the strong influence of diffusion processes on the deformation behavior as described above. The homologous temperature of around $0.11 T_m$ for thermal activation of the kink-pairs in Ta2.5W is relatively low compared to other bcc metals, where T_K is reached around $0.20 T_m$ [11, 79]. This is in line with a double-kink formation energy, reported to be 0.74 eV in case of Ta, what is less than half the value of W (1.60 eV) [80]. A similarly low transition temperature was further experimentally confirmed by several authors [33, 34, 57]. The reduced hardness at 823 K compared to 423 K, where deformation is controlled by cutting of forest dislocation and the yield stress should be temperature independent, can be explained by dynamic dislocation interaction during indentation. Nanoindentation with a Berkovich indenter applies a representative strain of 7.16 % [81]. Hence, for materials with a strong work hardening tendency, a significant contribution to the measured hardness values will originate from strain hardening [82]. As the testing temperature increases, the work hardening rate may decrease and thus the measured hardness value would be reduced although the yield point could remain the same. The work-hardening behavior of recrystallized Ta2.5W as derived from compression tests on macroscopic samples decreases significantly at these high temperatures, while the yield stress remains constant [59]. Hence, dynamic recovery is enhanced at 823 K, represented by decreasing hardness values.

The difference in the temperature- and strain rate-dependence of hardness in case of the HAGB and LAGB sample is striking. Below testing temperatures where an influence of O is evident, the HAGB sample exhibits a strong temperature dependence with a hardness decrease of around 0.9 GPa up to 523 K, whereas the LAGB sample behaves almost perfectly athermal. The microstruc-

ture is thermally stable in this temperature regime; hence this behavior can be solely related to the influence of the grain boundary character to the deformation mechanism. Notably, a kink-pair controlled deformation regime in case of the ufg microstructures could not be clearly identified from the hardness or flow stress over temperature. The results of the strain rate jump tests reveal a comparable behavior between the CG and LAGB sample, while the strain rate sensitivity in case of the HAGB sample is unaffected between RT and 373 K. However, due to the lack of sufficient data points below T_K the question regarding the dominating processes for the ufg samples in this deformation regime will not be addressed in this manuscript. Thus, the following discussion refers to temperatures exceeding 373 K. The activation volume of several $10b^3$ indicates dislocation-grain boundary interaction as the rate controlling step [11], *i.e.* plastic deformation is controlled by dynamic recovery processes at grain boundaries and grain boundary diffusion [24, 26]. As described by Eq. 1 the relaxation time for these processes scale inversely with the grain boundary diffusivity. While no grain boundary diffusion data that distinguishes between LAGB and HAGB is available for Ta, diffusivity along grain boundaries in general is strongly dependent on the misorientation angle of the two adjacent grains [83–85]. For fcc Ni, where interfacial diffusivity is well investigated, the grain boundary diffusion coefficient in case of LAGBs is at least two orders of magnitude lower [30, 31] and a similar trend can be assumed for Ta. Consequently, the reduced relaxation time in case of HAGBs results in an increased thermal activation of dislocation-grain boundary interaction, reflected by the stronger temperature- and rate dependence of flow stress [31]. The increasing strain rate sensitivity above 573 K for both ufg samples indicates that the mechanism is thermally facilitated above this temperature. As dislocation-grain boundary interaction is a thermally activated process, part of the energy barrier can be overcome by mechanical work, see Eq. 5 [86]:

$$\Delta F^* = \Delta G^* + \tau^* \cdot V^* \quad (5)$$

Here, ΔF^* is the Helmholtz free energy to overcome the energy barrier, consisting of a thermal contribution, represented by the Gibbs free energy ΔG^* and an equivalent mechanical work $\tau^* \cdot V^*$, where τ^* is the resolved shear stress. While Eq. 1 only considers the thermal contribution to the relaxation time, the applied high shear stresses during nanoindentation of the ufg structures allow to surmount the activation energy for dislocation-grain boundary interaction below temperatures where the process is facilitated by thermal activa-

tion only [24, 31]. This is in line with the difference in temperature dependent hardness in case of samples consisting mainly of HAGBs and LAGBs even below the critical temperature.

The results of the present study underline the importance of interfacial stress relaxation in the high temperature deformation regime of ultra-fine grained bcc metals. Comparison with nanostructured fcc metals of different interface types [31] further confirmed that the rate-controlling deformation process is common for nanostructured metals of both crystal structures, namely accommodation of lattice dislocations within grain boundaries.

5. Conclusions

High temperature nanoindentation was conducted on Ta2.5W in the recrystallized as well as severely deformed condition, with these samples consisting mainly of high- and low-angle grain boundaries, respectively. The goal of this research was to clarify how interfacial stress relaxation is affected by the grain boundary type in bcc metals in the high temperature deformation regime. From a comparison of the temperature- and strain rate-sensitivity of hardness the following conclusions can be drawn:

- The differences in the behavior of HAGB and LAGB emphasizes the importance of interfacial stress relaxation and its dependence on boundary diffusivity. Our results strongly suggest that the high temperature deformation behavior in ufg bcc metals above the knee-temperature is controlled by accommodation of lattice dislocations within grain boundaries, a process that occurs mechanically driven at low homologous temperatures and accelerates by thermal activation above a certain critical temperature. Thus, the temperature- and rate dependence of hardness is strongly pronounced in samples consisting mainly of HAGB, while LAGB perform rather athermal and thus a lower strain rate sensitivity is evidenced.
- Between 473 and 772 K the flow stress of Ta2.5W is strongly affected by small amounts (20 ppm) of O dissolved in the crystal. From 473 to 573 K a Portevin-Le Chatelier effect with serrated flow characteristics is evident, while at higher temperatures the effect manifests in an increased hardness and strain rate sensitivity.
- The grain size and boundary character in the lower end of the ultra-fine grained scale have a significant

impact on the dislocation-interstitial interaction, resulting in a shift of the temperature, for which the flow stress is affected and suppression of discrete yielding in case of HAGBs.

Acknowledgments

The authors want to thank Plansee SE for providing the material. D.K. acknowledges funding by the European Research Council under Grant number 771146 (TOUGHIT). O.R. acknowledges funding from the Austrian Academy of Sciences via Innovation Fund IF 2019-37.

References

- [1] E. Hall, The deformation and ageing of mild steel: III discussion of results, *Proc. Phys. Soc. B* 64 (9) (1951) 747.
- [2] N. Petch, The cleavage strength of polycrystals, *J. Iron Steel I.* 174 (1953) 25–28.
- [3] R. Fritz, V. Maier-Kiener, D. Lutz, D. Kiener, Interplay between sample size and grain size: single crystalline vs. ultrafine-grained chromium micropillars, *Mater. Sci. Eng. A* 674 (2016) 626–633.
- [4] D. Wu, X. Wang, T. Nieh, Variation of strain rate sensitivity with grain size in Cr and other body-centred cubic metals, *J. Phys. D Appl. Phys.* 47 (17) (2014) 175303.
- [5] J. May, H. W. Höppel, M. Göken, Strain rate sensitivity of ultrafine grained fcc-and bcc-type metals, in: *Mater. Sci. Forum*, Vol. 503, Trans Tech Publ, 2006, pp. 781–786.
- [6] Q. Wei, S. Cheng, K. Ramesh, E. Ma, Effect of nanocrystalline and ultrafine grain sizes on the strain rate sensitivity and activation volume: fcc versus bcc metals, *Mater. Sci. Eng. A* 381 (1-2) (2004) 71–79.
- [7] D. Caillard, J.-L. Martin, *Thermally activated mechanisms in crystal plasticity*, Pergamon Materials Series, 2003.
- [8] J. W. Christian, *The theory of transformations in metals and alloys*, Newnes, 2002.
- [9] B. Sestak, A. Seeger, *Gleitung und Verfestigung in kubisch-raumzentrierten Metallen und Legierungen*, *Z. Metallkd.* 69 (4) (1978) 195–202.
- [10] A. Seeger, The temperature and strain-rate dependence of the flow stress of body-centred cubic metals: A theory based on kink-kink interactions, *Z. Metallkd.* 72 (6) (1981) 369–380.
- [11] D. Kiener, R. Fritz, M. Alfreider, A. Leitner, R. Pippan, V. Maier-Kiener, Rate limiting deformation mechanisms of bcc metals in confined volumes, *Acta Mater.* 166 (2019) 687–701.
- [12] J. Kappacher, A. Leitner, D. Kiener, H. Clemens, V. Maier-Kiener, Thermally activated deformation mechanisms and solid solution softening in W-Re alloys investigated via high temperature nanoindentation, *Mater. Des.* 189 (2020) 108499.
- [13] V. Maier, A. Hohenwarter, R. Pippan, D. Kiener, Thermally activated deformation processes in body-centered cubic Cr–how microstructure influences strain-rate sensitivity, *Scripta Mater.* 106 (2015) 42–45.
- [14] R. Fritz, D. Wimler, A. Leitner, V. Maier-Kiener, D. Kiener, Dominating deformation mechanisms in ultrafine-grained chromium across length scales and temperatures, *Acta Mater.* 140 (2017) 176–187.
- [15] Q. Wei, H. Zhang, B. Schuster, K. Ramesh, R. Valiev, L. Kecskes, R. Dowding, L. Magness, K. Cho, Microstructure and mechanical properties of super-strong nanocrystalline tungsten processed by high-pressure torsion, *Acta Mater.* 54 (15) (2006) 4079–4089.
- [16] V. Maier, C. Schunk, M. Göken, K. Durst, Microstructure-dependent deformation behaviour of bcc-metals–indentation size effect and strain rate sensitivity, *Philos. Mag.* 95 (16-18) (2015) 1766–1779.
- [17] C. Bonnekoh, J. Reiser, A. Hartmaier, S. Bonk, A. Hoffmann, M. Rieth, The brittle-to-ductile transition in cold-rolled tungsten sheets: the rate-limiting mechanism of plasticity controlling the BDT in ultrafine-grained tungsten, *J. Mater. Sci.* 55 (2020) 12314–12337.
- [18] A. Schneider, D. Kaufmann, B. Clark, C. Frick, P. Gruber, R. Mönig, O. Kraft, E. Arzt, Correlation between critical temperature and strength of small-scale bcc pillars, *Phys. Rev. Lett.* 103 (10) (2009) 105501.
- [19] O. T. Abad, J. M. Wheeler, J. Michler, A. S. Schneider, E. Arzt, Temperature-dependent size effects on the strength of Ta and W micropillars, *Acta Mater.* 103 (2016) 483–494.
- [20] G. Cheng, W. Jian, W. Xu, H. Yuan, P. Millett, Y. Zhu, Grain size effect on deformation mechanisms of nanocrystalline bcc metals, *Mater. Res. Lett.* 1 (1) (2013) 26–31.
- [21] Y. Cui, G. Po, N. Ghoniem, Temperature insensitivity of the flow stress in body-centered cubic micropillar crystals, *Acta Mater.* 108 (2016) 128–137.
- [22] H. Yilmaz, C. J. Williams, J. Risan, B. Derby, The size dependent strength of Fe, Nb and V micropillars at room and low temperature, *Materialia* 7 (2019) 100424.
- [23] P. Srivastava, K. Jiang, Y. Cui, E. Olivera, N. Ghoniem, V. Gupta, The influence of nano/micro sample size on the strain-rate sensitivity of plastic flow in tungsten, *Int. J. Plast.* 136 (2021) 102854.
- [24] O. Renk, V. Maier-Kiener, I. Issa, J. Li, D. Kiener, R. Pippan, Anneal hardening and elevated temperature strain rate sensitivity of nanostructured metals: their relation to intergranular dislocation accommodation, *Acta Mater.* 165 (2019) 409–419.
- [25] J. Kappacher, O. Renk, D. Kiener, H. Clemens, V. Maier-Kiener, Controlling the high temperature deformation behavior and thermal stability of ultra-fine-grained W by Re alloying, *J. Mater. Res.*
- [26] N. Ahmed, A. Hartmaier, Mechanisms of grain boundary softening and strain-rate sensitivity in deformation of ultrafine-grained metals at high temperatures, *Acta Mater.* 59 (11) (2011) 4323–4334.

- [27] A. Nazarov, Kinetics of grain boundary recovery in deformed polycrystals, *Interface Sci.* 8 (4) (2000) 315–322.
- [28] L. Priester, Grain boundaries: from theory to engineering, Vol. 172, Springer Science & Business Media, 2012.
- [29] X. Liu, H. Zhang, K. Lu, Strain-induced ultrahard and ultra-stable nanolaminated structure in nickel, *Science* 342 (6156) (2013) 337–340.
- [30] Z. Wang, S. Divinski, Z. Luo, Y. Buranova, G. Wilde, K. Lu, Revealing interfacial diffusion kinetics in ultra-fine-laminated Ni with low-angle grain boundaries, *Mater. Res. Lett.* 5 (8) (2017) 577–583.
- [31] O. Renk, V. Maier-Kiener, C. Motz, J. Eckert, D. Kiener, R. Pippan, How the interface type manipulates the thermochemical response of nanostructured metals: A case study on nickel, *Materialia* (2021) 101020.
- [32] R. Smialek, T. Mitchell, Interstitial solution hardening in tantalum single crystals, *Philos. Mag.* 22 (180) (1970) 1105–1127.
- [33] R. Arsenault, An investigation of the mechanism of thermally activated deformation in tantalum and tantalum-base alloys, *Acta Metall.* 14 (7) (1966) 831–838.
- [34] G. Das, R. Arsenault, Non-monotonic strengthening in bcc solid solutions, *Scripta Metall.* 2 (9) (1968) 495–499.
- [35] W. Knabl, G. Leichtfried, R. Stickler, Refractory metals and refractory metal alloys, in: Springer Handbook of Materials Data, Springer, 2018, pp. 307–337.
- [36] O. Renk, P. Ghosh, R. Pippan, Generation of extreme grain aspect ratios in severely deformed tantalum at elevated temperatures, *Scripta Mater.* 137 (2017) 60–63.
- [37] A. Vorhauer, R. Pippan, On the onset of a steady state in body-centered cubic iron during severe plastic deformation at low homologous temperatures, *Met. Mater. Trans. A* 39 (2) (2008) 417–429.
- [38] F. Wetscher, R. Pippan, Cyclic high-pressure torsion of nickel and Armco iron, *Philos. Mag.* 86 (36) (2006) 5867–5883.
- [39] M. W. Kapp, O. Renk, T. Leitner, P. Ghosh, B. Yang, R. Pippan, Cyclically induced grain growth within shear bands investigated in ufg Ni by cyclic high pressure torsion, *J. Mater. Res.* 32 (23) (2017) 4317.
- [40] J. Wheeler, J. Michler, Elevated temperature, nano-mechanical testing in situ in the scanning electron microscope, *Rev. Sci. Instrum.* 84 (4) (2013) 045103.
- [41] W. C. Oliver, G. M. Pharr, An improved technique for determining hardness and elastic modulus using load and displacement sensing indentation experiments, *J. Mater. Res.* 7 (6) (1992) 1564–1583.
- [42] B. Lucas, W. Oliver, Indentation power-law creep of high-purity indium, *Metall. Mater. Trans. A* 30 (3) (1999) 601–610.
- [43] V. Maier, K. Durst, J. Mueller, B. Backes, H. W. Höppel, M. Göken, Nanoindentation strain-rate jump tests for determining the local strain-rate sensitivity in nanocrystalline Ni and ultrafine-grained Al., *J. Mater. Res.* 26 (11).
- [44] W. Köstner, The temperature dependence of the modulus of elasticity of pure metals, *Z. Metallkd.* 39 (1).
- [45] G. Bérces, N. Chinh, A. Juhász, J. Lendvai, Kinematic analysis of plastic instabilities occurring in microhardness tests, *Acta Mater.* 46 (6) (1998) 2029–2037.
- [46] N. Q. Chinh, J. Gubicza, Z. Kovács, J. Lendvai, Depth-sensing indentation tests in studying plastic instabilities, *J. Mater. Res.* 19 (1) (2004) 31–45.
- [47] H. Ovri, E. T. Lilleodden, New insights into plastic instability in precipitation strengthened Al–Li alloys, *Acta Mater.* 89 (2015) 88–97.
- [48] H. Ovri, E. T. Lilleodden, On the estimation of thermal activation parameters for Portevin–Le Chatelier effect from nanoindentation data, *JOM* 71 (10) (2019) 3343–3349.
- [49] V. Maier-Kiener, K. Durst, Advanced nanoindentation testing for studying strain-rate sensitivity and activation volume, *JOM* 69 (11) (2017) 2246–2255.
- [50] J. Wheeler, J. Michler, Invited article: Indenter materials for high temperature nanoindentation, *Rev. Sci. Instrum.* 84 (10) (2013) 101301.
- [51] A. Bolshakov, G. Pharr, Influences of pileup on the measurement of mechanical properties by load and depth sensing indentation techniques, *J. Mater. Res.* 13 (4) (1998) 1049–1058.
- [52] U. Rodrian, H. Schultz, Dislocation relaxation peaks in tantalum, intrinsic and impurity dependent effects, *J. Phys. Colloq.* 42 (C5) (1981) 65–79.
- [53] U. Rodrian, H. Schultz., Observations on the snoek-koester-relaxation in the system tantalum-oxygen, *Z. Metallkd.* 73 (1982) 21–29.
- [54] J. Baur, W. Benoit, H. Schultz, The dislocation-internal friction peak γ in tantalum, *Acta Metall.* 37 (4) (1989) 1159–1166.
- [55] F. Qianfeng, The influence of deformation on snoek peak in ta-o system, *Scripta Mater.* 35 (3) (1996) 455–458.
- [56] M. S. Blanter, I. S. Golovin, H. Neuhauser, H. Sinning, Internal friction in metallic materials – A Handbook, Springer, 2007.
- [57] S. Nemat-Nasser, R. Kapoor, Deformation behavior of tantalum and a tantalum tungsten alloy, *Int. J. Plast.* 17 (10) (2001) 1351–1366.
- [58] E. Pink, Thermisch aktivierte Verunreinigungseffekte bei der Verformung von Tantal, *Planseebericht Für Pulvermetallurgie* 17 (1969) 262–269.
- [59] D. H. Lassila, A. Goldberg, R. Becker, The effect of grain boundaries on the athermal stress of tantalum and tantalum-tungsten alloys, *Metall. Mater. Trans. A* 33 (11) (2002) 3457–3464.
- [60] H. Aboulfadl, J. Deges, P. Choi, D. Raabe, Dynamic strain aging studied at the atomic scale, *Acta Mater.* 86 (2015) 34–42.
- [61] M. Soare, W. Curtin, Solute strengthening of both mobile and forest dislocations: The origin of dynamic strain aging in fcc metals, *Acta Mater.* 56 (15) (2008) 4046–4061.

- [62] E. Rizzi, P. Hähner, On the Portevin–Le Chatelier effect: theoretical modeling and numerical results, *Int. J. Plast.* 20 (1) (2004) 121–165.
- [63] R. Kirchheim, Metals as sinks and barriers for interstitial diffusion with examples for oxygen diffusion in copper, niobium and tantalum, *Acta Metall.* 27 (5) (1979) 869–878.
- [64] N. Peterson, Diffusion in refractory metals, Tech. rep. (1961).
- [65] R. Powers, M. V. Doyle, Diffusion of interstitial solutes in the group V transition metals, *J. Appl. Phys.* 30 (4) (1959) 514–524.
- [66] H. Mehrer, Diffusion in solids: fundamentals, methods, materials, diffusion-controlled processes, Vol. 155, Springer Science & Business Media, 2007.
- [67] J. Kappacher, A. Leitner, H. Clemens, V. Maier-Kiener, Combination of nanoindentation and microscopy for the examination of aluminum alloys in coarse- and ultrafine-grained condition, *Practical Metallography* 56 (7) (2019) 432–442.
- [68] K. Durst, V. Maier, Dynamic nanoindentation testing for studying thermally activated processes from single to nanocrystalline metals, *Curr. Op. Solid State Mater. Sci.* 19 (6) (2015) 340–353.
- [69] S. D. Antolovich, R. W. Armstrong, Plastic strain localization in metals: origins and consequences, *Prog. Mater. Sci.* 59 (2014) 1–160.
- [70] K. Leitner, P. Felfer, D. Holec, J. Cairney, W. Knabl, A. Lorich, H. Clemens, S. Primig, On grain boundary segregation in molybdenum materials, *Mater. Des.* 135 (2017) 204–212.
- [71] D. Scheiber, R. Pippan, P. Puschnig, L. Romaner, Ab initio search for cohesion-enhancing impurity elements at grain boundaries in molybdenum and tungsten, *Model. Simul. Mater. Sci. Eng.* 24 (8) (2016) 085009.
- [72] L.-L. Niu, X. Shu, Y. Zhang, F. Gao, S. Jin, H.-B. Zhou, G.-H. Lu, Atomistic insights into shear-coupled grain boundary migration in bcc tungsten, *Mater. Sci. Eng. A* 677 (2016) 20–28.
- [73] O. Renk, R. Pippan, Transition from thermally assisted to mechanically driven boundary migration and related apparent activation energies, *Scripta Mater.* 154 (2018) 212–215.
- [74] T. Rupert, D. Gianola, Y. Gan, K. Hemker, Experimental observations of stress-driven grain boundary migration, *Science* 326 (5960) (2009) 1686–1690.
- [75] V. Maier-Kiener, X. An, L. Li, Z. Zhang, R. Pippan, K. Durst, Influence of solid solution strengthening on the local mechanical properties of single crystal and ultrafine-grained binary Cu–Al X solid solutions, *J. Mater. Res.* 32 (24) (2017) 4583–4591.
- [76] J. Crank, *The Mathematics of Diffusion*, Oxford University Press, 1975.
- [77] M. Cowgill, J. Stringer, The effect of oxygen pressure on the high temperature oxidation of tantalum, *J. Less Common Met.* 2 (2-4) (1960) 233–240.
- [78] I.-C. Choi, C. Brandl, R. Schwaiger, Thermally activated dislocation plasticity in body-centered cubic chromium studied by high-temperature nanoindentation, *Acta Mater.* 140 (2017) 107–115.
- [79] D. Brunner, Comparison of flow-stress measurements on high-purity tungsten single crystals with the kink-pair theory, *Mater. Trans. JIM* 41 (1) (2000) 152–160.
- [80] H. Li, C. Draxl, S. Wurster, R. Pippan, L. Romaner, Impact of d-band filling on the dislocation properties of bcc transition metals: The case of tantalum-tungsten alloys investigated by density-functional theory, *Phys. Rev. B* 95 (9) (2017) 094114.
- [81] D. Tabor, *The hardness of metals*, Oxford university press, 1951.
- [82] A. Leitner, V. Maier-Kiener, D. Kiener, Extraction of flow behavior and Hall–Petch parameters using a nanoindentation multiple sharp tip approach, *Adv. Eng. Mater.* 19 (4) (2017) 1600669.
- [83] X. Qian, Y. Chou, Grain boundary diffusion of chromium in niobium bicrystals, *Philos. Mag. A* 52 (2) (1985) L13–L18.
- [84] I. Kaur, Y. Mishin, W. Gust, et al., *Fundamentals of grain and interphase boundary diffusion*, John Wiley, 1995.
- [85] P. Heitjans, J. Kärger, *Diffusion in condensed matter: methods, materials, models*, Springer Science & Business Media, 2006.
- [86] D. Hull, D. J. Bacon, *Introduction to dislocations*, Butterworth-Heinemann, 2001.

High temperature nanoindentation as a tool to investigate plasticity upon phase transformations demonstrated on Cobalt

Johann Kappacher, Michael Tkadletz, Helmut Clemens, Verena Maier-Kiener

Department of Materials Science, Montanuniversität Leoben, Austria

Abstract:

A new field of application for high temperature nanoindentation as a complimentary method to understand the mechanics of plasticity upon bulk phase transformations in thermodynamic equilibrium is introduced. The feasibility is outlined on polycrystalline Cobalt involving a low-temperature hexagonal closed packed phase, and above 700 K, a high-temperature face centered cubic phase, which was conventionally characterized by means of differential scanning calorimetry and high temperature X-ray diffraction. Strain rate sensitivity, activation volume and activation energy of plastic deformation were determined up to 873 K to identify the rate-controlling deformation mechanism. From RT to 473 K plasticity was found to be controlled by lattice friction on the basal plane, where dislocations have to overcome the Peierls barrier and deformation twinning was apparent in the hexagonal phase. The thermal activation of cross slip lead to reduced twinning actions when the phase transition temperature is approached. In the high temperature face centered cubic phase deformation was found to be controlled by cutting of forest dislocations and no deformation twinning was observed.

Keywords:

mechanical phase transition characterization, high temperature nanoindentation, deformation twinning, hcp metals, thermally activated process

1. Introduction

Serious advances in high temperature nanoindentation testing have been made in the last couple of years, allowing to investigate thermally activated mechanisms in a variety of materials [1]. Small-scale probing of hardness, Young's modulus and rate-dependent properties nowadays enables examination of changes in dislocation plasticity [2–5]. Even the kinetics of static recrystallization [6] appears feasible. However, little attention has been drawn to phase transformations and its consequence for crystal plasticity. Earlier research showed the utility of high temperature nanomechanical techniques to investigate the flow stress of amorphous materials towards the glass transition temperature, *e.g.* in bulk metallic glasses [7, 8] or amorphous Selenium [9]. Investigations regarding a phase transition in terms of rearrangement of the crystal structure on the other hand, have not been reported before. Therefore, this work aims to demonstrate high temperature nanoindentation as a complimentary method for standard thermal analysis techniques to investigate the consequences of crystallographic changes on the plastic deformation behavior shown on metallic Cobalt.

The ferromagnetic transition metal Co has a high Curie temperature of 1390 K and a melting point, T_m , of 1768 K [10]. At room temperature (RT) Co exhibits a hexagonal close packed (hcp) structure (α -Co, historic: ϵ [11]) with the lattice parameters $a = 0.25071$ nm and $c = 0.40696$ nm [12], giving a ratio of $c/a = 1.623$, close to the ideal one of 1.633. The stacking fault energy is known to be low with 31 mJ m^{-2} at RT and decreases with increasing temperature to 20.5 mJ m^{-2} at 643 K [13]. Upon heating, Co undergoes a phase transformation at around 700 K [14] into a face centered cubic (fcc) modification (β -Co, historic: α [11]) with the lattice parameter $a = 0.354$ nm [15]. The allotropic transformation is of displacive nature [16, 17]. Investigations on the static mechanical deformation behavior in the temperature range from 300 K to 1450 K on bulk Co were mainly done in the 1960s, with the work of Betteridge [14] giving an overview. More recent research focus either on the mechanical properties of the low-temperature hcp [18–20] or high-temperature fcc phase [21–23].

In a hcp structure plastic deformation essentially involves dislocation movement, *i.e.* $\langle 11\bar{2}0 \rangle$ slip on the $\{0001\}$ basal, $\{10\bar{1}0\}$ first-order prismatic or $\{10\bar{1}1\}$ first-order pyramidal planes as well as $\langle 11\bar{2}3 \rangle$ slip on the $\{10\bar{1}1\}$ and $\{11\bar{2}2\}$ second-order pyramidal planes [24]. To fulfill the von Mises criterion, deformation twinning plays an important role to accommodate

plasticity. At RT twinning in the $\{10\bar{1}2\}$ planes is operative in most hcp metals, as this mode has the lowest shear magnitude [25].

In Co and Mg, both having a very similar c/a ratio, slip along the $\langle 11\bar{2}0 \rangle$ direction on the $\{0001\}$ basal plane is the predominant mechanism for dislocation glide [26]. The critically resolved shear stress (CRSS) for the activation of dislocation slip in Co is strongly temperature dependent at low homologous temperatures [27, 28]. Investigations regarding other slip systems are not reported, but are assumed to be significantly harder to activate. At high strains, however, $\langle 11\bar{2}0 \rangle$ slipping can not accommodate for deformation along the c -axis of the crystal and slip along $\langle 11\bar{2}3 \rangle$ is difficult to activate since its higher CRSS. Therefore, deformation twinning in Co takes place mainly via $\{10\bar{1}2\}\langle 1\bar{2}10 \rangle$ [20, 29], although also other modes are reported.

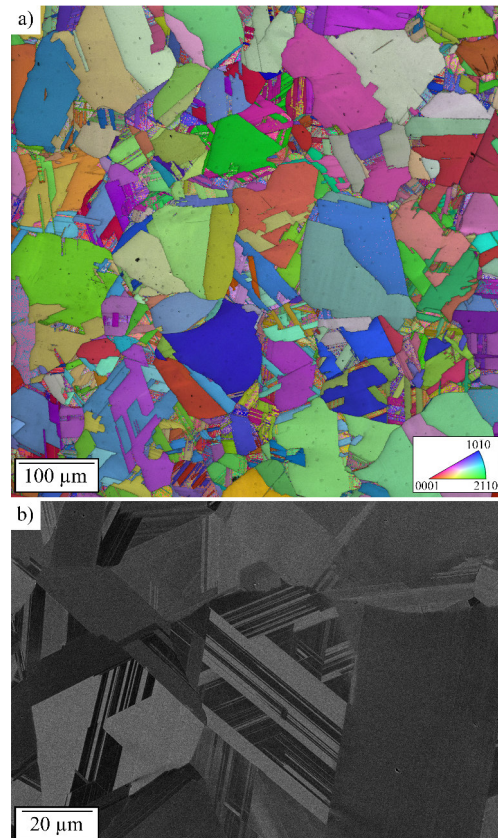


Figure 1: Electron microscopy images of the investigated Co sample: a) EBSD grain orientation map with an average grain size of $60 \pm 39 \mu\text{m}$ and b) BSE image revealing a grain with extensive annealing twins of a few micrometer in the width.

Deformation twins in Mg nucleate due to a local stress concentration stemming from a pile-up of prismatic $\langle 11\bar{2}0 \rangle$ dislocations that cross slip to the basal plane and dissociate into partial dislocations as reported in [30]. In single crystalline Mg deformation twinning

bears the deformation in case the crystal is orientated accordingly, however, twinning is suppressed and prismatic dislocation glide occurs as temperature exceeds 423 K [31]. Such a temperature dependence of deformation twinning is a result of changing CRSS for dislocation glide on different slip systems and twinning [32, 33]. In the complex stress field during nanoindentation deformation twinning can be observed independent of the orientation of the investigated crystal [34, 35].

There appears to have been little or no previous work focused on pure Cobalt relating deformation behavior, rate controlling deformation mechanisms and high temperature phase transformation. Other research focuses mainly on Co base alloys [36–39]. Apart from the beneficial small required sample volumes, there is also interest in whether the high local stresses created during nanoindentation are likely to induce a change in crystal structure below the phase transformation temperature.

2. Materials and methods

A polycrystalline Co rod with a purity of 99.9% was obtained by GoodFellow GmbH (Hamburg, Germany) in the as-drawn condition. In order to receive a material that is almost in thermodynamic equilibrium, annealing in a high vacuum furnace (HTM Reetz GmbH, Berlin, Germany) at a base pressure of $<5.0 \times 10^{-6}$ mbar was performed. The samples were heated to 1061 K, corresponding to $0.6 T_m$ in the fcc phasefield, held for 150 min, followed by a slow cooling of 1 K min^{-1} to 663 K (hcp phasefield), for another holding time of 12 h and finally cooled down to RT. The second holding step was chosen to ensure thermal stability of the microstructure close to the phase-transition temperature for the following high-temperature testing. All experiments were carried out in the axial direction of the rod after the samples were carefully ground with SiC sandpaper and mechanical polished. To remove any remaining deformation layer, a final electropolishing step was conducted at 40 V for 60 s with an A2 electrolyte of Struers GmbH (Willich, Germany).

Microstructural investigations were carried out on a Tescan Clara scanning electron microscope (SEM) (Tescan, Brno, Czech Republic) using back-scattered electron (BSE) imaging at 15 kV. Additional electron back-scattered diffraction (EBSD) experiments were performed on a field emission SEM FEI Versa 3D DualBeam (Thermo Fisher Scientific, Waltham, MA), equipped with an EDAX Hikari XP EBSD system (EDAX Inc., Mahwah, NJ) at 20 kV. The data was analyzed using the standard software package OIM analysis 7 from EDAX Inc.

In order to determine the phase transformation temperature, differential scanning calorimetry (DSC) measurements were carried out in Ar atmosphere up to 1073 K, utilizing heating rates of 5 and 10 K min^{-1} . The experiments were executed on a LabSYS Evolution system (SETARAM Instrumentation, Caluire, France) and the samples weight was 50 ± 3 mg, always enclosed by a $100 \mu\text{l}$ alumina crucible. High temperature X-ray diffraction (XRD) experiments were conducted using a Bruker AXS D8 Advance diffractometer (Bruker AXS GmbH, Karlsruhe, Germany) with a Cu X-ray tube and an energy dispersive Lynxeye XE-T detector. Parallel beam optics were used for the experiments, employing a Göbel mirror. A high temperature heating chamber HTK 1200 N (Anton Paar, Graz, Austria) was installed on the diffractometer to allow for heating the sample in He atmosphere. Diffraction intensities were isothermally detected for the 2θ range between 40 and 55° with a step size of 0.03° using a record time of 1 s per step. Measurements were performed at 298, 373, 473, 573, 623, 648, 723, 748, 773, 873, and 973 K with smaller temperature steps of 5 K between 648 and 723 K.

To account for mechanical properties on both sides of the phase transition temperature, high temperature nanoindentation experiments were conducted on an InSEM-HT (Nanomechanics Inc., KLA, Oak Ridge, TN), equipped with a continuous stiffness measurement unit. The superimposed force signal had a frequency of 100 Hz and a displacement amplitude of 2 nm, allowing a continuous record of the contact stiffness and thus Young's modulus and hardness over indentation depth. The setup is mounted in an Tescan Vega3 SEM (Tescan, Brno, Czech Republic) under high vacuum ($<5.0 \times 10^{-4}$ mbar). A SiC Berkovich tip (Synton-MDP, Nidau, Switzerland) was used for the experiments and frame stiffness and area function of the tip were obtained by RT indentation tests on fused quartz according to the analysis of Oliver and Pharr [40]. After the tests the sample was examined in a light optical microscope to exclude any surface oxidation. Nanoindentation experiments were conducted at 298, 373, 473, 523, 573, 623, 673, 723, 773, and 873 K. To acquire Young's modulus, E , and hardness, H , of the material constant indentation strain rate experiments at $\dot{P}/P = 0.1 \text{ s}^{-1}$ were performed up to 900 nm, with values averaged between 700 nm and 800 nm. A Poisson's ratio of 0.32 [41] for Co was assumed to calculate the Young's modulus and at least twelve indents were performed at each temperature and test protocol. Additionally, nanoindentation strain rate jump tests were performed as introduced by Maier *et al.* [42]. Therefore, the strain rate was kept constant

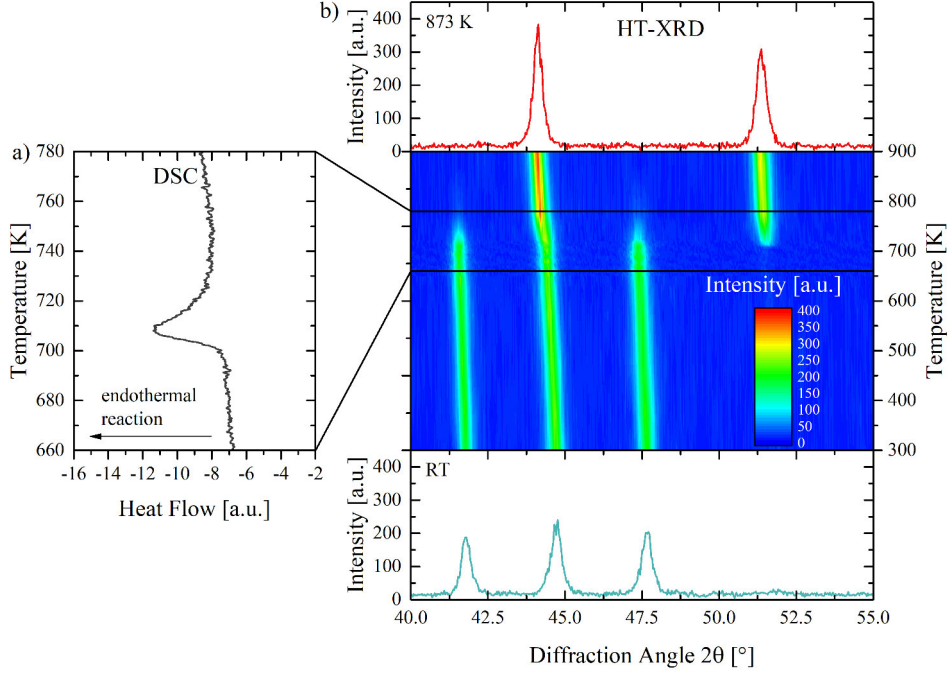


Figure 2: Results of the determination of the phase transformation temperature by means of a combination of a) DSC and b) HT-XRD experiments. In the DSC measurements, that were carried out at 10 K min^{-1} the start and finish of the transformation can be detected at 700 K and 740 K, respectively and no significant shift in transition temperature was examined for lower heating rates. At RT the three (1 0 0), (0 0 2) and (1 0 1) hcp peaks can be seen in the XRD experiments. First peaks of the fcc phase are detected at 708 K and last hcp signals can be observed at 748 K. At 873 K only the two (1 1 1) and (2 0 0) fcc peaks are remaining.

at $\dot{P}/P = 0.1 \text{ s}^{-1}$ up to 500 nm, followed by an abrupt change of an order of magnitude to $\dot{P}/P = 0.01 \text{ s}^{-1}$ for additional 175 nm and finally going back to the initial strain rate $\dot{P}/P = 0.1 \text{ s}^{-1}$ for another 175 nm.

$$m = \frac{\partial(\ln(H))}{\partial(\ln(\dot{\epsilon}))} \quad (1)$$

$$V^* = \frac{C^* \cdot \sqrt{3} \cdot k_B \cdot T}{m \cdot H} \quad (2)$$

From the resultant instantaneous change in hardness [43], strain rate sensitivity m and the apparent activation volume V^* can be extracted according to Equ. 1 and 2, where C^* is a constraint factor of 2.8 and k_B is the Boltzmann constant. The activation volume is normalized to the cubed Burger's vector b^3 with $b = 0.25 \text{ nm}$ [12] to facilitate comparison between different materials and it describes the atoms collectively involved in the rate limiting process [1].

3. Results

In Fig. 1 the microstructure of the investigated Co sample is summarized. From the color-coded inverse pole figure maps obtained by EBSD in Fig. 1a) an average grain diameter of $60 \pm 39 \mu\text{m}$ was determined, where twin boundaries were counted as grain boundaries. The

grain size is, as already derived from the high standard deviation, rather inhomogeneous with some grains exhibiting annealing twins in the micrometer range (Fig. 1b), resulting from the low stacking fault energy of Co [14].

DSC and HT-XRD experiments in Fig. 2 clearly indicate a phase transformation from the low-temperature hcp to a high temperature fcc phase. The measured heat flow during heating in the DSC experiment (Fig. 2a), indicates the appearance of first fcc phase at 700 K and a finish of the transformation at 740 K with a peak in the endothermic reaction between 705 K and 710 K. This correlates well with the HT-XRD measurements (Fig. 2b), where first signals from the fcc phase were detected at 708 K and the last hcp peaks were observed at 748 K. The slight shift of the peaks during the diffraction experiments to lower diffraction angles with increasing temperature originates from the thermal expansion of the crystal lattice.

The phase transformation can also be observed during heating in the nanoindentation system, see Fig. 3. The InSEM-HT system not only allows to track the current temperature upon heating, but also the heating power is accessible. When plotted over temperature (Fig. 3a), an increased power is required to follow the heating ramp of 10 K min^{-1} , *i.e.* an endothermic reaction takes place. It

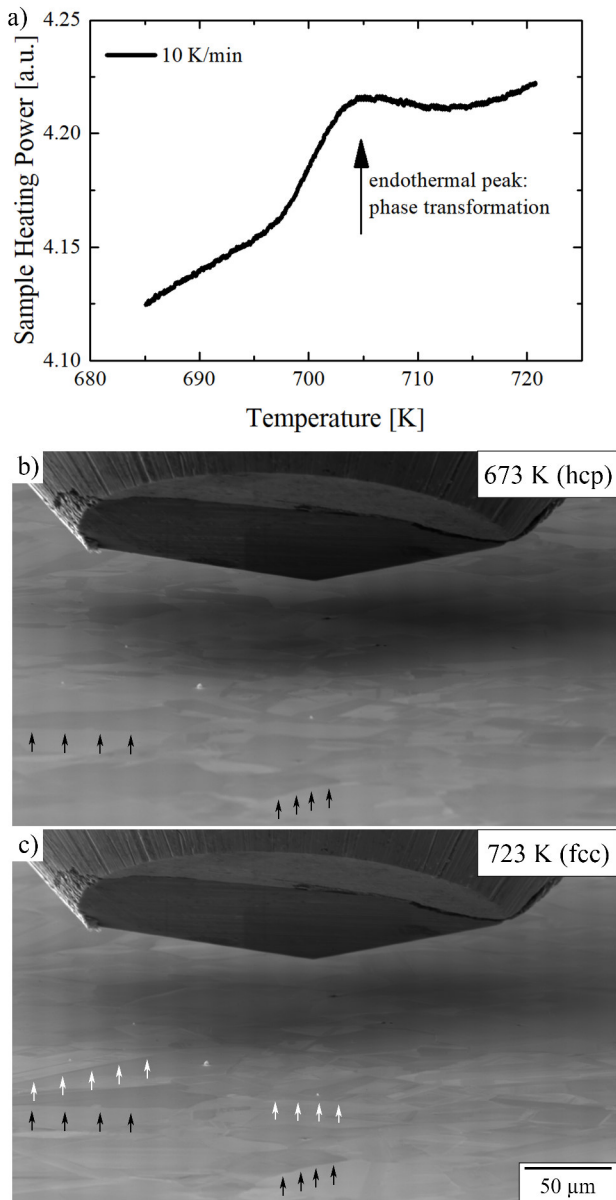


Figure 3: a) Required sample heating power of the high temperature nanoindentation system to overcome the phase transition temperature. *In situ* SEM images of the indenter and Co sample surface tilted 10° with respect to the incoming electron beam allows for investigation of the sample surface and microstructure b) before (at 673 K) and c) after (at 723 K) phase transformation. Selected remaining grain boundaries are indicated with black arrows, while new formed boundaries are highlighted with white arrows.

peaks at 705 K, agreeing well with the results obtained by DSC-measurements (Fig. 2). For high temperature nanoindentation knowledge about the thermal gradients within the system is essential for valid data acquisition and interpretation. Up to date this is achieved by a tip-temperature calibration where different procedures were presented as reported in [44]. The capability to track phase transitions by examining the sample heating power opens further the possibility to reliably perform a tem-

perature calibration of a nanoindentation system by simply heating different samples above their allotropic transformation temperature. Considering additional materials with different solid-state transition temperatures, *e.g.* perlitic steel (996 K), pure Fe (1184 K and 1665 K) or different bronze alloys, where a variety of phase transformations occur, such a calibration procedure would be conceivable.

Moreover, examining the sample surface tilted by 10° with respect to the incoming electron beam allows to *in situ* follow the phase transformation and its consequence for the materials microstructure. Figures 3b) and c) represent SEM images taken in secondary electron contrast of the sample with the Berkovich indenter $20\ \mu\text{m}$ away from the surface at the same position before (673 K) and after (723 K) the phase transformation, respectively. While some grain boundaries remain unchanged, indicated by black arrows, new interfaces are formed across preexisting boundaries as highlighted by white arrows. This behavior can be explained by the orientation relation between the low-temperature hcp and the high-temperature fcc phase [16, 17]. Also, no sign of surface topography can be observed upon phase transition, which might lead to falsified results during nanoindentation.

Figure 4 presents the evolution of Young's modulus a) and hardness b) over temperature with additional values taken from literature [45–47]. At RT a Young's modulus of 177.9 ± 8.1 GPa was measured, followed by a monotonous decrease over temperature to 147.7 ± 5.4 GPa at 873 K. In contrast to the Young's modulus, hardness values decrease from 2.87 ± 0.19 GPa at RT continuously to 1.93 ± 0.12 GPa at 673 K, followed by an abrupt drop upon phase transformation to 1.07 ± 0.04 GPa at 723 K, after which they remain rather constant up to 873 K (0.97 ± 0.11 GPa).

During the loading sequence numerous displacement bursts, as illustrated in the load-displacement curves in Fig. 5, could be observed. The nanoindentation system is intrinsically load controlled, therefore, those displacement bursts characterize a sudden increase in indentation displacement ranging from 5 to 50 nm in between two data points at constant loads, but random load levels. As the data acquisition rate was 40 Hz, these events take place within less than 25 ms. To identify the origin of these events, three different RT residual indentations were investigated by means of EBSD. All three impressions showed quantitatively identical results with two representative shown in Fig. 5. The indent in Fig. 5a) was performed in a single grain with an orientation close to $\{0001\}$, while Fig. 5b) was executed close to a

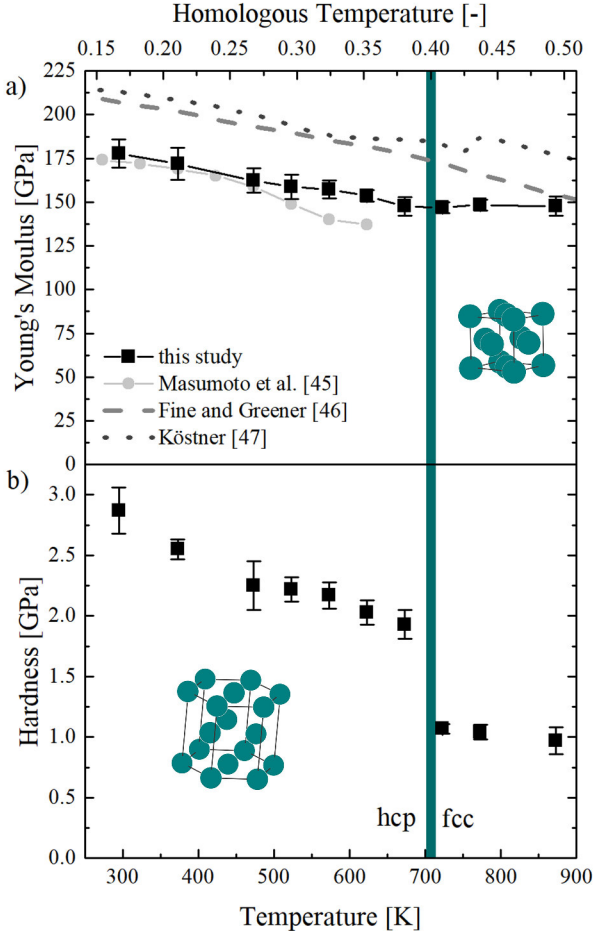


Figure 4: Evolution of Young's modulus a) with additional literature values [45–47] and hardness b) over temperature derived from HT nanoindentation. While E shows a gradual decrease over temperature, H reveals a drop of almost 50 % as the phase changes from hcp to fcc.

grain boundary, where twinning was observed in a grain closely orientated to $\{10\bar{1}0\}$. The inverse pole figure maps revealed two deformation twins (T1, T2) for the former and one deformation twin (T3) for the latter indent. Thus, the number of displacement bursts matches exactly with the observed deformation twins. The pole figures are revealing, that the parent grain and deformation twins share a certain $\{10\bar{1}2\}$ plane. Misorientation plots, as indicated in the inverse pole figure maps, report a misorientation angle between parent grain and deformation twins of 85.6, 86.9 and 85.8° for T1, T2, and T3, respectively. In an approach to quantify these displacement bursts, we counted those larger than 5 nm at an indentation depth exceeding 200 nm, to exclude for any initial pop-in events representing the transition from purely elastic to elastic-plastic deformation [48]. This absolute number was then divided by the number of indents at a certain testing temperature, giving an average

number of displacement bursts per indent. An increasing frequency of such events was detected as the temperature increased from RT to 523 K, followed by a decrease as temperature approached towards the phase transformation temperature, see Fig. 6.

In Fig. 7 details of representative strain rate jump tests at RT, 673 K (hcp) and 723 K (fcc) are shown. In a) the Young's modulus and in b) hardness are plotted over displacement. While the Young's modulus is unaffected by a change in strain rate, the corresponding hardness changes significantly for experiments performed in the hcp phase. Magnifications of the hardness of single strain rate jumps are presented in Figs. 7c-e). For the hcp phase deformation twinning events, that result in a drop in hardness, are indicated with arrows.

The strain rate sensitivity and apparent activation volume as well as the derived activation energy for plastic deformation Q are presented in Fig. 8. The latter was approximated by the apparent activation enthalpy $\Delta\mathcal{H}$ according to Equ. 3, as demonstrated by Lee *et al.* [49].

$$Q \approx \Delta\mathcal{H} = \frac{H \cdot V^*}{\sqrt{3} \cdot C^* \cdot T} \cdot \frac{\partial(\ln H)}{\partial(1/T)} \quad (3)$$

From RT to 473 K a constant strain rate sensitivity of 0.011 ± 0.003 , combined with an increasing activation volume from $42 \pm 9b^3$ to $81 \pm 21b^3$ and an activation energy of 1.5 to 2 eV can be observed. Starting at 523 K the strain rate sensitivity rises with increasing temperature up to 0.023 ± 0.007 at 673 K. At the same time the activation volume is rather constant at around $75b^3$ and the activation energy for plastic deformation decreases to values between 0.8 and 1.0 eV. Finally, indentation of the fcc phase at high temperatures revealed a low strain rate sensitivity (0.009 ± 0.002) and a sudden rise in the activation volume to $343 \pm 126b^3$ at 523 K that continues to increase to $456 \pm 104b^3$ at 873 K. The activation energy for plastic deformation in the high temperature regime was found to be between 3.5 and 4.0 eV.

4. Discussion

The affected volume of an indent with 900 nm indentation depth can be expected to be around $9 \mu\text{m}$ in diameter [50], thus considerably smaller than the average grain size (Fig. 1). While the observed hardness values may for some indents be affected by regions of a higher density of interfaces, the rate controlling process for plasticity, reflected in the observed strain rate sensitivity, activation volume as well as activation energy, will hardly be influenced towards grain boundary sliding or similar processes, as could be expected in nanocrystalline materials. Hence, nanoindentation allows for the

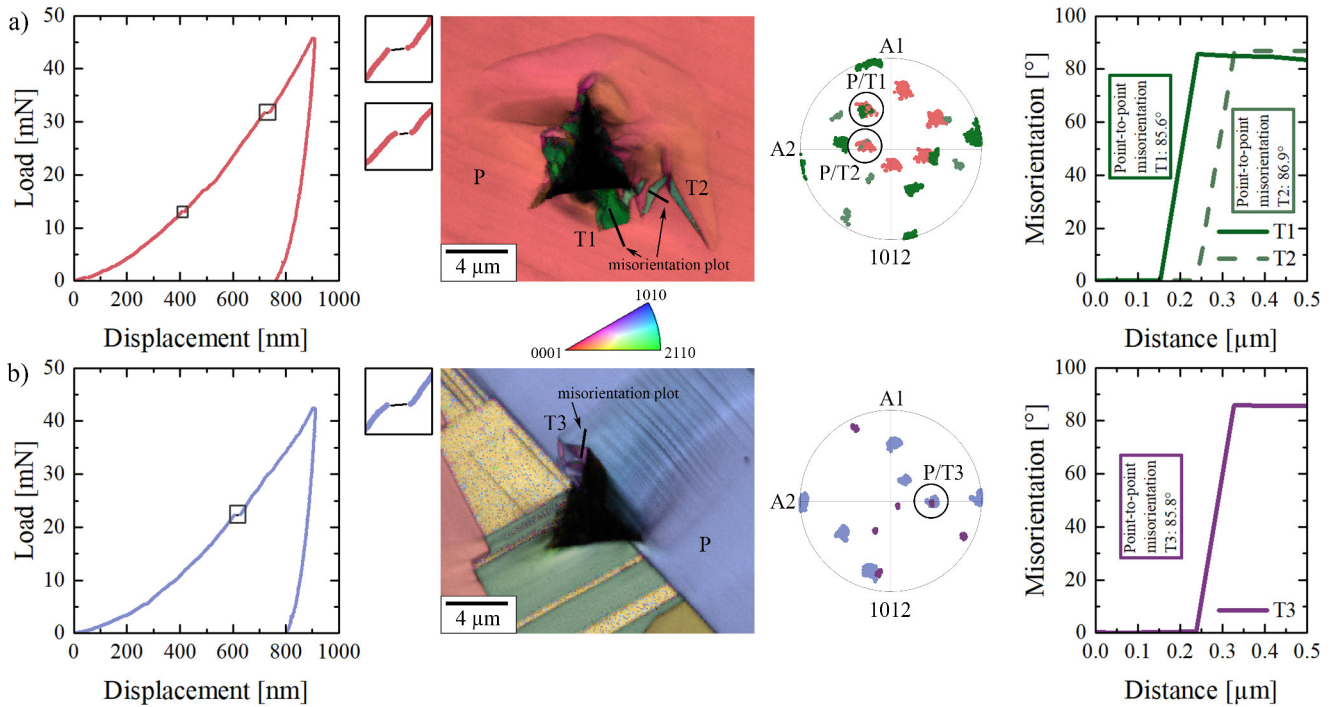


Figure 5: Two representative load-displacement curves of indents performed at RT. The EBSD examination of the remaining indents include inverse pole figure maps, pole figures with highlighted parent and twin orientation as well as misorientation plots. The indent in a) was performed in a single grain with a parent orientation close to $\{0001\}$, while b) was executed close to a grain boundary where twinning was observed in a grain closely orientated to $\{10\bar{1}0\}$.

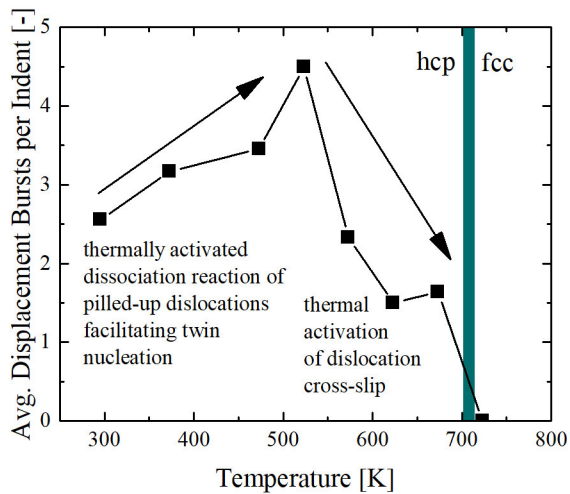


Figure 6: Average displacement bursts per indent over temperature observed in the hcp phase. A change in twinning activity was apparent over temperature with a peak at 523 K. No displacement bursts were examined after phase transformation in the fcc phase.

local probing of intrinsically single crystalline behavior of a usually polycrystalline sample material that the following argumentation refers to.

4.1. Mechanical properties and deformation twinning

Due to the hcp Co crystal structure a strong anisotropic elastic behavior can be expected. Masumoto

et al. [45] determined values for Young's moduli in different crystal directions and reported 213, 169, 175, and 174 GPa in $\langle 0001 \rangle$, $\langle 10\bar{1}2 \rangle$, $\langle 10\bar{1}0 \rangle$, and $\langle 11\bar{2}0 \rangle$ direction, respectively. The strong elastic anisotropy was confirmed by several other authors [51–53]. Vlassak and Nix [54] demonstrated on single crystals of hcp Zn that the measured modulus during nanoindentation can vary by as much as a factor of two, while the maximum change in hardness with orientation is about 20%. However, the anisotropy of the elastic constants is more pronounced in Zn compared to Co [55]. The reported literature values for Young's modulus of Co vary from 174 to 214 GPa [45–47]. A possible explanation could be differently textured samples of the experiments. The observed temperature dependence, however, is remarkable consistent. Our experimental data is well within the reported range and follows the same trend over temperature, thus underlining the validity of our results. The consistent temperature dependence also confirms that 12 indents per temperature and test protocol are statistically sufficient to depict average values of mechanical properties for randomly orientated grains.

A few studies regarding the influence of phase transformation on the mechanical properties of coarse grained Co have been performed [56–59]. The results differ remarkably and, notably, no discontinuity is reported for

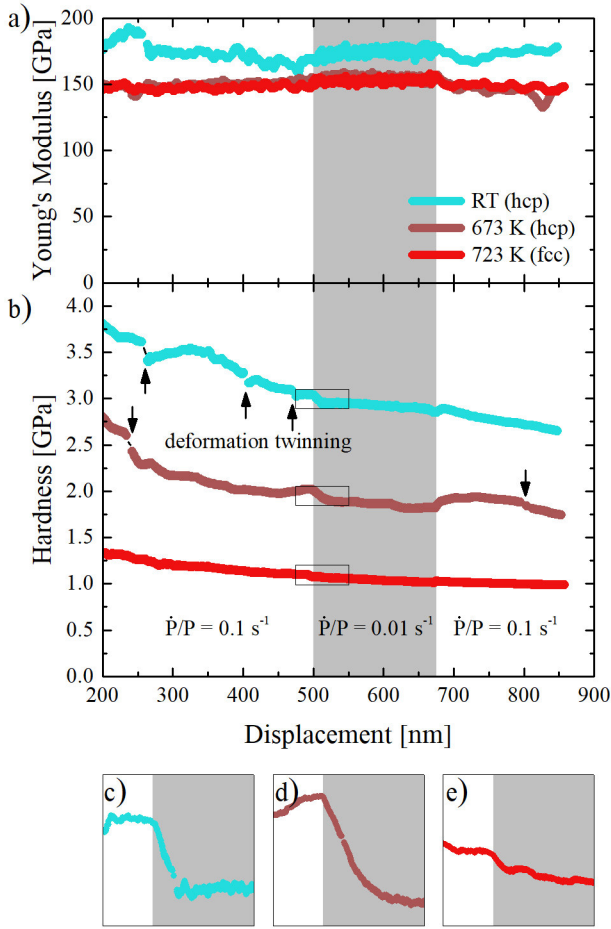


Figure 7: Representative Young's modulus a) and hardness b) over displacement plots of the strain rate jump tests conducted at RT, 673 K (hcp) and 723 K (fcc). Arrows indicate deformation twinning events in the hcp phase. Details in higher magnification of the first jump for the three different temperatures are plotted in c)-e).

tensile strength or hardness over temperature once the phase transformation was reached at 700 K. It could be assumed that this discrepancy arises from the thermal history or the content of impurities of the investigated materials [14]. The drop in hardness of almost 50% once the crystal structure changes from hcp to fcc can be explained by a remarkably reduced friction stress for dislocation glide in the fcc crystal compared to the hcp structure. As in the fcc lattice also more slip systems are active in different crystal directions, no dislocation pile-up on a limited number of slip planes is expected.

Deformation twinning during nanoindentation with an intrinsically load controlled system manifests as displacement bursts, while sharp, "wing-like" changes of the crystal orientation can be observed around the remaining indent [60, 61]. The most common twin modes in Co during tensile deformation are tension twins along the $\{10\bar{1}2\}$ plane with a rotation angle of 86° around the $\langle 1\bar{2}10 \rangle$ axis due to the lowest twinning shear magni-

tude [20, 29, 62]. The same type of twins were detected in this nanoindentation study, as can be derived from the shared $\{10\bar{1}2\}$ plane and the misorientation angle between parent grain and twin in Fig. 5. In the hcp phase twinning apparently bears a significant amount of plastic deformation. A peak in twinning activity with increasing temperature, see Fig. 6, is in line with results obtained for different Mg alloys [63–65]. It is argued, that this is a result of changing CRSS for twinning and dislocation slip. However, the reported values of the CRSS for $\{10\bar{1}2\}\langle 1\bar{2}10 \rangle$ twinning in Mg is only slightly temperature dependent [32]. As twin nucleation requires pile-up and dissociation of dislocations [30], it is conceivable, that the latter process is thermally activated, resulting in a facilitation of twin nucleation with increasing temperature up to 523 K. As the maximum amount of deformation twins per indent is exceeded at 523 K, a different mechanism has to contribute to the plastic deformation in c-direction of the crystal. This temperature coincides with the start of an increasing strain rate sensitivity (Fig. 8a). Dislocation slip along the $\langle 11\bar{2}3 \rangle$ direction on non-basal planes [31] can bear such deformation. The thermal activation of such an additional slip system in the hcp Co lattice would in turn reduce the stress from piled-up dislocations on the basal plane causing twin nucleation and growth. Ultimately, this would result in the observed diminishing twinning activity.

4.2. Thermally activated deformation processes

A jump in the applied strain rate results in an immediate change in hardness at RT and 723 K. At 673 K, however, the hardness evolution shows a more transient behavior. Such a non-instantaneous hardness response during an abrupt change in strain rate is usually discussed in terms of coupled dislocation and grain boundary migration in ultra-fine grained materials as reported in [66]. Due to the large grain size in this study, grain boundary migration can hardly be responsible for this behavior. On the other hand, a deformation-induced phase transformation below the transition temperature would lead to a significantly larger hardness drop to similar values as measured at 723 K. Such a transient hardness response can also be observed in coarse grained Zr at RT [1], where dislocations slip on the prismatic plane occurs. Previous investigations outlined that the appearance of the hardness response on a changed strain rate can be a hint on how dislocations bear plasticity [67]. Therefore, it is tempting to speculate that the transient behavior is characteristic for a changed deformation mechanism at 673 K compared to RT.

In order to assess the dominating deformation mechanisms we first focus on the low-temperature hcp phase.

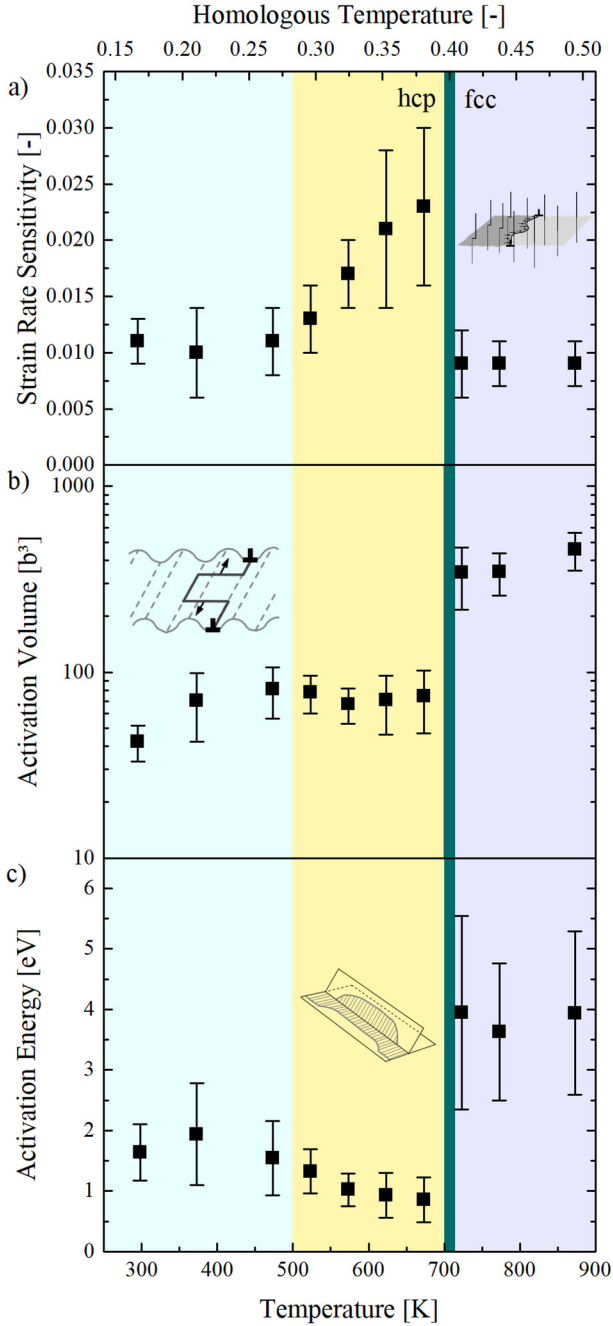


Figure 8: Results of the strain rate jump tests as a function of temperature. Upon the phase transformation a sudden decrease in the a) strain rate sensitivity a) as well as an increased activation volume b) and activation energy c) can be observed, indicating a change in the dominating deformation mechanism (see text).

Deformation twinning is present in the investigated temperature regime (Fig. 6), however, twin nucleation is considered rate-insensitive, but occurs at high stress concentrations [30, 32, 68]. Once nucleated, twins grow more readily than dislocation slip can propagate, hence twin growth can hardly be the rate-controlling process

during plastic deformation, at least at the moderate strain rates employed in the current study.

From the examined values for strain rate sensitivity, activation volume and activation energy, see Fig. 8, two different deformation regimes can be distinguished in the hcp Co phase. Between RT and 500 K the strain rate sensitivity is rather constant at a moderate level and an increasing activation volume with temperature can be observed. An activation volume of 10 to $100b^3$ is typically associated with lattice friction caused by the Peierls barrier or dislocation cross slip [69]. Further, a strong temperature dependence of the CRSS for $\langle 11\bar{2}0 \rangle \{0001\}$ dislocation slip at low homologous temperatures for Co is reported in [27, 28]. It can therefore be concluded, that roughly up to 500 K plasticity is dominated by lattice friction hindering dislocation slip on the basal plane. With increasing temperature the energy barrier becomes partially thermally activated and the activation volume increases. Very few values for the activation energy of plastic deformation of Co can be found in literature at increased temperature, however a value of 1.61 eV is reported up to 384 K [70], which is associated with the formation of vacancies by jogs dragged by basal dislocations. This is in line with the observed values in this study and thus supports its validity.

Starting at 523 K an increasing strain rate sensitivity with temperature can be observed (Fig. 8a). Such a behavior indicates an increasing thermally activated contribution to plasticity, in line with the observed decreasing twinning activity (Fig. 6). In metals with low stacking fault energies and dissociated dislocations, initiation of cross slip is a rate sensitive process [71, 72]. Also, the work hardening rate of hcp single crystals in general shows a peak at $0.3T_m$, indicating that dislocation cross slip is thermally activated above this temperature [73]. It is thus presumed, that dislocation cross slip along the $\langle 11\bar{2}3 \rangle$ direction on non-basal planes is the dominating deformation mechanism in hcp Co from 523 K to the phase transformation temperature. Dislocation cross slip was also reported to be the rate controlling mechanism during nanoindentation of Mg at similar homologous temperature [74, 75]. This mechanism gradually takes over deformation along the c-axis of the hcp crystal, while twinning is suppressed, in line with observations reported for Mg and Ti [31, 76]. No values for activation energies for cross slip in Co are reported, however, this deformation mechanism was intensively investigated on Mg. There, activation energies for cross slip are strongly dependent on the activated glide plane and alloy content, but values around 1 eV are reported [77].

Finally, the low strain rate sensitivities and high acti-

vation volumes determined in the fcc high temperature phase are typical for coarse-grained fcc metals, where obstacle controlled dislocation glide is the dominating deformation mechanism. The activation energy for plastic deformation in the high temperature regime of 3.5 to 4.0 eV can be rewritten as the "normalized activation energy" $\Delta\mathcal{H}/\mu b^3$ with a shear modulus μ of ~ 60 GPa and b of the high temperature fcc phase of 0.25 nm [15] giving values of 0.7 to $0.8\mu b^3$. This is in line with reported values of 0.2 to $1.0\mu b^3$ for dislocation plasticity that is controlled by cutting of forest dislocations [78].

5. Conclusions

In this study we demonstrated the application of micromechanical methods as an analysis tool for bulk phase transformation and its consequence on plasticity as well as elasticity. Therefore, high temperature nanoindentation combined with electron microscopy were carried out to investigate the rate-controlling mechanisms for plastic deformation in technically pure Co in both the hcp and fcc phase from RT to 873 K. The phase transformation was complimentary analyzed by means of differential scanning calorimetry and high temperature X-ray diffraction and was determined to occur around 700 K. The main conclusions can be drawn as follows:

- Between RT and 473 K lattice friction controls plasticity, where dislocations have to overcome a Peierls barrier. This results in a moderate strain rate sensitivity of 0.011, increasing activation volumes with temperature from $42b^3$ to $81b^3$ and an activation energy for plastic deformation in the range of 1.5 to 2 eV.
- With further temperature increase dislocation cross slip proceed facilitated through thermal activation, resulting in an increasing strain rate sensitivity and a reduced activation energy of 0.8 to 1.0 eV at an almost constant activation volume.
- Deformation twinning, which was identified as the $\{10\bar{1}2\}\langle 1\bar{2}10\rangle$ tension twin mode at RT, was present at all temperatures in the hcp phase. A rising twinning activity with increasing temperature could be observed up to 523 K owed to a thermal activation of twin nucleation. Promoted cross slip reduces the dislocation pile-up necessary for deformation twinning and hence a reduced twinning activity with further increasing temperature was detected.
- In the high temperature fcc phase a low strain rate sensitivity (0.009), high activation volumes of 350

to $450b^3$ and activation energies in the range of 3.5 to 4.0 eV were determined. These are values typically found for deformation that is dominated by obstacle controlled dislocation glide, *e.g.* cutting of forest dislocations.

Acknowledgments

J.K. wants to thank S. Jakob for his support with the EBSD measurements.

References

- [1] V. Maier-Kiener, K. Durst, Advanced nanoindentation testing for studying strain-rate sensitivity and activation volume, *JOM* 69 (11) (2017) 2246–2255. doi:<https://doi.org/10.1007/s11837-017-2536-y>.
- [2] I.-C. Choi, C. Brandl, R. Schwaiger, Thermally activated dislocation plasticity in body-centered cubic chromium studied by high-temperature nanoindentation, *Acta Mater* 140 (2017) 107–115. doi:<https://doi.org/10.1016/j.actamat.2017.08.026>.
- [3] O. Renk, V. Maier-Kiener, I. Issa, J. Li, D. Kiener, R. Pippan, Anneal hardening and elevated temperature strain rate sensitivity of nanostructured metals: their relation to intergranular dislocation accommodation, *Acta Mater* 165 (2019) 409–419. doi:<https://doi.org/10.1016/j.actamat.2018.12.002>.
- [4] B. D. Beake, A. J. Harris, J. Moghal, D. E. Armstrong, Temperature dependence of strain rate sensitivity, indentation size effects and pile-up in polycrystalline tungsten from 25 to 950 °C, *Mater Des* 156 (2018) 278–286. doi:<https://doi.org/10.1016/j.matdes.2018.06.063>.
- [5] C. Minnert, W. C. Oliver, K. Durst, New ultra-high temperature nanoindentation system for operating at up to 1100 °C, *Mater Des* (2020) 108727 doi:<https://doi.org/10.1016/j.matdes.2020.108727>.
- [6] P. Baral, M. Laurent-Brocq, G. Guillonnet, J.-M. Bergheau, J.-L. Loubet, G. Kermouche, In situ characterization of AA1050 recrystallization kinetics using high temperature nanoindentation testing, *Mater Des* 152 (2018) 22–29. doi:<https://doi.org/10.1016/j.matdes.2018.04.053>.
- [7] J. Wheeler, R. Raghavan, J. Michler, Temperature invariant flow stress during microcompression of a Zr-based bulk metallic glass, *Scripta Mater* 67 (2) (2012) 125–128. doi:<https://doi.org/10.1016/j.scriptamat.2012.03.039>.
- [8] L. Krämer, V. Maier-Kiener, Y. Champion, B. Sarac, R. Pippan, Activation volume and energy of bulk metallic glasses determined by nanoindentation, *Materials & Design* 155 (2018) 116–124. doi:<https://doi.org/10.1016/j.matdes.2018.05.051>.
- [9] C. Su, E. G. Herbert, S. Sohn, J. A. LaManna, W. C. Oliver, G. M. Pharr, Measurement of power-law creep parameters by instrumented indentation methods, *J Mech Phys Solids* 61 (2) (2013) 517–536. doi:<https://doi.org/10.1016/j.jmps.2012.09.009>.

- [10] H. Winterhager, J. Kruger, Pure cobalt and its properties, *Cobalt* 29 (1965) 185–195.
- [11] Centre D'Information du Cobalt, Cobalt Monograph, Vol. 185, C.I.C, Brussels, Belgium, 1960.
- [12] A. Taylor, R. W. Floyd, Precision measurements of lattice parameters of non-cubic crystals, *Acta Crystallogr* 3 (4) (1950) 285–289. doi:<https://doi.org/10.1107/S0365110X50000732>.
- [13] T. Ericsson, The temperature and concentration dependence of the stacking fault energy in the Co-Ni system, *Acta Metall Mater* 14 (7) (1966) 853–865. doi:[https://doi.org/10.1016/0001-6160\(66\)90006-X](https://doi.org/10.1016/0001-6160(66)90006-X).
- [14] W. Betteridge, The properties of metallic cobalt, *Prog in Mater Sci* 24 (1980) 51–142. doi:[https://doi.org/10.1016/0079-6425\(79\)90004-5](https://doi.org/10.1016/0079-6425(79)90004-5).
- [15] R. Kohlhaas, P. Dunner, P. Schmitz, The temperature-dependence of the lattice parameters of iron, cobalt, and nickel in the high temperature range, *Z Angew Physik* 23 (4) (1967) 437.
- [16] B. Strauss, F. Frey, W. Petry, J. Trampenau, K. Nicolaus, S. Shapiro, J. Bossy, Martensitic phase transformation and lattice dynamics of fcc cobalt, *Phys Rev B* 54 (9) (1996) 6035. doi:<https://doi.org/10.1103/PhysRevB.54.6035>.
- [17] O. Blaschko, G. Krexner, J. Pleschiutchnig, G. Ernst, C. Hitznerberger, H. Karnthaler, A. Korner, Coherent modulated structure during the martensitic hcp-fcc phase transition in Co and in a CoNi alloy, *Phys Rev Lett* 60 (26) (1988) 2800. doi:<https://doi.org/10.1103/PhysRevLett.60.2800>.
- [18] G. Fleurier, E. Hug, M. Martinez, P.-A. Dubos, C. Keller, Size effects and hall–petch relation in polycrystalline cobalt, *Phil Mag Lett* 95 (2) (2015) 122–130. doi:<https://doi.org/10.1080/09500839.2015.1020351>.
- [19] A. Karimpoor, K. Aust, U. Erb, Charpy impact energy of nanocrystalline and polycrystalline cobalt, *Scripta Mater* 56 (3) (2007) 201–204. doi:<https://doi.org/10.1016/j.scriptamat.2006.10.018>.
- [20] M. Martinez, G. Fleurier, F. Chmelík, M. Knapek, B. Viguier, E. Hug, TEM analysis of the deformation microstructure of polycrystalline cobalt plastically strained in tension, *Mater Charact* 134 (2017) 76–83. doi:<https://doi.org/10.1016/j.matchar.2017.09.038>.
- [21] R. Kapoor, B. Paul, S. Raveendra, I. Samajdar, J. Chakravartty, Aspects of dynamic recrystallization in cobalt at high temperatures, *Metall Mater Trans A* 40 (4) (2009) 818–827. doi:<https://doi.org/10.1007/s11661-009-9782-8>.
- [22] B. Paul, R. Kapoor, J. Chakravartty, A. Bidaye, I. Sharma, A. Suri, Hot working characteristics of cobalt in the temperature range 600–950 °C, *Scripta Mater* 60 (2) (2009) 104–107. doi:<https://doi.org/10.1016/j.scriptamat.2008.09.012>.
- [23] B. Paul, A. Sarkar, J. Chakravartty, A. Verma, R. Kapoor, A. Bidaye, I. Sharma, A. Suri, Dynamic recrystallization in sintered cobalt during high-temperature deformation, *Metall Mater Trans A* 41 (6) (2010) 1474–1482. doi:<https://doi.org/10.1007/s11661-010-0181-y>.
- [24] S. Suwas, R. K. Ray, Deformation textures, in: *Crystallographic Texture of Materials*, Springer, 2014, pp. 95–141.
- [25] P. Partridge, The crystallography and deformation modes of hexagonal close-packed metals, *Metall Rev* 12 (1) (1967) 169–194. doi:<https://doi.org/10.1179/mtrl.1967.12.1.169>.
- [26] M. Yoo, C. Wei, Slip modes of hexagonal-close-packed metals, *J Appl Phys* 38 (11) (1967) 4317–4322. doi:<https://doi.org/10.1063/1.1709121>.
- [27] K. Davis, E. Teghtsoonian, Plastic deformation in cobalt crystals, *T Metall Soc Aime* 227 (3) (1963) 762.
- [28] A. Seeger, H. Kronmüller, O. Boser, M. Rapp, Plastische Verformung von Kobalteinkristallen, *Phys Status Solidi B* 3 (6) (1963) 1107–1125. doi:<https://doi.org/10.1002/pssb.19630030617>.
- [29] X. Zhang, Y. Zhu, Q. Liu, Deformation twinning in polycrystalline Co during room temperature dynamic plastic deformation, *Scripta Mater* 63 (4) (2010) 387–390. doi:<https://doi.org/10.1016/j.scriptamat.2010.04.031>.
- [30] J. Jeong, M. Alfreider, R. Konetschnik, D. Kiener, S. H. Oh, In-situ tem observation of {101⁻ 2} twin-dominated deformation of Mg pillars: Twinning mechanism, size effects and rate dependency, *Acta Mater* 158 (2018) 407–421. doi:<https://doi.org/10.1016/j.actamat.2018.07.027>.
- [31] G.-D. Sim, K. Y. Xie, K. J. Hemker, J. A. El-Awady, Effect of temperature on the transition in deformation modes in Mg single crystals, *Acta Mater* 178 (2019) 241–248. doi:<https://doi.org/10.1016/j.actamat.2019.08.014>.
- [32] A. Chapuis, J. H. Driver, Temperature dependency of slip and twinning in plane strain compressed magnesium single crystals, *Acta Mater* 59 (5) (2011) 1986–1994. doi:<https://doi.org/10.1016/j.actamat.2010.11.064>.
- [33] H. Yoshinaga, R. Horiuchi, On the nonbasal slip in magnesium crystals, *T Japan I Met* 5 (1) (1964) 14–21. doi:<https://doi.org/10.2320/matertrans1960.5.14>.
- [34] J.-H. Shin, S.-H. Kim, T. Ha, K. Oh, I.-S. Choi, H. Han, Nanoindentation study for deformation twinning of magnesium single crystal, *Scripta Mater* 68 (7) (2013) 483–486. doi:<https://doi.org/10.1016/j.scriptamat.2012.11.030>.
- [35] R. Sánchez-Martín, M. Pérez-Prado, J. Segurado, J. Molina-Aldareguia, Effect of indentation size on the nucleation and propagation of tensile twinning in pure magnesium, *Acta Mater* 93 (2015) 114–128. doi:<https://doi.org/10.1016/j.actamat.2015.04.005>.
- [36] A. Bauer, S. Neumeier, F. Pyczak, M. Göken, Microstructure and creep strength of different γ/γ' -strengthened Co-base superalloy variants, *Scripta Mater* 63 (12) (2010) 1197–1200. doi:<https://doi.org/10.1016/j.scriptamat.2010.08.036>.
- [37] M. Kolb, L. P. Freund, F. Fischer, I. Povstugar, S. K. Makeneni, B. Gault, D. Raabe, J. Müller, E. Spiecker, S. Neumeier, et al., On the grain boundary strengthening effect of boron in γ/γ' cobalt-base superalloys, *Acta Mater* 145 (2018) 247–254. doi:<https://doi.org/10.1016/j.actamat.2017.12.020>.

- [38] F. Pyczak, A. Bauer, M. Göken, S. Neumeier, U. Lorenz, M. Oehring, N. Schell, A. Schreyer, A. Stark, F. Symanzik, Plastic deformation mechanisms in a crept L12 hardened Co-base superalloy, *Mat Sci Eng A* 571 (2013) 13–18. doi:https://doi.org/10.1016/j.msea.2013.02.007.
- [39] I. Weißensteiner, M. Petersmann, P. Erdely, A. Stark, T. Antretter, H. Clemens, V. Maier-Kiener, Deformation-induced phase transformation in a Co-Cr-W-Mo alloy studied by high-energy X-ray diffraction during in-situ compression tests, *Acta Mater* 164 (2019) 272–282. doi:https://doi.org/10.1016/j.actamat.2018.10.035.
- [40] W. C. Oliver, G. M. Pharr, An improved technique for determining hardness and elastic modulus using load and displacement sensing indentation experiments, *J Mater Res* 7 (6) (1992) 1564–1583. doi:https://doi.org/10.1557/JMR.1992.1564.
- [41] G. Simmons, H. Wang, Single crystal elastic constants and calculated aggregate properties, The M.I.T. Press, Cambridge, Massachusetts and London, England, 1965.
- [42] V. Maier, K. Durst, J. Mueller, B. Backes, H. W. Höppel, M. Göken, Nanoindentation strain-rate jump tests for determining the local strain-rate sensitivity in nanocrystalline Ni and ultrafine-grained Al, *J Mater Res* 26 (11) (2011) 1421–1430. doi:https://doi.org/10.1557/jmr.2011.156.
- [43] V. Maier, C. Schunk, M. Göken, K. Durst, Microstructure-dependent deformation behaviour of bcc-metals—indentation size effect and strain rate sensitivity, *Philos Mag* 95 (16-18) (2015) 1766–1779. doi:https://doi.org/10.1080/14786435.2014.982741.
- [44] J. Wheeler, D. Armstrong, W. Heinz, R. Schwaiger, High temperature nanoindentation: The state of the art and future challenges, *Curr Opin Solid St M* 19 (6) (2015) 354–366. doi:https://doi.org/10.1016/j.cossms.2015.02.002.
- [45] H. Masumoto, H. Saito, M. Kikuchi, Thermal expansion and temperature dependence of Young's modulus of single crystal of hexagonal cobalt, *Sci Rep Res Tohoku A* 19 (1967) 172–183.
- [46] M. Fine, E. Greener, Internal friction and Young's modulus of hexagonal and cubic cobalt, *T Metall Soc Aime* 212.
- [47] W. Köstner, The temperature dependence of the modulus of elasticity of pure metals, *Z Metallkd* 39 (1).
- [48] M. Göken, M. Kempf, Pop-ins in nanoindentations - the initial yield point, *Z Metallkd* 92 (9) (2001) 1061–1067.
- [49] D.-H. Lee, I.-C. Choi, G. Yang, Z. Lu, M. Kawasaki, U. Ramamurty, R. Schwaiger, J.-i. Jang, Activation energy for plastic flow in nanocrystalline CoCrFeMnNi high-entropy alloy: A high temperature nanoindentation study, *Scripta Mater* 156 (2018) 129–133. doi:https://doi.org/10.1016/j.scriptamat.2018.07.014.
- [50] P. S. Phani, W. Oliver, A critical assessment of the effect of indentation spacing on the measurement of hardness and modulus using instrumented indentation testing, *Mater Des* 164 (2019) 107563. doi:https://doi.org/10.1016/j.matdes.2018.107563.
- [51] H. McSkimin, Measurement of the elastic constants of single crystal cobalt, *J Appl Phys* 26 (4) (1955) 406–409. doi:https://doi.org/10.1063/1.1722007.
- [52] R. Hearmon, The elastic constants of anisotropic materials—II, *Adv Phys* 5 (19) (1956) 323–382.
- [53] E. Fisher, D. Dever, Temperature dependence of elastic moduli of ruthenium, rhenium, cobalt, dysprosium and erbium: A study of the elastic anisotropy-phase transformation relationship, *T Metall Soc Aime* 239 (1) (1967) 48–57.
- [54] J. J. Vlassak, W. Nix, Measuring the elastic properties of anisotropic materials by means of indentation experiments, *J Mech Phys Solids* 42 (8) (1994) 1223–1245. doi:https://doi.org/10.1016/0022-5096(94)90033-7.
- [55] D. Tromans, Elastic anisotropy of hcp metal crystals and polycrystals, *Int J Res Rev Appl Sci* 6 (4) (2011) 462–483.
- [56] G. Altmeyer, M. Jung, On hot-hardness measurements and creep-phenomena of hard-metal alloys under pressure at high temperature, *Z Metallkd* 52 (576).
- [57] F. Morral, High-purity cobalt and its properties, *JOM* 10 (10) (1958) 662–664. doi:https://doi.org/10.1007/BF03398257.
- [58] R. Fraser, D. Evans, V. Mackiw, The production and properties of ductile cobalt strip, *Can Inst Mining Met Trans* 68 (1965) 126–133.
- [59] H. Beckers, L. Fontainas, L. Habraken, B. Tougarinoff, Forming and properties of malleable cobalt (formability and malleability of vacuum melted and cast cobalt after remelting), *Journées Internationales des Applications du Cobalt* (1964) 171–186.
- [60] T. Guo, F. Siska, M. Barnett, Distinguishing between slip and twinning events during nanoindentation of magnesium alloy AZ31, *Scripta Mater* 110 (2016) 10–13. doi:https://doi.org/10.1016/j.scriptamat.2015.07.034.
- [61] R. Sarvesha, A. Gokhale, K. Kumar, N. K. Sharma, J. Jain, S. S. Singh, Effect of crystal orientation on indentation-induced deformation behavior of zinc, *Mat Sci Eng A* 776 (2020) 139064. doi:https://doi.org/10.1016/j.msea.2020.139064.
- [62] M. Martinez, E. Hug, Characterization of deformation twinning in polycrystalline cobalt: A quantitative analysis, *Mater* 7 (2019) 100420. doi:https://doi.org/10.1016/j.mtl.2019.100420.
- [63] K. Máthis, F. Chmelík, M. Janeček, B. Hadzima, Z. Trojanová, P. Lukáč, Investigating deformation processes in AM60 magnesium alloy using the acoustic emission technique, *Acta Mater* 54 (20) (2006) 5361–5366. doi:https://doi.org/10.1016/j.actamat.2006.06.033.
- [64] K. Máthis, J. Čapek, Z. Zdražilová, Z. Trojanová, Investigation of tension-compression asymmetry of magnesium by use of the acoustic emission technique, *Mat Sci Eng A* 528 (18) (2011) 5904–5907. doi:https://doi.org/10.1016/j.msea.2011.03.114.
- [65] G. Farkas, J. Pilch, P. Minárik, K. Máthis, Deformation behavior of Mg-alloy-based composites at different temperatures studied by neutron diffraction, *Acta Phys Pol A* 134 (3). doi:https://doi.org/10.12693/APhysPolA.134.881.

- [66] E. Bruder, P. Braun, H. ur Rehman, R. K. Marceau, A. S. Taylor, R. Pippan, K. Durst, Influence of solute effects on the saturation grain size and rate sensitivity in Cu-X alloys, *Scripta Mater* 144 (2018) 5–8. doi:<https://doi.org/10.1016/j.scriptamat.2017.09.031>.
- [67] V. Maier-Kiener, B. Schuh, E. P. George, H. Clemens, A. Hohenwarter, Nanoindentation testing as a powerful screening tool for assessing phase stability of nanocrystalline high-entropy alloys, *Mater Des* 115 (2017) 479–485. doi:<https://doi.org/10.1016/j.matdes.2016.11.055>.
- [68] J. W. Christian, S. Mahajan, Deformation twinning, *Prog Mater Sci* 39 (1-2) (1995) 1–157. doi:[https://doi.org/10.1016/0079-6425\(94\)00007-7](https://doi.org/10.1016/0079-6425(94)00007-7).
- [69] H. Conrad, Thermally activated deformation of metals, *JOM* 16 (7) (1964) 582–588. doi:<https://doi.org/10.1007/BF03378292>.
- [70] P. Feltham, Stress relaxation and dynamic recovery in cobalt at low temperatures, *Philos Mag* 8 (90) (1963) 989–996. doi:<https://doi.org/10.1080/14786436308214458>.
- [71] W. Püschl, Models for dislocation cross-slip in close-packed crystal structures: a critical review, *Prog Mater Sci* 47 (4) (2002) 415–461. doi:[https://doi.org/10.1016/S0079-6425\(01\)00003-2](https://doi.org/10.1016/S0079-6425(01)00003-2).
- [72] U. Messerschmidt, Dislocation dynamics during plastic deformation, Vol. 129, Springer Science & Business Media, Berlin Heidelberg, 2010.
- [73] P. Lukáč, Plastic deformation of hexagonal metals, *Czech J Phys Sect B* 31 (2) (1981) 135–141. doi:<https://doi.org/10.1007/BF01959434>.
- [74] H. Somekawa, C. A. Schuh, Effect of solid solution elements on nanoindentation hardness, rate dependence, and incipient plasticity in fine grained magnesium alloys, *Acta mater* 59 (20) (2011) 7554–7563. doi:<https://doi.org/10.1016/j.actamat.2011.08.047>.
- [75] H. Somekawa, C. A. Schuh, Nanoindentation behavior and deformed microstructures in coarse-grained magnesium alloys, *Scripta Mater* 68 (6) (2013) 416–419. doi:<https://doi.org/10.1016/j.scriptamat.2012.11.010>.
- [76] M. Yoo, S. Agnew, J. Morris, K. Ho, Non-basal slip systems in hcp metals and alloys: Source mechanisms, *Mat Sci Eng A* 319 (2001) 87–92. doi:[https://doi.org/10.1016/S0921-5093\(01\)01027-9](https://doi.org/10.1016/S0921-5093(01)01027-9).
- [77] R. Ahmad, Z. Wu, W. Curtin, Analysis of double cross-slip of pyramidal $Ic+a$ screw dislocations and implications for ductility in Mg alloys, *Acta Mater* 183 (2020) 228–241. doi:<https://doi.org/10.1016/j.actamat.2019.10.053>.
- [78] H. J. Frost, M. F. Ashby, Deformation mechanism maps: the plasticity and creep of metals and ceramics, Pergamon press, Oxford, 1982.